Actinides in the Cosmic Rays and Their Detection

by

Benjamin Alan Weaver

B.S. (University of Arizona) 1995
B.A. (University of Arizona) 1995
M.A. (University of California at Berkeley) 1998

A dissertation submitted in partial satisfaction of the
requirements for the degree of
Doctor of Philosophy

in

Physics

in the

GRADUATE DIVISION
of the
UNIVERSITY of CALIFORNIA at BERKELEY

Committee in charge:

Professor P. Buford Price, Chair
Professor Stuart J. Freedman
Professor Alexei V. Filippenko

Spring 2001

The dissertation of Benjamin Alan Weaver is approved:

Chair Date

Date

Date

University of California at Berkeley

Spring 2001

Actinides in the Cosmic Rays and Their Detection

Benjamin Alan Weaver

Abstract

Actinides in the Cosmic Rays and Their Detection

by

Benjamin Alan Weaver

Doctor of Philosophy in Physics

University of California at Berkeley

Professor P. Buford Price, Chair

I have made a measurement of the elemental abundance of cosmic rays with atomic number $70 < Z < 83$. I made this measurement as part of the Extended Analysis of the Trek detector (Extended-Trek for short). The original Trek detector consisted of 150 stacks, each of 16 sheets, of BP-1 glass exposed on the Russian space station *Mir*. In the original analysis of Trek 245 cosmic-ray events were analyzed. The cosmic-ray elemental abundance pattern observed by Trek is strongly inconsistent with the prevailing model of cosmic-ray sources. For Extended-Trek I re-analyzed 146 events in the ~ 100 stacks which were calibrated with relativistic gold ions at two zenith angles. These correspond to a collecting area of approximately 0.7 m^2. The Extended-Trek analysis improved the resolution of cosmic-ray charge to $0.35e$ over $0.39e$–$0.45e$ in the original Trek analysis and confirmed the cosmic-ray abundance pattern observed by Trek. I have developed a new computer code for the calculation of energy loss of charged particles due to ionization of matter. It is valid for highly charged nuclei and relativistic ($\gamma \approx 2$) to ultrarelativistic ($\gamma > 100$) energies. In addition to

describing the theoretical aspects of the construction of this code, I test its validity both by experiment and comparison to other codes. I have made a new determination of the empirical response function of BP-1 glass to relativistic charged particles. The data strongly suggest that this response function becomes extremely simple at low energies. In addition, I have found a very small relativistic rise in BP-1, which, though it is a clue to track formation, does not impair the performance of present or future BP-1 cosmic-ray detectors. I have made a measurement of the abundance of Ir in the Galactic cosmic rays. This is the first measurement of an odd-Z element in this region of cosmic-ray charge, other odd-Z elements in this region having natural abundances too low to make statistically significant determinations of abundance. The most abundant isotope of Ir experiences bound-state beta-decay in the Galactic cosmic rays. Finally, I give a series of recommendations for next-generation cosmic-ray detectors based on the conclusions reached in this study.

Professor P. Buford Price
Dissertation Committee Chair

Dedicated in loving memory to

Mary Lillian Harner

Mary Anne Kingsbury

Schuyler Nieukirk McClellan, Jr.

Grace Ann Weaver

they knew it all along.

Contents

List of Figures

List of Tables

Acknowledgements

Because alienation's for the rich
And I'm feeling poorer every day
— "Alienation's For the Rich," *They Might Be Giants* (1987)

- First and foremost I wish to thank Andrew Westphal and Buford Price. It was a great privilege to work with this combination of youthful energy and deep experience.

- I am grateful to Dolores Holland and the NASA GSRP program for helping pay the bills.

- I would like to thank Louis Bernhardt, Klaus Sümmerer, Margaret Hellström, Dieter Schardt, and Reimar Spohr of the Gesellschaft für Schwerionenforschung in Darmstadt, Germany for assistance during uranium beam exposures. I would also like to thank Ralf Prigl of Brookhaven National Laboratory for assistance during a gold beam exposure at the Alternating Gradient Synchrotron. Considering how much help all these people were at the wee hours of the night, it must be astonishing how much they accomplish during the day.

- Many thanks to Hans Bichsel, Jay Cummings, Pui-Tak Leung, Michael Salamon, Christoph Scheidenberger, Steven Seltzer, Allan Sørensen, and Greg Tarlé for assistance during the research into stopping-power effects.

- I am grateful to Ryan Bay, Dima Chirkin, and Ped Miocinovic for tolerating my shameless, though occasional, appropriation of their office space.

- I am deeply grateful to Michael Solarz who has probably taught me as much as ten professors. It would be impossible to enumerate all the ways he has been helpful without considerably exceeding the length of Andrew Westphal's dissertation.

- I would like to thank Christopher Snead and Lluvia Zuñiga who provided invaluable assistance to nearly every phase of Extended-Trek.

- Many thanks to (the parade): Sherley Blood, Linda Barnett, Dianna Jacobs, Anna Engberg, and LaVern Navarro, as well as Anne Takizawa, Donna Sakima, and Doris Via-Craig for making the labyrinthine Berkeley bureaucracy easier to navigate.

- I would like to thank all my friends through the years at AGSE/UAW, who not only fought the good fight, but also revealed a whole world to me outside the Physics Department. Solidarity Forever!

- Finally, I want to thank the “twin quasars of rock” John Flansburgh and John Linnell of They Might Be Giants, whose lyrics I have appropriated for all the quotations herein.

Chapter 1

Introduction

A man came up to me and said
"I'd like to change your mind
By hitting it with a rock," he said,
"Though I am not unkind."
— "Whistling in the Dark," *Flood* (1990)

Despite almost 90 years of study, the origin of Galactic cosmic rays (GCRs) remains mysterious. The GCRs may be thought of as a diffuse relativistic gas—though a gas far out of thermal equilibrium—which is present in every part of our galaxy and in most galaxies. The dominant component of GCRs consists of atomic nuclei, primarily nuclei completely stripped of electrons. Electrons and anti-protons are also present; high-energy γ-rays and neutrinos are sometimes also considered cosmic rays. This work will be concerned exclusively with the heaviest members of the ultra-heavy component of the GCRs. The ultra-heavy component of the GCRs is defined to be all cosmic-ray nuclei heavier than Zn ($Z > 30$), all the way up to the actinides ($Z \geq 90$) and possibly beyond.

Although it has been known for more than 50 years that elements heavier than hydrogen are a component of the GCRs [1, 2, 3], measurements of the ultra-heavy nuclei carried out

with balloon flights and space exposures (a nice historical summary may be found in [4]) suffered from very large systematic effects which were not recognized until the end of the 1970s. The first detectors to avoid these effects were the satellite instruments Ariel 6 and the Heavy Nuclei Experiment on HEAO-3, both launched in 1979. These were both electronic detectors whereas virtually all previous experiments had been performed with passive detectors such as nuclear emulsions and track-etch detectors. Both detectors suffered from poor charge resolution in the ultra-heavy regime and could do no better than distinguish "element groups." Furthermore, they made no strong claim to have observed any actinide cosmic rays (with $Z \geq 90$).

The leading model for the source of cosmic-ray particles was a "warm" ($\sim 10^4$ K) plasma, hot enough for most atoms to be singly ionized, but not completely ionized. The chromospheres of Sun-like stars were the best candidates for such a plasma [5, 6]. The main prediction of this model was an overabundance of elements with small values of first ionization potential (FIP) relative to solar abundances. This overabundance is actually observed in the energetic particles emitted in solar flares and the solar wind [7]. The FIP model then assumed that the cosmic-ray seed particles would be emitted from a warm plasma source and drift through the interstellar medium where they would encounter supernova shocks and be accelerated to cosmic-ray energies [8]. Figure 1.1 shows the abundance pattern expected in the FIP model based on [5]. If stellar chromospheres provide the source plasma, the average nucleosynthetic age of cosmic rays (*i.e.*, the time since nucleosynthesis) should be the characteristic age of the material out of which Sun-like stars form, a few billion years.

The abundance of "Pb-group" elements relative to "Pt-group" elements observed by HEAO [9] and Ariel [10] was sufficiently different from the FIP model prediction to lead Binns *et al.* [4] to propose a fit to the data in which the elements with $Z > 60$ were dominated by r-process [11] ma-

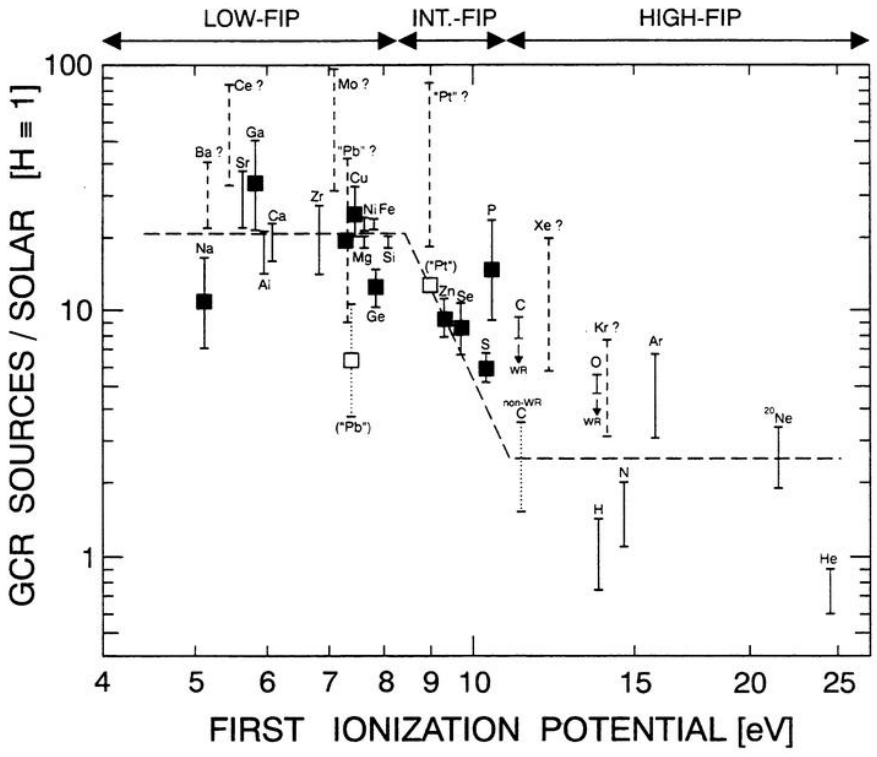

Figure 1.1: Illustration of the inverse correlation of cosmic-ray abundances with FIP. The filled black squares emphasize elements which can distinguish between a FIP model source and a volatility model source. The dotted line indicates the expectation of abundances in the FIP model.

terial. The Pt-group elements are dominated by material produced in the r-process. In fact, the Pt-group is a peak of the r-process. Pb was thought at the time to be produced predominantly in the s-process. At that time the basis for this model was purely empirical. Recently, Ramaty, Kozlovsky, and Lingenfelter [12] have proposed a model of cosmic-ray acceleration in which supernovae accelerate their own ejecta or the ejecta of nearby supernovae in OB associations. Since the r-process is thought to occur in supernovae, supernova ejecta should be naturally enhanced in r-process material. Figure 1.2 shows the models considered in [4]. Figure 1.2a indicates a source with solar-system abundances and no fractionation. Figure 1.2b is a solar source with FIP fractionation. Figure 1.2c is similar to b but with corrections to solar abundances at Ge and Pb as proposed in [13]. Figure 1.2d shows the "best source" with a ratio of s-process to r-process of 0.1 times the solar ratio for $Z > 60$ and with FIP fractionation in addition.

Alternatively, the cosmic-ray source could be nucleosynthetically "normal" (*i.e.*, with relative abundances of r-process and s-process material similar to solar abundances) but fractionated by an atomic property other than FIP. Exactly such a model was proposed originally by Epstein [14] and by Cesarsky and Bibring [15] and extensively refined recently by Meyer, Drury, and Ellison [16, 17]. In this model, interstellar dust grains are directly accelerated by supernova shocks up to about $0.01c$ and the material which becomes the cosmic rays is sputtered off these accelerated grains. As a result, the material is over-abundant in elements that easily condense into dust grains. This tendency is usually measured by the temperature at which a gas of an element condenses. Elements with a very high condensation temperature are termed "refractory" and will be the first to form grains as a gas cools. Elements with low condensation temperature are termed "volatile." For most elements, volatility (as measured by condensation temperature) is inversely correlated with FIP, so

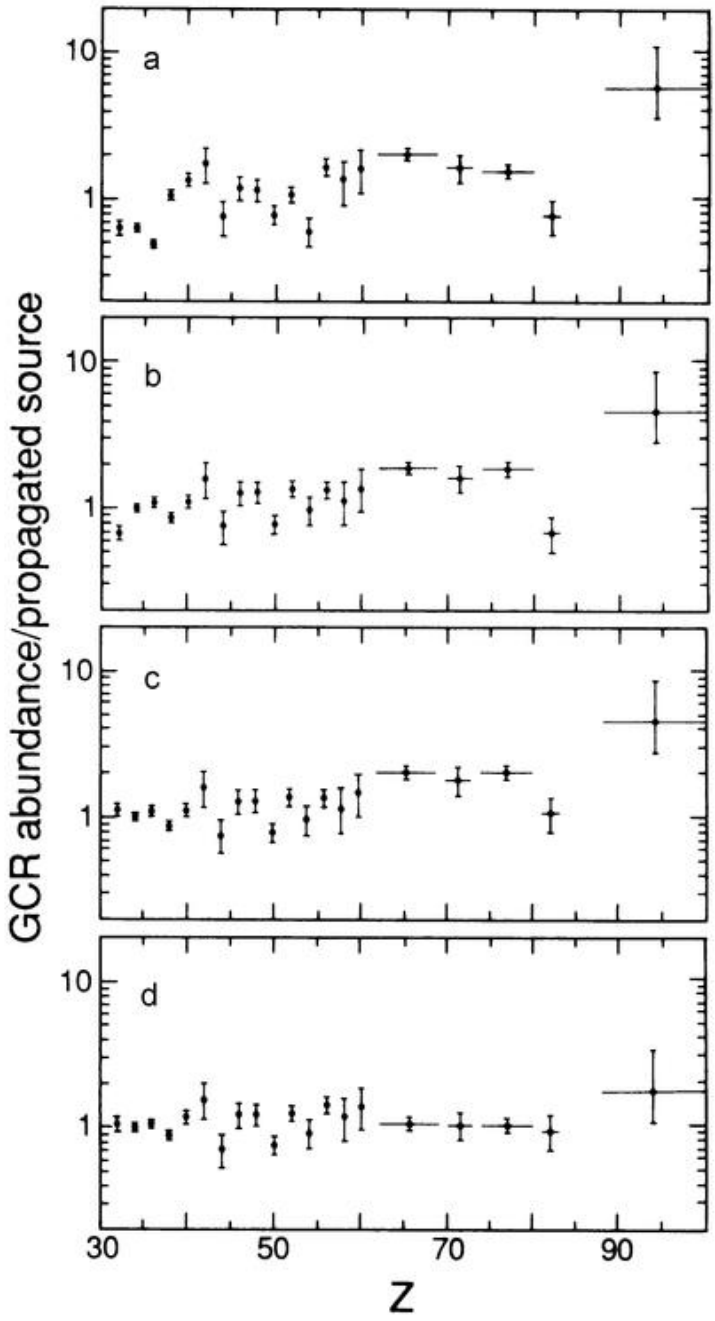

Figure 1.2: Ratios of abundance of ultra-heavy GCRs to source models. Further discussion of the propagated source models is in the main text.

that volatile elements have high FIP and refractory elements have low FIP. A few elements break this correlation; one of them is Pb which is volatile but has low FIP. The Pt-group elements Pt, Ir, and Os are all refractory. Figure 1.3 illustrates this correlation and shows the ranges of condensation temperature which constitute “refractory” and “volatile” as defined by [16].

Both the r-process model and the volatility model predict that Pt-group elements should be more abundant than Pb in the cosmic rays, while the FIP model predicts the opposite. Confirmation of the depletion of Pb relative to Pt had to wait for the Trek detector which was designed to resolve Pb cleanly from Pt for the first time. The physical characteristics of the Trek detector are described in Chapter 2. The results of the Trek analysis [18] were strongly inconsistent with the FIP model and favored both the r-process model and the volatility model. In fact, the predictions of the Pb to Pt-group abundance ratio in the r-process and the volatility models overlap, so that the two models cannot be experimentally distinguished by the more accurate measurement of the Pb abundance.

As we have seen, the competing models of cosmic-ray origin cannot be distinguished on the basis of their predictions of abundances in the range of cosmic-ray charge $70 < Z < 82$. However, the two models predict very different abundances of the actinides, $Z \geq 90$. This difference is due to the different ages of the source material. In the r-process model the source is thought to be fresh r-process material, less than 1 Myr since nucleosynthesis. The actinides, which can only be produced by the r-process, do not have time to decay significantly from their abundances at the time of nucleosynthesis (see Table 1.1 for the longest-lived actinides). In contrast, the source in the volatility model should have an age comparable to the lifetime of interstellar grains, on the order of 1 Gyr, so actinides will have had time to decay.

Trek was the first cosmic-ray detector to unambiguously detect actinides (six events) both

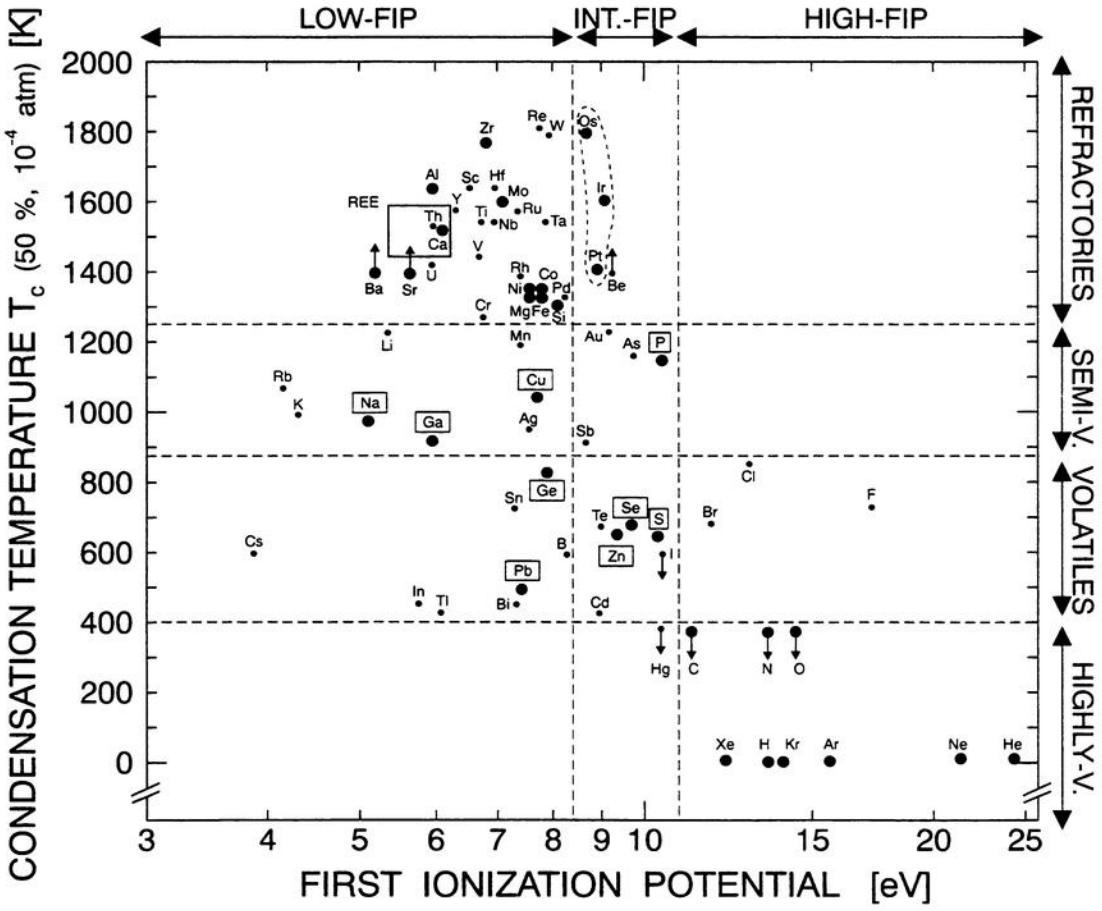

Figure 1.3: Condensation temperature plotted versus FIP, showing the inverse correlation of condensation temperature with FIP. The boxed element names are those elements which can serve as markers to distinguish FIP source models from volatility source models. The box labelled "REE" indicates rare-earth elements.

Isotope	Half-life* [yr]
^{232}Th	1.405×10^{10}
^{235}U	7.038×10^{8}
^{238}U	4.428×10^{9}
^{237}Np	2.144×10^{6}
^{244}Pu	8.00×10^{7}
^{247}Cm	1.56×10^{7}

*Source: Karlsruher Nuklidkarte, 6th ed., 1995.

Table 1.1: Longest-lived isotopes among the actinide elements.

with the correct charge, $Z \geq 90$, and cleanly separated from lower charges (*zero* events detected in the "actinide gap," $84 \leq Z \leq 89$). However, the statistical uncertainty with only six events is too large to distinguish the r-process model from the volatility model. The Extremely Heavy Cosmic Ray Composition Observer (ECCO) has been proposed as a detector capable of making a definitive measurement of the abundances of the actinides in the cosmic rays. The extreme rarity of actinides demands an extremely large area (~ 30 m^2) and a ~ 3 year exposure, to obtain adequate statistics. ECCO will consist of an array of track-etch detectors similar to Trek. An enormous advantage of track-etch detectors is that they are very inexpensive and robust compared to electronic detectors. Indeed, large-area track-etch detector arrays are probably the only way to carry out measurements such as these both inexpensively and with high probability of success. The primary goal of ECCO is the measurement of the elemental abundances of the actinides in the Galactic cosmic rays. In addition, ECCO will be capable of conducting searches for super-heavy elements, strangelets (small lumps of strange quark matter, see [19] for a recent review), and other exotic, highly ionizing particles. I give details on the planned design of ECCO in Chapter 2.

Figure 1.4 shows how the ECCO measurement of actinide abundances would depend on the age of the cosmic-ray source material. The initial abundances were computed by Pfeiffer [20]. For a young source, characteristic of the r-process model, ECCO should detect Pu and Cm. For an older source, Pu and Cm will be absent and more Th will be detected than U. A source of intermediate age, or consisting of a mixture of sources, should also be distinguishable based on the relative abundances among the various actinides. If it should prove the case that the cosmic-ray source consists primarily of young material (the unambiguous detection of ^{247}Cm would guarantee this), then the abundances of Th and U will be little changed from their abundances at the time of

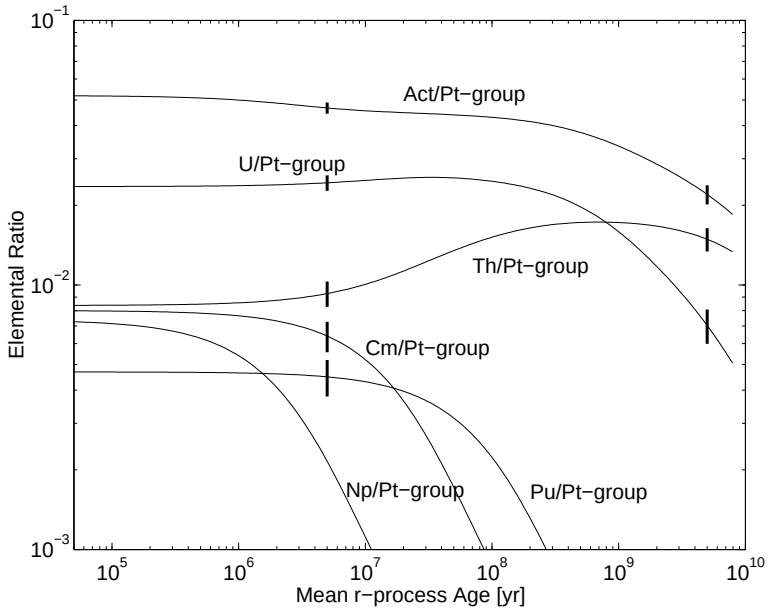

Figure 1.4: Relative abundances with respect to the Pt-group ($75 \leq Z \leq 79$) of the actinides as a function of time since nucleosynthesis. The top curve is the sum of all actinides. The thick vertical bars indicate the anticipated statistical error bars for the ECCO detector.

nucleosynthesis. The yields of U and Th at the time of nucleosynthesis are unknown, but of critical importance in radioactive dating methods to determine the age of the Galaxy.

We have been presented with an opportunity to "field-test" the analysis techniques which will be applied to ECCO. I describe this test and the results in Chapter 2. In Chapter 3, I develop the theory describing the energy loss of charged particles in matter and the code necessary to handle very large charges at relativistic energies. In Chapter 4, I lay the groundwork for the measurement of the response of track-etch detectors to relativistic actinides. In Chapter 5, I demonstrate the versatility of track-etch detectors by conducting a search for a rare form of beta-decay which has not been observed in the laboratory for an isotope of Ir, despite the fact that the isotope is both common and stable in Nature. I conclude with a series of recommendations for the design of ECCO.

Chapter 2

Trek and Extended-Trek

Checking out and flying
By rocket to the Moon
By airplane to the rocket
By taxi to the airport
By front door to the taxi
By throwing back the blanket, hanging down the legs
— "Destination Moon," *John Henry* (1994)

2.1 Introduction

The Trek ultra-heavy cosmic-ray collector (Trek for short) was installed on the exterior of the *Mir* space station in 1991. The detector was composed of 150 stacks of sheets of BP-1 glass, a barium phosphate track-etch detector developed at the University of California at Berkeley [21]. The total surface area was about 1 m^2, and the effective aperture was about 1 sr. Each stack contained 16 sheets of 9 cm $\times$ 9 cm $\times$ 1.5 mm BP-1 glass. One third of Trek was returned to Earth in November 1993 in a dedicated re-entry capsule. The remainder was returned in November 1995 by Space Shuttle *Atlantis* (STS-74).

After recovery, to correct for small variations in chemical composition, all stacks were calibrated with 10.8 A GeV Au ions (the heaviest ion available) at the Alternating Gradient Synchrotron (AGS) at Brookhaven National Laboratory. Hereinafter I use the notation "A GeV" for "GeV per nucleon," and similarly for "A MeV" and "A TeV." The first batch of glass returned was exposed to this beam at normal incidence, *i.e.*, with the beam directed exactly perpendicular to the stack of detectors. The remaining stacks were exposed to this beam at both 15° and 40° zenith angle (measured with respect to the normal).

2.2 The Trek Analysis

For Trek measurements in the platinum-lead region, we removed six sheets from each stack (numbers 1, 2, 7, 8, 13, and 14), allowing up to twelve measurements on a cosmic-ray track. The remaining sheets were reserved for later analysis. We annealed these sheets for five days at 50°C to remove the effects of differential track fading during exposure in orbit. After annealing, we etched the glass plates in 49% HF at room temperature for 72 hours. Forty sheets of glass were etched simultaneously in four gallons of etchant, which was stirred vigorously to insure uniform etching conditions throughout the volume of the tank. The limitation on the number of sheets meant that the Trek analysis required more than twenty separate etches. Approximately 50 μm of material was removed from each surface. The glass was then scanned, both manually and automatically, to locate cosmic-ray tracks. The etch-pits of both cosmic rays and neighboring calibration tracks were then measured, along with cosmic-ray trajectories, and the amount of material removed by etching. From these measurements, the charge and energy of each cosmic ray were determined.

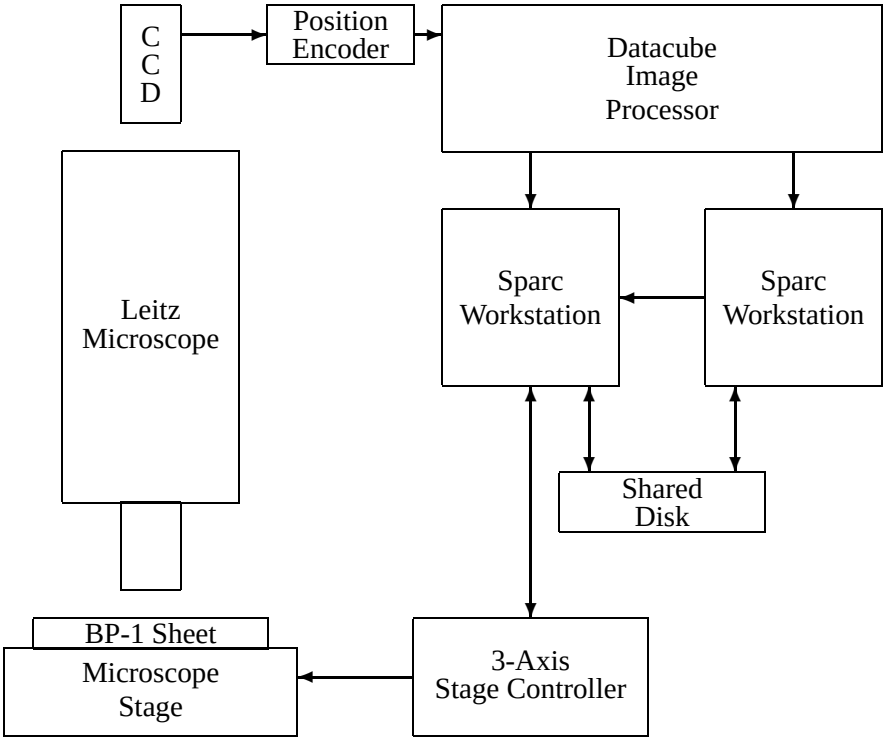

Figure 2.1: Schematic layout of the automated scanning system used for the Trek analysis.

2.2.1 Automated Digital Scanning Microscopy

Over the last several years we have developed an automated scanning system for the analysis of cosmic-ray, nuclear, and atomic interaction experiments. The scanning system consists of a Leitz microscope, a three-axis computer-controlled stage, a CCD camera, a Datacube image processor, and a Sun computer. The stage may also be controlled through a joystick. The layout of the scanning system is illustrated schematically in Figure 2.1.

The unprocessed image of an etch-pit in the microscope is a black ellipse against a bright background. The raw image from the CCD camera is directed to the image processor, which digitizes the image, producing an array of brightness values $I_{i,j}$. The image processor then computes, in

real time, a "gradient" array

$$v_{i,j} = \left| \sum_{k=j-1}^{j+1} I_{i+1,k} - I_{i-1,k} \right| + \left| \sum_{k=i-1}^{i+1} I_{k,j+1} - I_{k,j-1} \right|, \tag{2.1}$$

where i and j are the pixel coordinates. This operation produces an image $v_{i,j}$ in which edges are bright, and flat-fields are dark. In this image, the etch-pits appear to be nearly uniform elliptical rings, with widths of order several pixels. The image processor then selects pixels from $v_{i,j}$ that exceed a preset threshold value and passes a list of the coordinates and brightnesses of these pixels to the Sun computer.

This list of pixels is then organized by the computer into contiguous groups, using a rapid clustering technique developed by Daniel Snowden-Ifft (unpublished). A thinning algorithm developed by Winthrop Williams (unpublished) reduces the widths of the elliptical rings from several pixels to ~ 1 pixel, which is useful in subsequent determination of the goodness-of-fit. These clusters of pixels are then fitted to ellipses, using an analytic, fast-fitting algorithm [22], giving the semi-major and semi-minor axes of the ellipse, a and b, the coordinates of the geometric center of the ellipse, h and k, the orientation of the ellipse, ϕ, and the χ^2 of the ellipse fit. The focus height can also be determined. The physical magnitudes of size and position, in microns, are then computed, and the measurements are values recorded in a computer file. The dispersions in repeated measurements of a single event, while moving the event randomly within a field of view, are 0.026 μm for (a,b), and < 1 μm in position (x,y), when scanning using a $25\times$ objective.

For automated scanning, the computer moves the stage, making a raster-scan of each detector. The coordinate system for a scan is defined by two fiducial events at either corner of a rectangular scanning region. In the typical case, the glass sheet to be scanned has been exposed, usually in a stack with other glass sheets, at an accelerator. It is convenient to choose the etch-

pits from two of these beam particles as fiducials, so that the resulting coordinate system will be consistent among all sheets of glass within a stack. Before scanning, a map of the height of the glass surface is made on a rectangular grid, using manual focusing. The focusing accuracy is $< 2\ \mu$m. The focus height is determined at any arbitrary point by interpolation. These focus maps are archived on computer disk. During a scan, the positions and ellipse characteristics of all etch-pits within each field of view are recorded in a computer file for subsequent analysis.

For the Trek analysis, we have developed a novel scanning technique which has given an improvement in scanning speed of a factor of ~ 6 over previous methods. There are three novel aspects of the new system. First, the stage is illuminated by a stroboscopic illumination system—this allows the stage to move continuously, without the need to stop the stage for each image. Second, the position of the stage is encoded digitally in the video image itself, so that the position of the stage is measured at precisely the time of the strobe flash (with $\sim 1\ \mu$m accuracy). Finally, the scanning computer writes the raw pixel data onto a shared disk, and another, faster, computer does the ellipse-fitting of etch-pit mouths. Figure 2.2 shows two Trek calibration etch-pits. Figure 2.3 shows the "gradient" of Figure 2.2 as computed by (2.1). Figure 4 of [23] has a full-color illustration of this procedure.

The scanning system was employed to automatically search for cosmic-ray events. The top surfaces of two adjacent sheets of glass (usually sheets 7 and 8) were scanned, and a matching algorithm was used to identify candidates. The system automatically returned to each candidate event, and recorded the images of the etch-pits on disk. After the automated procedure was completed, we reviewed the images and identified actual cosmic-ray tracks, confirming the identification in a stereo microscope. The automated scanning rate for the Trek glass was $\sim 250\ \mathrm{cm}^2\ \mathrm{day}^{-1}$. We

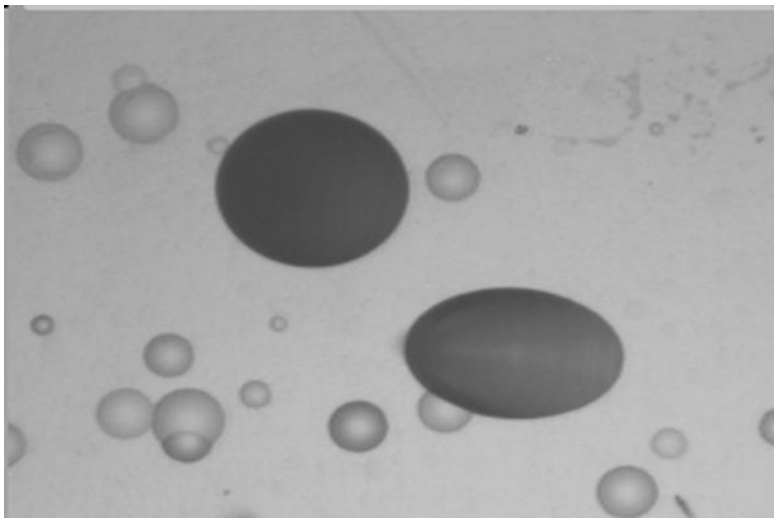

Figure 2.2: Image of typical Trek calibration etch-pits at two zenith angles.

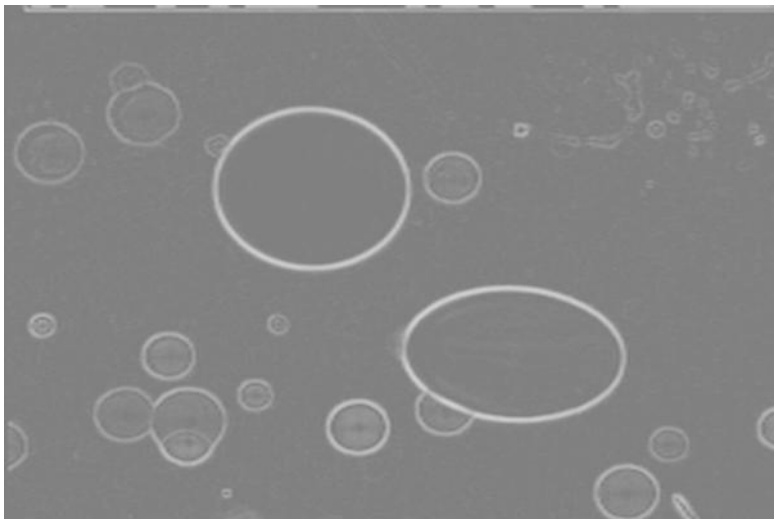

Figure 2.3: Gradient image of typical Trek calibration etch-pits at two zenith angles.

also scanned aligned adjacent sheets manually using a stereo microscope. The efficiency, in a single scan, for finding a cosmic ray with semi-minor axis greater than 10 μm was $\sim$ 90%, and was independent of etch-pit size.

The microscope stage accommodated four 9 cm $\times$ 9 cm sheets of glass at one time. Thus, it was convenient to scan several regions sequentially in a procedure which lasted many hours. Occasionally the scanning system crashed due to lock-up of the stage drivers, a computer failure, or overheating of the system due to air-conditioning failure. We monitored the health of the scanning system continuously using an independent monitoring computer and a paging service which could be activated automatically by electronic mail to alert us to the failure.

2.2.2 The Trek Charge Measurement

The empirical response function used in the Trek analysis is discussed extensively in Chapter 4. The function published in [23] was a rather poor fit to the low-energy data, resulting from the observation, at high energies, that the response function was separable into independent functions of Z and β. This empirical function, along with a standard range-energy code [24], was used to determine the charge and energy of cosmic rays, in the original Trek analysis. To make the measurement of charge, etch-pit sizes and positions were measured on up to 12 surfaces in each stack of glass. First, the semi-minor axis of the elliptical etch-pit mouth is measured, the trajectory is then determined, and the thickness of material removed from each glass surface, G, is measured. The signal, s, defined to be the ratio of track-etch rate to general etch rate, is then determined from the geometry of the etch-pit (see Appendix B).

Empirically, changes in response due to small variations in composition, track-fading, or changes in detector temperature are characterized by constant additive shifts in response, nearly

independently of the value of the response. Furthermore, the intrinsic dispersion of the detector may be characterized by a nearly constant dispersion in signal, which is also independent of the value of the signal (however, see §2.4.2). To correct the cosmic-ray signal, we first identified populations of 10.8 A GeV Au calibration etch-pits in the scan data. For each population we performed a Gaussian fit to the histogram of semi-minor axis measurements of the most populous (Au) charge peak and used the mean value from this fit, $b_{\rm cal}$, as the representative value of b for the purposes of calculating response. The histogram of $b_{\rm cal}$ consistently had width $\sigma \approx 0.2$ μm, one order of magnitude larger than the dispersion in measurement. This width is due to the intrinsic dispersion of the BP-1 track-etch detector. The calibration data were incorporated into the measurement in a very simple way. We defined the standard response to 10.8 A GeV Au to be $\xi_0 = -0.27$. For the original Trek analysis ξ was the variable characterizing detector response, $\xi = \ln(s-1)$ (however, see Chapter 4). We then calculated a correction by computing a difference between the calibration response and the standard response. The corrected cosmic-ray response $\xi'_{\rm e}$ was thus

$$\xi'_{\rm e} = \xi_{\rm e} - (\xi_{\rm cal} - \xi_0)\,. \tag{2.2}$$

For a range of charges and energy, the response was calculated for a nucleus following the same trajectory as the cosmic ray, using a range-energy code and the measured response function. This was compared to data and the best values of Z and E were determined by maximum likelihood.

2.2.3 Trek Error Analysis

Trek Monte Carlo Simulation

It is tedious and sometimes impossible to analytically propagate every measurement error to a dispersion in charge. Therefore, we created a Monte Carlo simulation of an idealized Trek

experiment to calculate dispersion in charge measurement due to various effects. Using the set of the measured charge, energy, and zenith angles from our cosmic-ray data set, we formed simulated data, adding sources of dispersion from our list (Table 2.1), one at a time or in combination. We then measured the charges of these simulated events by the same method used for analyzing Trek data, and measured the width and shift of differences between measured charge and input charge, thus determining the charge dispersion and shift. To stay as close to the experiment as possible, we also simulated events which did not appear on all 12 surfaces by removing the same surfaces from consideration in the analysis in the Monte Carlo simulation. We have also simulated dispersive effects on the 40° zenith angle gold calibration beam and calculated the resulting charge shifts (ΔZ_{40}). This dispersion value in the Monte Carlo simulation comes from the "trimmed" dispersion, which is the square root of the variance of the data with the outlying 1% of events removed. The results of the Monte Carlo simulation often have broad non-Gaussian tails which inflate the estimate of the variance. We then divided the "trimmed" dispersion by 0.93 to correct to a Gaussian dispersion.

The first two sections of Table 2.1 contain the dispersion due to response and zenith angle fluctuations. In each case the measured value gives the real dispersion in charge measurement. Above each measured value are effects which contribute to this type of dispersion. For example, errors in the value of G, the amount of material removed during etching, add some width to the total dispersion in response. Thus each contributing effect adds in quadrature to give the measured value. Table 2.2 contains effects which would tend to shift the measured charge away from its true value. Here the charge shifts are ΔZ_{40}, the shift in charge of a 10.8 A GeV Au calibration beam at 40° zenith angle.

The report on the performance of the Trek detector [23] contains extensive discussions

Source of Dispersion	Magnitude	Contribution to Charge Dispersion (e)
Response fluctuations		
G random error (0.4 μm)	$\sigma_\xi(G) = 0.011$	0.241
b random error (0.025 μm)	$\sigma_\xi(b) = 0.002$	0.039
inferred intrinsic dispersion	$\sigma_\xi = 0.018$	$0.240^\star$
measured, adjacent surfaces	$\sigma_\xi = 0.021$	0.342
Zenith angle errors		
index of refraction (0.2%)	0.073°	0.028
x,y random error (0.7 μm)	0.037°	0.014
z random error (1.7 μm)	0.064°	$0.024^\star$
multiple Coulomb scattering	0.091°	0.034
non-parallel sheet surfaces	0.025°	0.009
measured value	0.14°	0.054
Calibration errors		
statistics	≈ 0.014 μm	0.029
focus	< 3 μm	< 0.068
illumination	< 0.04 μm	< 0.01
anellipticity	0.3%	0.022
Other contributions		
thickness random error	2 μm	0.016
unmeasured sheet thicknesses	41 μm/sheet	0.012
straggling	—	0.001
electron capture and stripping	—	$0.15^\dagger$
nuclear fragmentation	—	$0.15^\dagger$
isotopic spread	0.58 amu	0.006
registration temperature variation	$< 10^\circ$C	< 0.06
track fading after corrective anneal	4 yr at 25°C	0.09
Range of charge resolution		$0.36 - 0.42$

*Estimated or inferred

†With no rejection

Table 2.1: Contributions to dispersion in the measurement of charge in the original Trek Analysis. All magnitudes were measured unless otherwise indicated. Indented values are contributions to the measured values.

Source of Dispersion	Magnitude	Contribution to Charge Shift (e)
b anisotropy	0.1%	0.009
position anisotropy	$< 0.024\%$	< 0.011
G offset	$< 0.5\ \mu$m*	< 0.055
position offset	$< 2\ \mu$m	< 0.009
b offset	$< 0.2\ \mu$m*	< 0.035
thickness offset	$< 5\ \mu$m	< 0.010
b scale factor	$< 0.6\%$	< 0.032
position scale factor	$< 0.6\%$	< 0.022
thickness scale factor	$< 0.5\%$	< 0.015
anellipticity	0.3%	0.057
focus	$< 3\ \mu$m	< 0.031
measured value (3σ limit)	—	$\lvert\Delta Z_{40}\rvert < 0.04e$

*Estimated or inferred.

Table 2.2: Systematic errors contributing to charge shifts in the Trek Ultraheavy Collector.

of each of these sources of dispersion. By far the largest sources of dispersion are the error in measurement of G and the intrinsic dispersion of the detector. These deserve detailed discussion.

Dispersion in G

Accurate determination of the amount of material etched from each glass surface, G, is of crucial importance in determining the signal due to a cosmic ray. We determined G by three methods, two of which are nearly independent of each other, and a third which is completely independent of the first two.

First, we measured the thickness of each sheet of glass in four corners using a digital micrometer which was nominally accurate to 1 μm. We measured the thickness before (T_b) and after (T_a) the etch. G is thus trivially

$$G_\mathrm{thick} = \frac{1}{2}\left(T_\mathrm{b} - T_\mathrm{a}\right). \tag{2.3}$$

Second, we measured the weight loss Δw due to etching. With the idealization that each sheet of glass is a rectangular solid, and ignoring third-order terms in G/T, we determined $G_{\rm weight}$ by solving

$$a_1 G_{\rm weight}^2 + a_2 G_{\rm weight} + a_3 = 0, \tag{2.4}$$

where $a_1 = T_{\rm b}\rho/w_{\rm b} + 2\sqrt{\rho/(T_{\rm b}w_{\rm b})}$, $a_2 = -1/T_{\rm b} - \sqrt{T_{\rm b}\rho/w_{\rm b}}$, $a_3 = \Delta w/w_{\rm b}$, $w_{\rm b}$ is the weight before etching, and ρ is the density of the glass. The sheets were not in fact rectangular solids, but departures from this geometry introduced errors of order $\ll 1\ \mu$m. The weight and thickness methods share only one measurement, $T_{\rm b}$, errors in which have a negligible effect on $G_{\rm weight}$.

The third method, possible only for about two-thirds of the Trek instrument, used the measured average values of b for the low-angle ($\sim 15^\circ$) and high-angle ($\sim 40^\circ$) calibration beams. Since BP-1 glass is an isotropic material, the value of the response must be identical for both beams. Thus a third value, $G_{\rm calib}$, may be computed by equating the geometric formula for response for the two calibration beams:

$$a_1' G_{\rm calib}^4 + a_2' G_{\rm calib}^2 + a_3' = 0, \tag{2.5}$$

where $a_1' = 1 - \cos\theta_1/\cos\theta_2$, $a_2' = (1 + \cos\theta_1/\cos\theta_2)(b_1^2 - b_2^2)$, and $a_3' = (\cos\theta_1/\cos\theta_2 - 1)b_1^2 b_2^2$; θ_1 and θ_2 are values of the zenith angle for the low-angle and high-angle calibration beams, measured individually in each stack of glass. $G_{\rm calib}$ is completely independent of $G_{\rm weight}$ and $G_{\rm thick}$.

We found that the values obtained by each of the three methods agreed remarkably well. In Figures 2.4 and 2.5 we show the distributions of the differences in measurement of G in the three methods. The difference between $G_{\rm weight}$ and $G_{\rm calib}$ shows the smallest dispersion. Thickness measurement appears to have a larger intrinsic dispersion than the other two methods.

The value of G can vary from etch to etch, due to small differences in temperature or

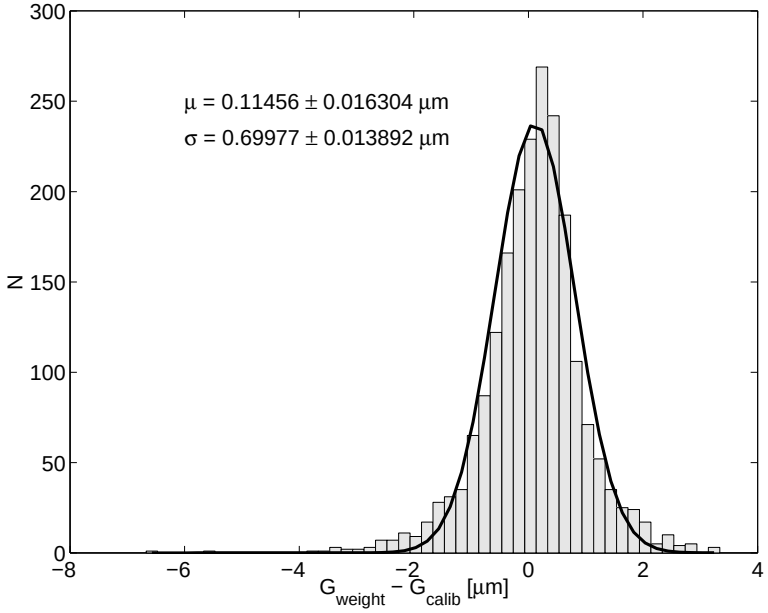

Figure 2.4: Histogram of differences between G_{weight} and G_{calib}.

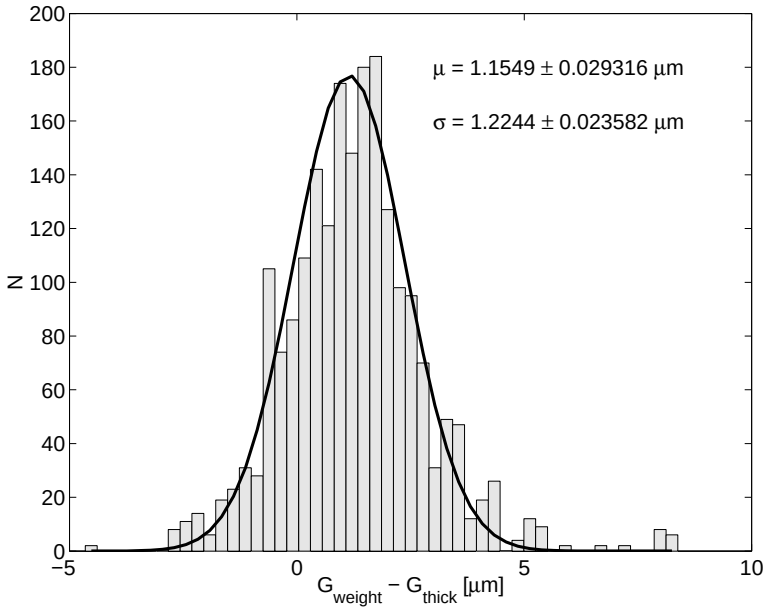

Figure 2.5: Histogram of differences between G_{weight} and G_{thick}.

differences in the composition of the etchant. If the variation in G were due solely to variations in etching conditions, then one would expect to observe no correlation between measurements by weight and by calibration for glass sheets etched simultaneously in the same etch tank, since these measurements are completely independent of each other. We tested this hypothesis by subtracting $\langle G \rangle$, the average value of G for that etching batch, from each measured value of G. We found that the values of $G_{\text{weight}} - \langle G_{\text{weight}} \rangle$ and $G_{\text{calib}} - \langle G_{\text{calib}} \rangle$ were correlated (Figure 2.6). We attribute this correlation to an actual variation in G from sheet to sheet within each etch. The dispersion of these physical fluctuations is denoted $\sigma(G_{\text{actual}})$ below. This variation may be due to small differences in glass composition between sheets, or to small variations in etching conditions from one location to another within the etch tank, although all etches were vigorously stirred. From the widths of the distributions of $G_{\text{weight}} - \langle G_{\text{weight}} \rangle$, $G_{\text{calib}} - \langle G_{\text{calib}} \rangle$, and $G_{\text{weight}} - \langle G_{\text{weight}} \rangle - (G_{\text{calib}} - \langle G_{\text{calib}} \rangle)$, we were able to estimate the dispersions in measurement of G by weight and by calibration, and the actual value of G:

$$\begin{aligned} \sigma(G_{\text{weight}}) &= 0.40 \pm 0.13\ \mu\text{m} \\ \sigma(G_{\text{calib}}) &= 0.26 \pm 0.21\ \mu\text{m} \\ \sigma(G_{\text{actual}}) &= 0.70 \pm 0.04\ \mu\text{m}. \end{aligned}$$

Intrinsic Dispersion

The intrinsic fluctuation in response, apparently due to microscopic variations in track-etch rate [25], is the largest source of dispersion in charge measurement. The intrinsic dispersion was determined by measuring the difference in cosmic-ray response on two adjacent surfaces. Since the measurement segments were adjacent, and were much shorter than the mean free path for

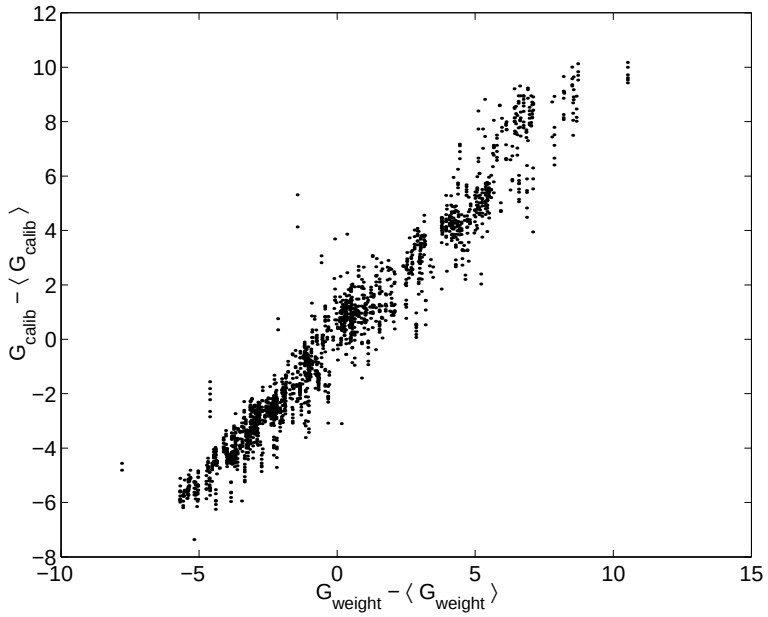

Figure 2.6: Scatterplot of values of $G_{\text{weight}} - \langle G_{\text{weight}} \rangle$ against $G_{\text{calib}} - \langle G_{\text{calib}} \rangle$.

change of ionic charge state, the ionic charge and velocity were identical for both measurements (Figure 2.7). The dispersion for one surface is then $\sigma_\xi(\text{total}) = \sigma_{\Delta\xi}/\sqrt{2}$. In addition, the response is a function of b, G, and θ, so errors in each of these quantities introduce errors in the response. We can find the true intrinsic dispersion by subtracting other sources of dispersion:

$$\sigma_\xi^2(\text{intrinsic}) = \sigma_\xi^2(\text{total}) - \sigma_\xi^2(G) - \sigma_\xi^2(b) - \sigma_\xi^2(\theta). \tag{2.6}$$

After subtraction we find $\sigma_\xi(\text{intrinsic}) = 0.018$, which is consistent with the observed widths of charge peaks in the calibration scans.

The primary lesson learned from the detailed analysis of the various sources of error in the Trek detector was that, with the exception of intrinsic dispersion, many of the sources of dispersion can be controlled or eliminated with new and creative techniques. These techniques could be applied not only to a next generation cosmic-ray detector, but to a reanalysis of the Trek detector itself.

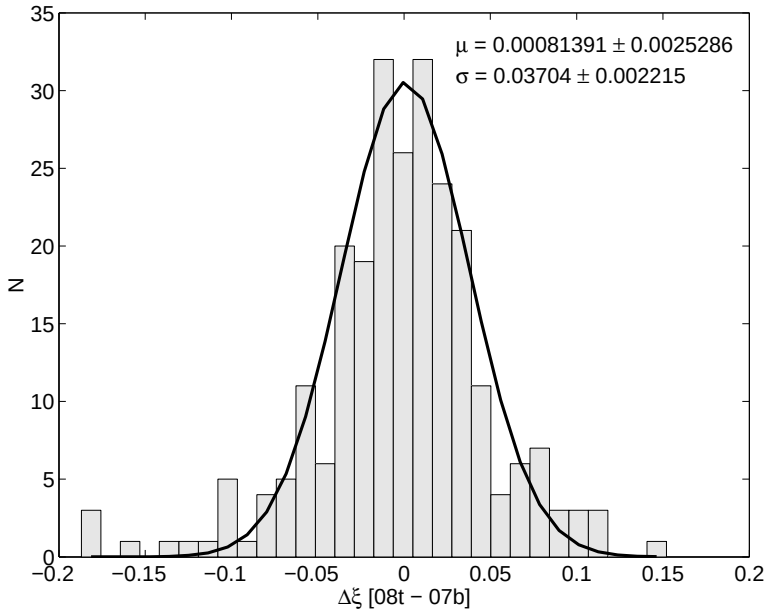

Figure 2.7: Illustration of response on adjacent surfaces.

2.3 Design of ECCO

Before we consider new analysis and detector handling techniques developed recently, it would be helpful to have some context to understand the motivation for these new techniques. As mentioned in Chapter 1, ECCO has been proposed as the successor to Trek, optimized in design and area to detect the rare actinides. In current proposals, ECCO would have an area of ~ 30 m^2 and an exposure time of about three years. With such a large area, stacks of BP-1 sheets become very expensive, since the cost of manufacturing a sheet of BP-1 glass is dominated by the cost of cutting the glass into sheets and final grinding and polishing. In addition, most of the area of polished glass would never be examined. Instead, ECCO is being designed around a radical new approach to track-etch detector configuration—the "monolithic block" detector.

At minimum, ECCO monolithic blocks would measure 25 cm $\times$ 25 cm $\times$ 2.5 cm. Each

monolithic block would be sandwiched between thin sheets of BP-1. The most likely configuration would be two layers of thin ($\sim$ 1 mm) sheets on both faces of the block, tiled to cover the full area. The outermost layers on the top and bottom would serve as a hodoscope (a detector which provides a position measurement without identifying the event). After exposure this layer would be removed first and etched for a long time in a very sensitive etchant (probably HBF_4) until cosmic-ray tracks were etched all the way through the sheet, forming tiny holes. The positions of the holes can be rapidly located using the gas-transfer technique: the etched sheet is placed adjacent to an ammonia-sensitive paper or plastic and the other side is exposed to ammonia vapor. Where the ammonia penetrates an etched-through hole a spot forms on the plastic. The locations of these spots can be identified by automated scanning techniques inherited from our development of automated microscope scanning. The best results so far have been obtained with azolite plastic.

After the positions of potentially interesting tracks are located, the second layer of glass sheets is removed. These sheets are etched in an etchant suitable for preliminary charge identification: NaOH for actinides, HF for Pb and Pt-group elements. The signal of these charges would be saturated in HBF_4 (see Appendix B).

Once the interesting cosmic rays are located, the monolithic block is placed on a computer-controlled milling machine. Using a diamond-tipped, water-cooled core drill, a core surrounding the cosmic ray is removed. The result is a BP-1 cylinder with the cosmic-ray track along the axis of the cylinder. Figure 2.8 shows a BP-1 monolith being cored. This cylinder is then exposed to calibration beams. The cylinder is subsequently diced into wafers with a precision dicing machine of the sort used in semiconductor manufacture. Figure 2.9 shows samples of BP-1 cores in various stages of the dicing process. The wafers will probably have an initial thickness of roughly 1000 μm

after grinding and polishing. The wafers are then etched and analyzed. After a round of analysis, the wafers can be resurfaced for maximal sampling (see §2.5).

Based on this design we can imagine several laboratory tests which can be performed to verify the performance of ECCO before it is even constructed. Using materials readily available from the Trek detector, some of the tests which can be performed in preparation for ECCO are as follows:

- Coring BP-1 glass.
- Handling of wafers, especially in etching.
- Automation of data analysis beyond that used in Trek.
- Improvements in charge resolution resulting from more measurements on individual cosmic rays.
- Effects of resurfacing on actual cosmic rays.

In the following sections I will discuss all of these tests.

2.4 Extended-Trek

2.4.1 New Techniques

After the first Trek analysis was completed, the remaining Trek glass was placed in cold storage. Since 16 sheets were available, up to 32 measurements of a single cosmic-ray track were possible. Crudely, one might expect an improvement of $\sim \sqrt{3}$ in the charge resolution if all these measurements were made. In addition, as demonstrated in [23], the uncertainty in the value of G

Figure 2.8: A BP-1 monolith being cored.

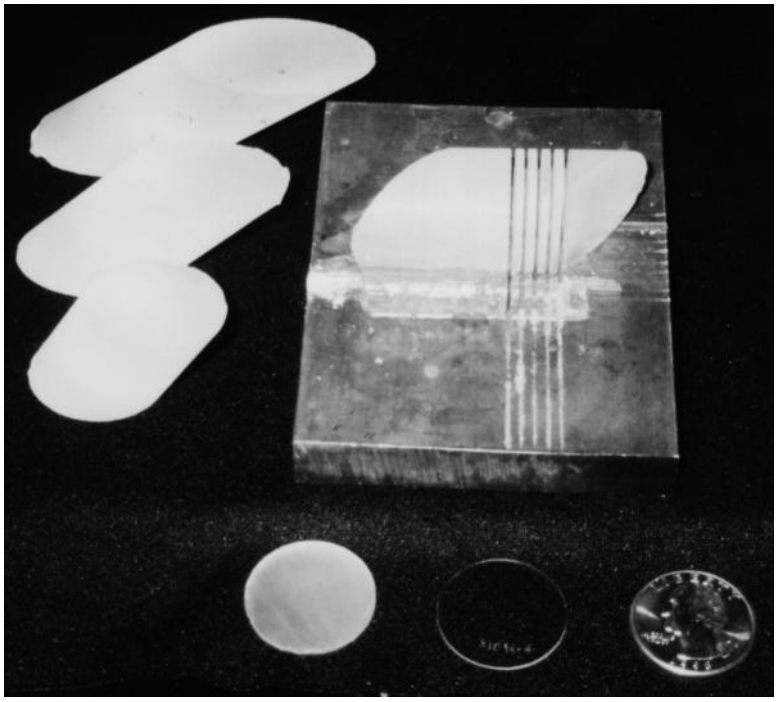

Figure 2.9: Samples of BP-1 cores at several angles along with a diced core, an unpolished wafer, and a polished wafer.

measured by weight loss is a significant contribution to overall measurement dispersion. For the Extended Analysis of the Trek Detector (Extended-Trek for short), we have selected cosmic-ray tracks from the group of Trek stacks which were calibrated at two zenith angles. The two zenith angles allow a more precise measurement of *G*, the amount of material removed by etching, in addition to other consistency checks described in [23]. We have etched the remaining ten sheets from each selected Trek stack and combined the measurements with the original Trek data set to obtain up to 32 measurements of each individual cosmic ray.

A novel feature of Extended-Trek is the coring technique. Instead of etching an entire sheet of glass we use a water-cooled diamond-tipped core drill to remove a 2.5 cm diameter wafer which is nominally centered on the cosmic-ray track location. Thus the amount of glass which actually needs to be etched is dramatically reduced. While the original Trek analysis required more than 20 etches, the Extended-Trek etching was completed with *only two* primary etches with no change in the etch tank. The cost of etchant is always significant, and, especially in the case of HF, disposal costs can more than double the final cost of a quantity of etchant.

The uniform size of Extended-Trek wafers allows us to maximize the amount of scanning which can be performed on our existing microscope stage. In the original Trek analysis, the size of the sheets limited the number of automated scans which could be performed in one session. With Extended-Trek we are limited by the physical range of motion of the stage, and can perform 49 automated calibration scans after a single setup.

We have already made a number of advances in data analysis which will have a direct impact on the future analysis of ECCO. The first advance is in the automated measurement of cosmic-ray signal. Each cosmic-ray etch-pit is electronically photographed and the image is passed

through an image processor which produces a threshold gradient image. The pixels which make up the rim of the etch-pit are selected and their coordinates are written to a file. Occasionally, the cosmic-ray etch-pit will intersect small over-etched pits due to low-charge, low-energy cosmic rays. These can break up what would otherwise be an essentially perfect ellipse. In the past we have removed the pixels due to these defects by manually editing the file containing the pixel coordinates. However, we have found a technique for automatically editing these files, provided the defects are not too large. We start by fitting an ellipse to the unedited coordinates. We then identify the pixels which fall outside the fitted ellipse and which are farthest from the fitted ellipse. These pixels are removed from the analysis, and the fit is repeated on the remaining pixels. This process is repeated until all remaining pixels lie 1 μm or less from the fitted ellipse. This technique has reduced the amount of manual editing required by roughly an order of magnitude. Figure 2.10 shows a typical cosmic-ray etch-pit with a small bowl-shaped pit on the left side. The pixels identified by the image processor are shown in Figure 2.11 on the left-hand side. Note that the bowl was picked up in the pixel identification along with the cosmic ray. The bowl feature was automatically removed during editing and the fit is shown on the right side of Figure 2.11. The slight change in the azimuth angle of the ellipse is an artifact of the pixel-editing algorithm, which rotates the pixels into a frame in which the ellipse azimuth angle of the original ellipse fit is zero.

Another advance has been made in the automated identification of orbital electron attachment. The short sampling distance and excellent charge resolution of BP-1 allow us to observe cases where a cosmic-ray nucleus has temporarily captured a single orbital electron. To automatically identify such events, we first perform a maximum-likelihood fit to the signal-versus-distance data with the assumption that the cosmic-ray charge remains constant throughout. Then for each

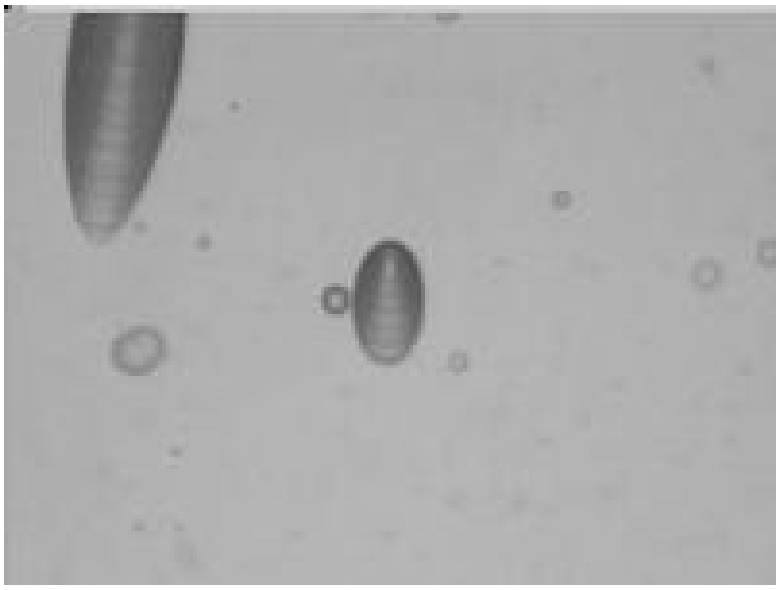

Figure 2.10: Cosmic-ray etch-pit under 25× magnification.

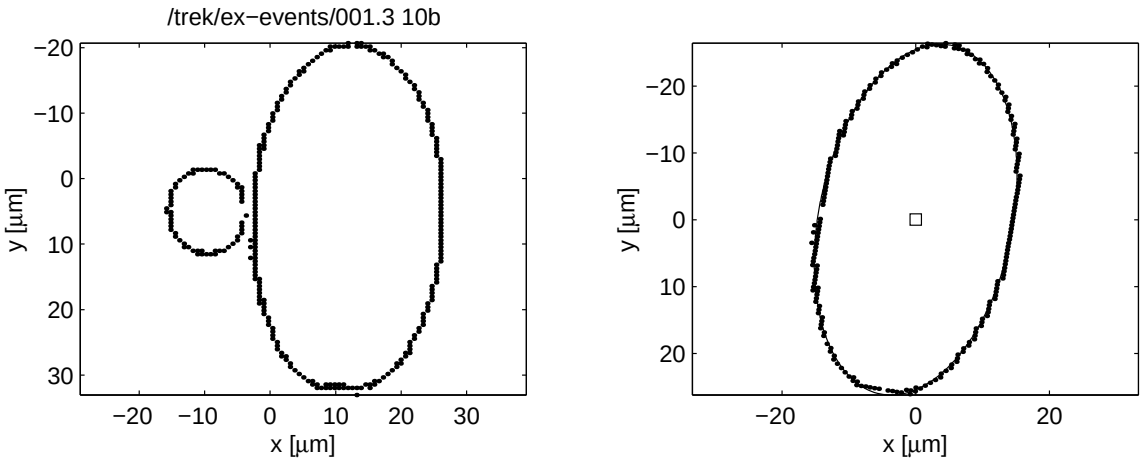

Figure 2.11: Left: pixels identified by the image processor for further analysis. Right: pixels remaining after automated editing, and the fitted ellipse. The square indicates the geometric center of the ellipse. A slight change in the azimuth angle of the ellipse is an artifact of the pixel-editing algorithm.

pair of adjacent surfaces we reevaluate the likelihood holding the energy fixed and reducing the charge by one unit for only that pair of surfaces. If the χ^2 is reduced, we assume that an electron attachment has taken place. Finally we repeat the complete maximum-likelihood analysis with the identified charge offsets. Figure 2.12 shows an example of an electron attachment which was automatically identified in the analysis.

In a similar way we are also able to automatically identify "reverse" events. The Trek stacks were oriented with respect to *Mir* such that sheet 1 was furthest from the hull and sheet 16 the closest. A "forward" directed cosmic ray is one which entered the Trek stack passing through sheet 1 first and then proceeding deeper. A "reverse" event is one which entered the Trek stack starting on sheet 16, and incidentally passed through some of *Mir* before reaching the Trek detector. There are two ways to tell the direction of a cosmic ray. First, if the particle is of sufficiently low energy, as it loses energy in the detector, its value of detector response will increase. If x is the depth of the cosmic-ray track in the detector measured along the track and increasing from sheet 1 to sheet 16, then we determine $\mathrm{d}s/\mathrm{d}x$. If $\mathrm{d}s/\mathrm{d}x$ is sufficiently large and negative, we identify the particle as a reverse event. This does not work for high-energy cosmic rays for which $\mathrm{d}s/\mathrm{d}x \approx 0$. However, it is possible to determine direction for relativistic particles which undergo nuclear fragmentation in the detector. The probability of losing one or more charges is much greater than the probability of gaining a charge, and the probability of gaining more than one charge is essentially zero. Thus, if the charge of the particle appears to increase (discontinuously) with increasing x, this is most likely a "reverse" cosmic ray which has lost some charge due to nuclear fragmentation. If neither of these methods suggest a definite direction, we analyze the data in both directions and assign the direction which has the smaller χ^2. Approximately 25% of Extended-Trek events were identified as reverse

events.

2.4.2 Analysis

In Figure 2.12 we show an example of a final Extended-Trek measurement. For each surface, we have measured the signal due to the cosmic ray and performed a calibration scan of the surrounding area. The cosmic-ray signal is corrected using the difference between the calibration signal and a standard value for Au at 10.8 A GeV. We also measure the zenith angle of the event and compute the flight distance of the cosmic ray. The signal-versus-distance data are all that are needed to perform a fit to determine the cosmic-ray charge and energy.

The Extended-Trek data analysis of a single cosmic ray proceeded in these steps:

1. The pixel images of the cosmic-ray etch-pits were automatically edited and ellipses were fitted to the data.

2. The calibration data for each surface were analyzed to find the mean value of b for the two calibration beams as well as the width of the b distribution.

3. The b data from the calibration beams were combined with the zenith-angle measurements (all original Trek data) to produce the calibration value of G, as well as the value of the average calibration signal, s_{cal}.

4. The measured thicknesses were read from data files and cumulatively summed to yield the x values as in Figure 2.12 (when divided by the cosine of the event zenith angle).

5. The calibration correction was performed. In this analysis the calibrated value was given by

$$s'_{\mathrm{e}} = s_{\mathrm{e}} \frac{s_0}{s_{\mathrm{cal}}}. \tag{2.7}$$

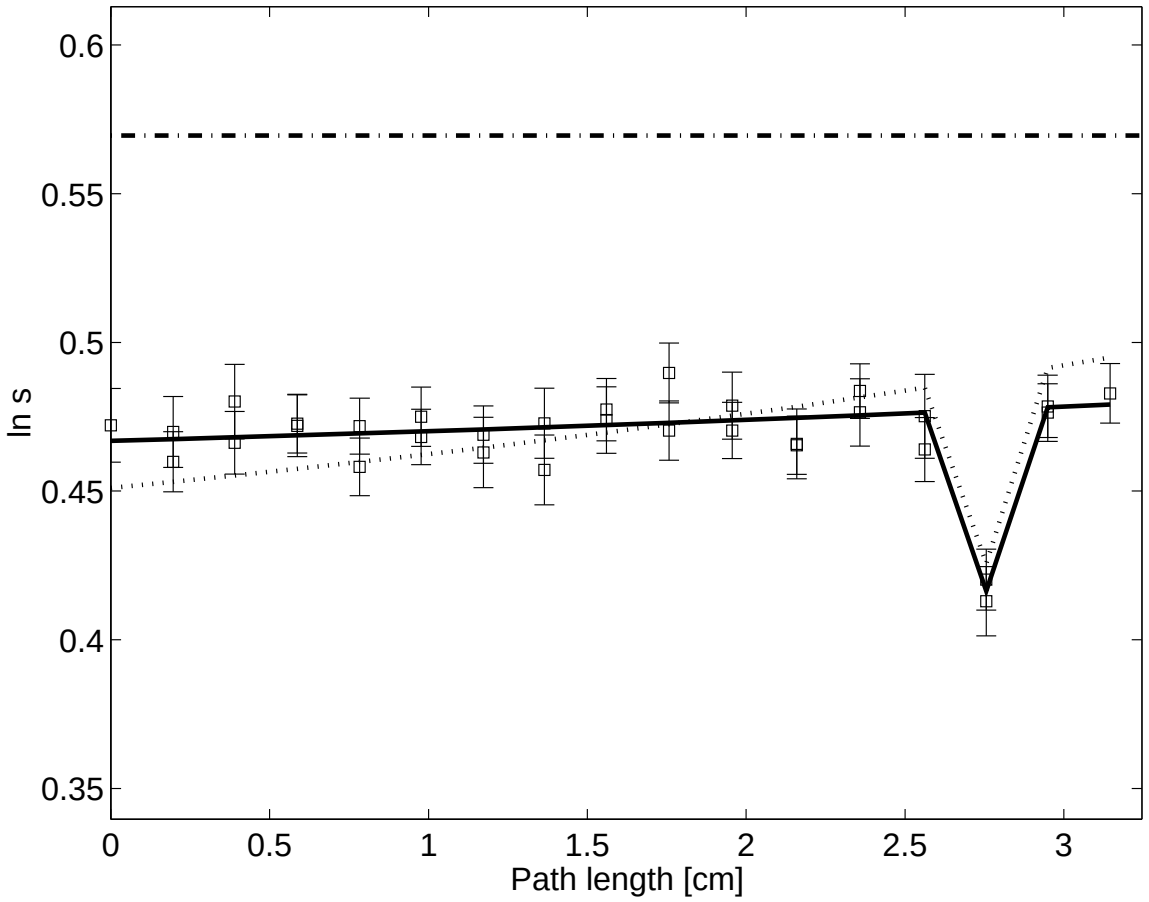

Figure 2.12: Track-etch signal ($\ln s$) plotted versus flight distance in a Trek detector stack for a typical ultra-heavy cosmic ray. Individual measurements are indicated by the square points with error bars. The solid line indicates the expected values for the best-fit charge, Z, and energy. The lower dotted line shows the expected values with the charge fixed at $Z-1$ and with the energy free to vary. The dot-dashed line indicates the values for relativistic Au (the calibration beam). The dip in signal toward the end of the track is due to the temporary attachment of a single orbital electron and was automatically identified during the data analysis.

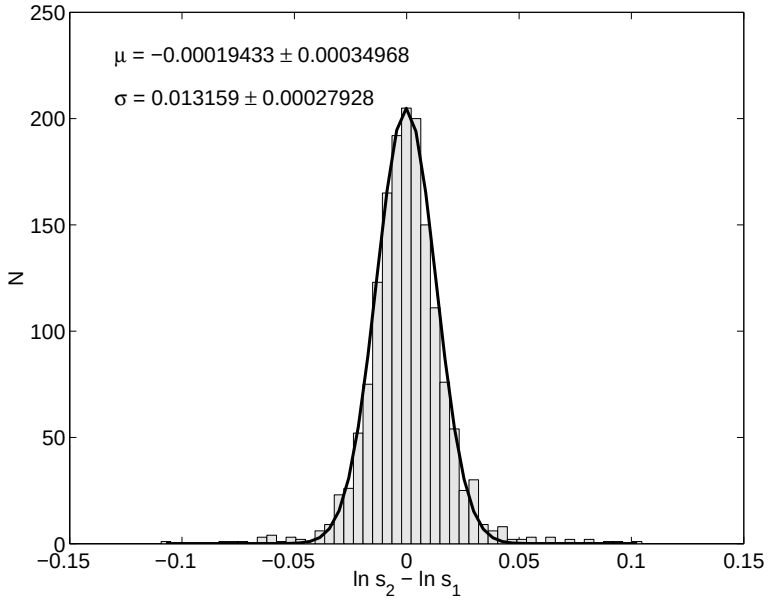

Figure 2.13: Histogram of change in signal on adjacent surfaces.

6. The widths of the calibration peaks were converted into a value of σ_s, and any s-dependent corrections to σ_s were applied (see below).

7. A grid in Z and β was constructed and at each pair, values of s as a function of x were generated. The value of χ^2 could then be calculated for each pair.

8. An acceptable range of Z and β was found by demanding that $\chi^2 - \chi^2_{\text{min}}$ was less than some pre-defined value $\Delta\chi^2$. This range of acceptable values was then used to generate a new grid.

9. The previous two steps were repeated, with $\Delta\chi^2$ reduced at each iteration until $\Delta\chi^2 = 1$ was reached. At that point the value of Z and β assigned to the cosmic ray were those which minimized χ^2 and the upper and lower limits on each value were defined by the contour of $\chi^2_{\text{min}} + 1$.

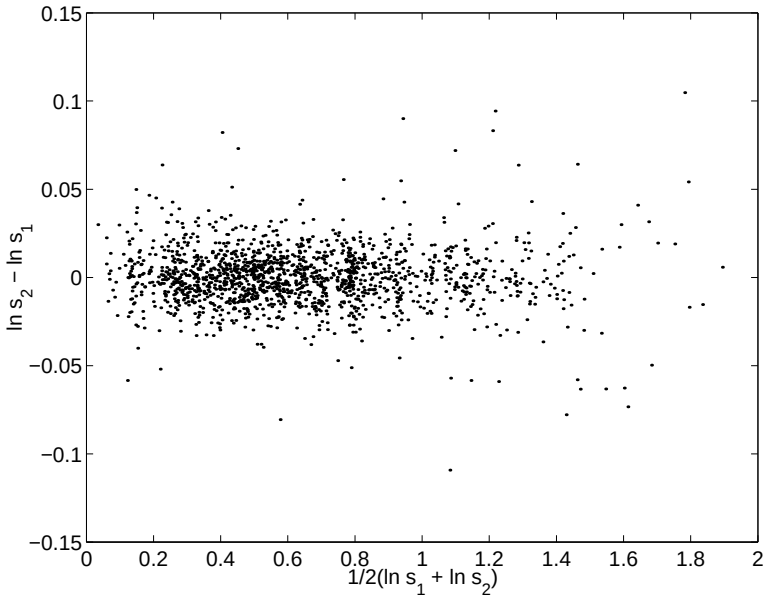

Figure 2.14: Scatterplot of change in signal on adjacent surfaces plotted versus average signal on adjacent surfaces.

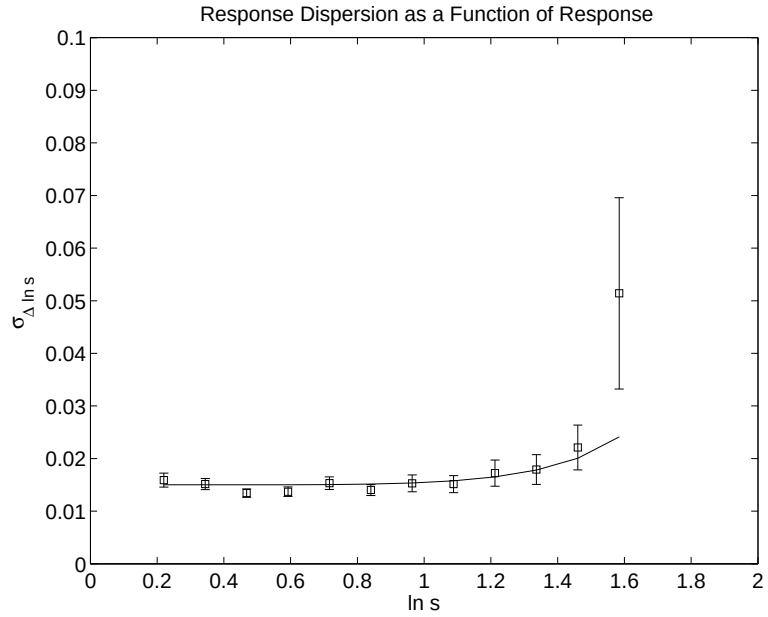

Figure 2.15: Dispersion in change in signal on adjacent surfaces plotted versus average signal. Error bars are statistical. The line indicates a conservative empirical fit described in the main text.

For the first time we had sufficient statistics to measure the dependence of dispersion in $\ln s$ as a function of s. Figure 2.13 shows the histogram of $\Delta \ln s$ across adjacent surfaces for all values of s. In Figure 2.14 these same data are plotted together with $\langle \ln s \rangle = (\ln s_1 + \ln s_2)/2$. The data in Figure 2.14 were then broken down into bins of $\langle \ln s \rangle$ and the dispersion in $\Delta \ln s$ was calculated for each bin. The results are shown in Figure 2.15. For values of $\ln s < 1$, it appears that the dispersion in $\Delta \ln s$ is constant. Indeed, the value $\sigma_{\Delta \ln s}/\sqrt{2}$ is very close to the typical widths of calibration event peaks. Thus for $\ln s < 1$ we are justified in assuming that $\sigma_{\ln s}$ is both independent of s and well characterized by the widths of calibration peaks. However, for $\ln s > 1$, it appears that neither assumption is justified. Using the data in Figure 2.15 (excluding the point with the largest error bar), I obtained the (crude) fit

$$\sigma_{\ln s} = 0.015 \exp\left[0.03 (\ln s)^6\right] / \sqrt{2}, \tag{2.8}$$

and used this value to characterize the error bars for individual cosmic-ray measurements with $\ln s > 1$.

The one trade-off of using multiple calibration beams to measure G is that the values of s for the two beams are "locked" together. That is, the value of s for the high zenith angle calibration beam is equal to that of the low zenith angle calibration beam by assumption and both are then adjusted to equal $s(Z = 79, E = 10.8 \text{ A GeV})$ as determined from the empirical response function. This makes it impractical to perform the analysis of the high zenith angle calibration beam as though it were a cosmic-ray track, as was done in the original Trek analysis.

During the course of measuring initial sheet thicknesses for Extended-Trek, it was found that the thicknesses tended to be correlated within stacks, though not from stack to stack. One way to measure the scale of this phenomenon quantitatively is to look first at the distribution of

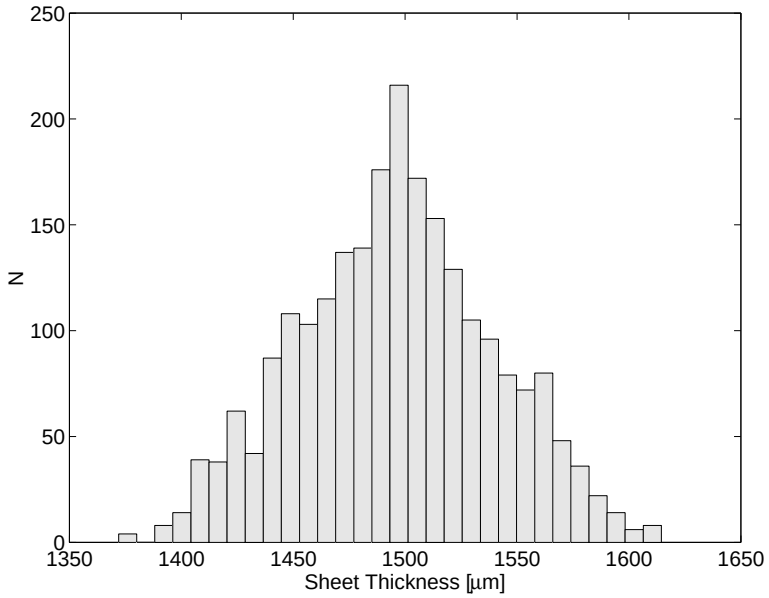

Figure 2.16: Distribution of initial (pre-etch) sheet thicknesses in the Extended-Trek Analysis.

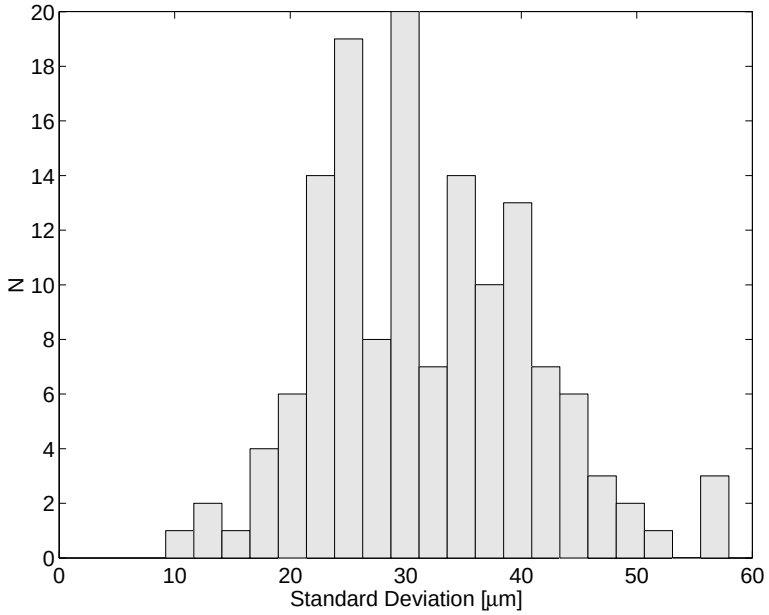

Figure 2.17: Distribution of standard deviation of initial (pre-etch) sheet thicknesses in one stack in the Extended-Trek Analysis.

all sheet thicknesses. This distribution is shown in Figure 2.16. The median value is 1497 μm, and the standard deviation is 44 ± 1 μm. We can then compare the standard deviation of all sheets to the standard deviation within a stack. The distribution of these values is shown in Figure 2.17. The median value of this distribution is 31 ± 3 μm. On average, therefore, there is significantly less dispersion in the thicknesses of sheets within one stack than in the thicknesses of all sheets in all stacks. During the initial Trek analysis, it was assumed that all unmeasured sheet thicknesses would, on average, be 1500 μm. However, as this analysis shows, it would be more appropriate for unmeasured sheet thicknesses in one stack to be set to the median value of all measured sheet thicknesses in that stack. The explanation for the intra-stack correlations is fairly simple. The Trek stacks were assembled from BP-1 glass sheets supplied by Schott Glass. These came in a number of different batches, so it is not too difficult to imagine that sheet thicknesses were all very similar within one batch, but fluctuated from batch to batch. The Trek stacks were then assembled directly from the batches, not from a randomized pool of glass, so they would have retained any batch-scale thickness correlations.

2.4.3 Extended-Trek Error Analysis

In much the same way as the original Trek analysis we performed Monte Carlo simulations of the detector in the Extended-Trek configuration using measured values of dispersion in various parameters to generate dispersions in charge. The Monte Carlo simulation was performed using actual Extended-Trek charges and energies but with six times the statistics. Many of the sources of dispersion are the same as in the original Trek analysis. Though the magnitudes are mostly the same, the contribution to charge dispersion is reduced by the increased statistics.

There are two new effects in Table 2.3, namely “missing” surfaces and “walk-offs.” Miss-

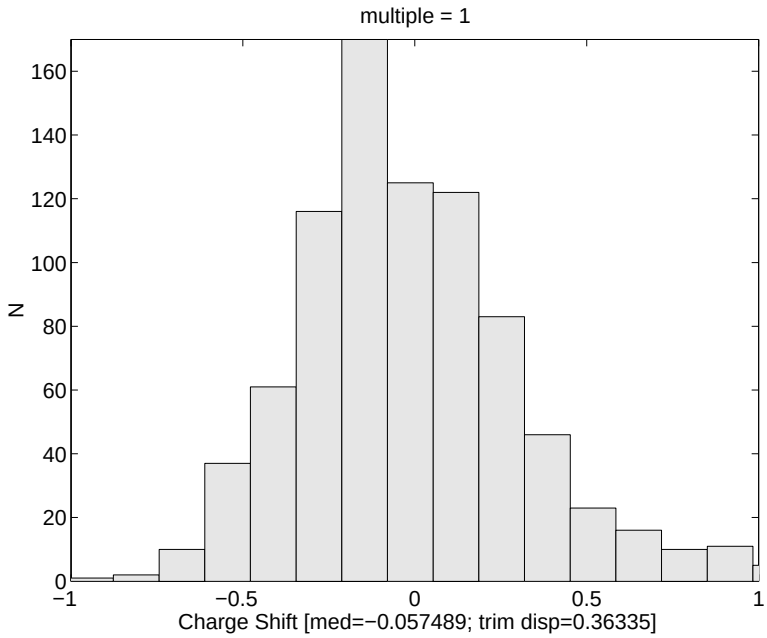

Figure 2.18: Monte Carlo simulation of charge dispersion with multiple errors.

ing surfaces are those surfaces which, for one reason or another, could not be included in the analysis. For example, a wafer may have shattered during coring, or the etch-pit of the cosmic ray was masked by some surface defect. The average number of analyzable surfaces is consistent with roughly 5% missing surfaces, not counting walk-offs, which is the magnitude included in Table 2.3. The walk-offs are events which fragmented completely in the detector or which passed off the edge of the detector. In other words, these are a special category of missing surfaces in which after some number of surfaces all subsequent surfaces are missing.

The effects of electron capture and nuclear fragmentation have been eliminated from consideration since we now have full coverage of the cosmic-ray track. These effects are extremely easy to identify and correct, and so should not make a significant contribution to charge dispersion.

The Monte Carlo simulation with multiple errors is shown in Figure 2.18. In this simula-

tion, instead of finding the contribution of individual error sources, all the error sources are included to find the total expected charge dispersion.

2.4.4 Results

The histogram of measured charges is shown in Figure 2.19. This includes all events passing the cuts $E > 900$ A MeV, $Q(\chi^2|\nu) > 0.001$, $Z > 71$, and $Z < 84$. The charge cuts removed only two outliers, which, at least in the case of the high charge event, was probably mis-identified due to poor statistics (the event was close to the edge of a stack and "walked off"). Altogether 121 out of 146 (83%) Extended-Trek events passed these cuts. For comparison I also show the charge histogram of original Trek analysis data in Figure 2.20 with the same cuts applied, and the same bin size. It should be readily apparent to the unaided eye that the charge resolution has improved in the Extended-Trek analysis. The peaks at Os and Pb are particularly diagnostic in this case.

To find the observed abundance the histogram in Figure 2.19 was fitted to a series of Gaussians with peaks at integer charges between 72 and 83 and with resolutions between 0.3e and 0.4e. The fitted charge distribution was then compared with the data in the Kolmogorov-Smirnov test (see Appendix A). The best fit to the observed data was with a charge resolution of 0.35e, which is consistent with the resolution obtained from the Extended-Trek error analysis. The charge histogram with the fitted Gaussians is shown in Figure 2.21. The results of the Kolmogorov-Smirnov test are shown in Figure 2.22. The value of χ^2 reported in the figure is the value recommended for binned data with low statistics [26], namely

$$\chi^2 = 2\sum_k (y(x_k) - y_k) + y_k \ln\left(\frac{y_k}{y(x_k)}\right), \tag{2.9}$$

where y_k is the number of events in the kth bin and $y(x_k)$ is the model prediction for that bin. When

Source of Dispersion	Magnitude	Contribution to Dispersion (e)
Response fluctuations		
G random error (0.26 μm)	$\sigma_{\ln s}(G) = 0.0057$	(0.084)
b random error (0.025 μm)	$\sigma_{\ln s}(b) = 0.0013$	(0.021)
inferred intrinsic dispersion	$\sigma_{\ln s} = 0.0093$	(0.129*)
measured, adjacent surfaces	$\sigma_{\ln s} = 0.011$	0.155
Zenith angle errors		
index of refraction (0.2%)	0.073°	(0.018)
x,y random error (0.7 μm)	0.037°	(0.009)
z random error (1.7 μm)	0.064°	(0.010*)
multiple Coulomb scattering	0.091°	(0.023)
non-parallel sheet surfaces	0.025°	(0.009)
measured value	0.14°	0.025
Calibration errors		
statistics	≈ 0.014 μm	0.017
focus	< 2 μm	< 0.022
illumination	< 0.04 μm	< 0.01
anellipticity	0.3%	< 0.01
Thermal effects		
registration temperature variation	< 10°C	< 0.04
track fading after corrective anneal	4.2 yr at 20°C	0.198
Other contributions		
thickness random error	2 μm	< 0.01
straggling	—	0.005
missing surfaces	5%	0.032
walk-offs	2%	0.23
isotopic spread	0.58 amu	0.01
Expected charge resolution (quadrature)		0.35
Simulated charge resolution (multiple errors)		0.36

*Estimated or inferred

Table 2.3: Contributions to dispersion in the measurement of charge in the Extended-Trek Analysis. All magnitudes were measured unless otherwise indicated. Indented values are contributions to the measured values.

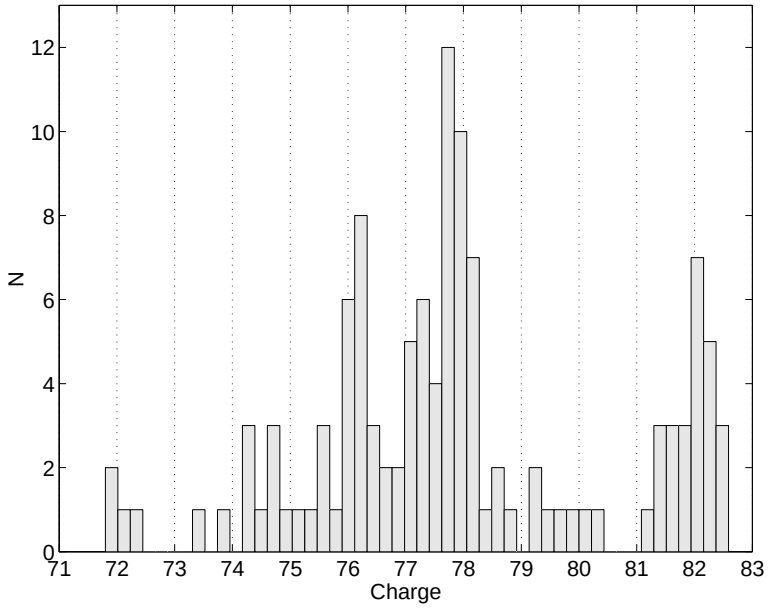

Figure 2.19: Charge histogram for the Extended-Trek analysis.

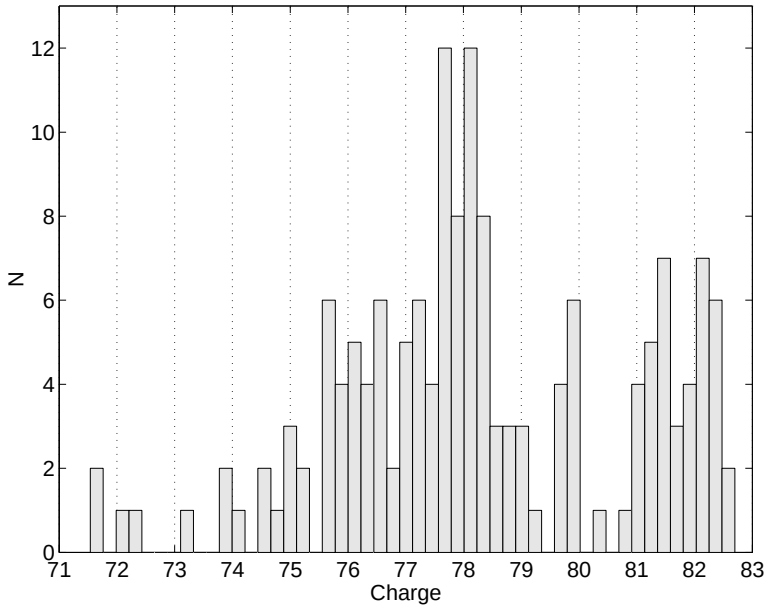

Figure 2.20: Charge histogram for the original Trek analysis with the same cuts as applied to the Extended-Trek analysis.

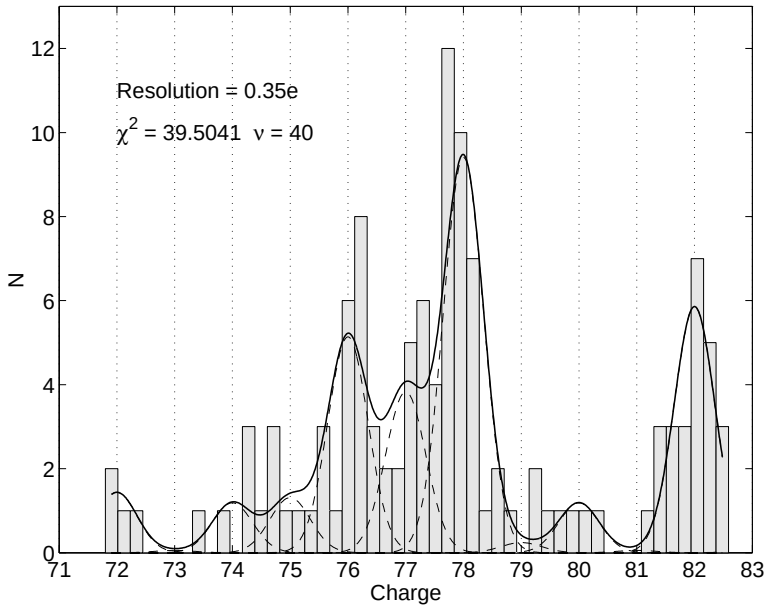

Figure 2.21: Charge histogram for the Extended-Trek analysis with fits to observed abundances.

$y_k = 0$, the second term is zero.

To obtain the uncertainty in the fitted abundances, Monte Carlo distributions based on the fitted abundances were generated and fitted with the same procedure. The statistical uncertainty was determined from 63% lower and upper limits in the Monte Carlo simulation subtracted from the mean value of the abundances in the different resolution models. The systematic uncertainty was determined from the maximum and minimum abundances in the different resolution models subtracted from the mean values. The observed abundances are shown in Table 2.4.

To account for detector acceptance, the fits were repeated and the fitted abundances corrected for acceptance. The acceptance models were defined by the minimum detectable semi-minor axis b_{min}, which took on the values 5 μm and 10 μm. The corrected abundances are shown in Table 2.5. For comparison I show the acceptance-corrected abundances from the original Trek analysis

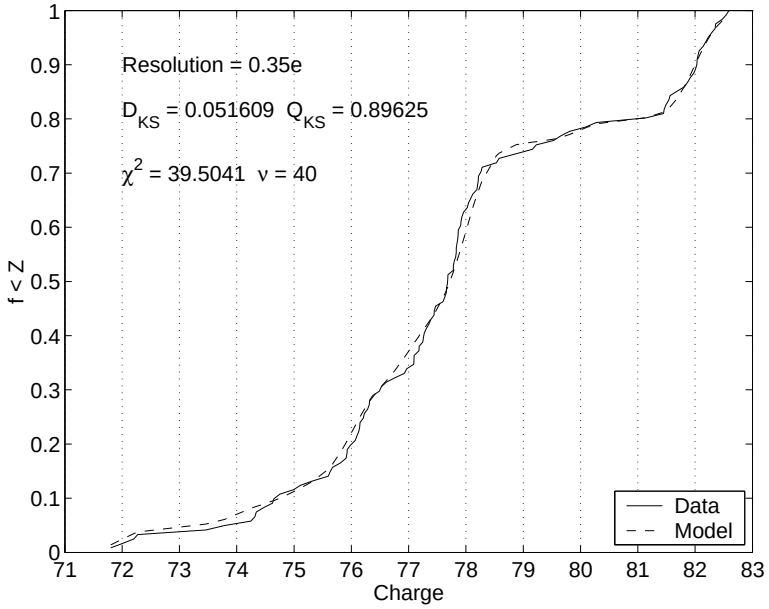

Figure 2.22: Plot of the Kolmogorov-Smirnov test applied to the fit to observed Extended-Trek abundances with a resolution of 0.35*e*.

Element	Observed Abundance
Hf	$0.073^{+0.028}_{-0.006}(\text{stat.})^{+0.002}_{-0.001}(\text{syst.})$
W	$0.061^{+0.014}_{-0.016}(\text{stat.})^{+0.003}_{-0.002}(\text{syst.})$
Os	$0.257^{+0.031}_{-0.031}(\text{stat.})^{+0.006}_{-0.007}(\text{syst.})$
Ir	$0.190^{+0.036}_{-0.038}(\text{stat.})^{+0.006}_{-0.009}(\text{syst.})$
Pt	$0.471^{+0.027}_{-0.036}(\text{stat.})^{+0.030}_{-0.031}(\text{syst.})$
Hg	$0.062^{+0.011}_{-0.014}(\text{stat.})^{+0.006}_{-0.003}(\text{syst.})$
Pb	$0.294^{+0.031}_{-0.028}(\text{stat.})^{+0.022}_{-0.023}(\text{syst.})$

Table 2.4: Observed abundances in the Extended-Trek analysis. All abundances are relative to the Pt-group: $75 \leq Z \leq 79$.

Element	Abundance at Detector
Hf	$0.164^{+0.061}_{-0.018}(\text{stat.})^{+0.016}_{-0.015}(\text{syst.})$
W	$0.085^{+0.019}_{-0.023}(\text{stat.})^{+0.007}_{-0.005}(\text{syst.})$
Os	$0.279^{+0.031}_{-0.033}(\text{stat.})^{+0.011}_{-0.011}(\text{syst.})$
Ir	$0.190^{+0.036}_{-0.031}(\text{stat.})^{+0.007}_{-0.011}(\text{syst.})$
Pt	$0.438^{+0.028}_{-0.041}(\text{stat.})^{+0.032}_{-0.032}(\text{syst.})$
Hg	$0.052^{+0.009}_{-0.012}(\text{stat.})^{+0.006}_{-0.004}(\text{syst.})$
Pb	$0.227^{+0.023}_{-0.020}(\text{stat.})^{+0.023}_{-0.023}(\text{syst.})$

Table 2.5: Observed abundances in the Extended-Trek analysis corrected for detector acceptance. All abundances are relative to the Pt-group: $75 \leq Z \leq 79$.

in Table 2.6.

Since the observed abundances are consistent with the original Trek analysis, the results [18] in terms of source abundances still stand. The abundance of Hg is slightly lower, but this does not significantly change the results of [18]. The observation of a depletion of Ir relative to Os is confirmed. Chapter 5 discusses the depletion of Ir in greater detail. There is no way to find the source abundance of Ir since the propagation-corrected point-spread-function of Ir is strongly peaked at Pt, thus the point-spread-function of Pt will look very similar to that of Ir. This degeneracy leads to an intrinsic numerical instability in the derivation of source abundances.

Ratio	Abundance at Detector
Os	$0.38^{+0.06}_{-0.05}(\text{stat.})^{+0.07}_{-0.03}(\text{syst.})$
Ir	< 0.21
Pt	$0.48^{+0.04}_{-0.06}(\text{stat.})^{+0.02}_{-0.01}(\text{syst.})$
Hg	$0.12^{+0.03}_{-0.04}(\text{stat.})^{+0.01}_{-0.02}(\text{syst.})$
Pb	$0.29^{+0.05}_{-0.06}(\text{stat.})^{+0.01}_{-0.02}(\text{syst.})$

Table 2.6: Observed abundances in the original Trek analysis corrected for detector acceptance. All abundances are relative to the Pt-group: $75 \leq Z \leq 79$.

2.5 Maximal Sampling

Track-etch detectors traditionally consist of stacks of separate sheets of the detector material. For BP-1 detectors, the detectors have been manufactured with thicknesses between 700 and 1500 μm. Suppose that after a round of etching and analysis, the glass is ground to remove ~ 50 μm of material from each surface. In addition to the material removed by previous etching, typically 50 μm, the grinding results in a new sheet which will be roughly 200 μm thinner. Now the glass is repolished and reetched, revealing a new set of etch-pits. We refer to the combined action of grinding and polishing as *resurfacing*. In this way, portions of the track *within* a sheet of glass can be sampled, in addition to the portion of the track closest to the original surface of the glass. BP-1 in 1-inch diameter wafers becomes too fragile for safe handling when its thickness is less than ~ 500 μm. Thus, in principle, a 1500 μm thick BP-1 wafer could be etched and analyzed five times before handling became too difficult. Since we make measurements on both the top and bottom surfaces, this gives 10 measurements *per sheet*. A cosmic ray analyzed in this way is thus said to be

Event	Z	β	χ^2	d.o.f.	$Q(\chi^2\|\nu)$
Before resurface	75.488 ± 0.166	0.946 ± 0.002	21.571	29	0.837
After resurface	75.594 ± 0.17	0.946 ± 0.002	30.401	26	0.251
Combined data	$75.497^{+0.173}_{-0.152}$	$0.946^{+0.002}_{-0.001}$	39.029	40	0.513

Table 2.7: Comparison of charge and energy measurement for the same cosmic-ray event before and after resurfacing and with a combined before and after dataset.

maximally sampled.

During the course of the preliminary test-etching for Extended-Trek, a few sets of wafers became frosted (see §2.6). In addition, two Extended-Trek events were at such high zenith angle, and thus so close to threshold, that minor fluctuations in etch rate made these events difficult to analyze. For these reasons, we decided to attempt to resurface these wafers with our recently acquired Buehler Ecomet-3 grinder-polisher.

Fortuitously, one of the two high zenith angle events passed very near another cosmic-ray track. Thus, some of the wafers to be resurfaced for this event contained a second cosmic-ray track. Since this second event was well above threshold, it could be analyzed both before and after resurfacing. Naturally, we analyzed the before and after data in the standard 32 surface configuration. In addition, it proved possible to combine the data into a single 64 surface configuration. Table 2.7 shows the results of these three measurements. Figure 2.23 shows the combined data in the 64 surface analysis. Since only seven of the ten Extended-Trek wafers were actually resurfaced, only a maximum of 46 surfaces were actually available. The act of resurfacing a glass track etch detector appears to have no measurable effect on the measurement of cosmic-ray charge whether the resurfaced data are considered separately or combined into a larger dataset.

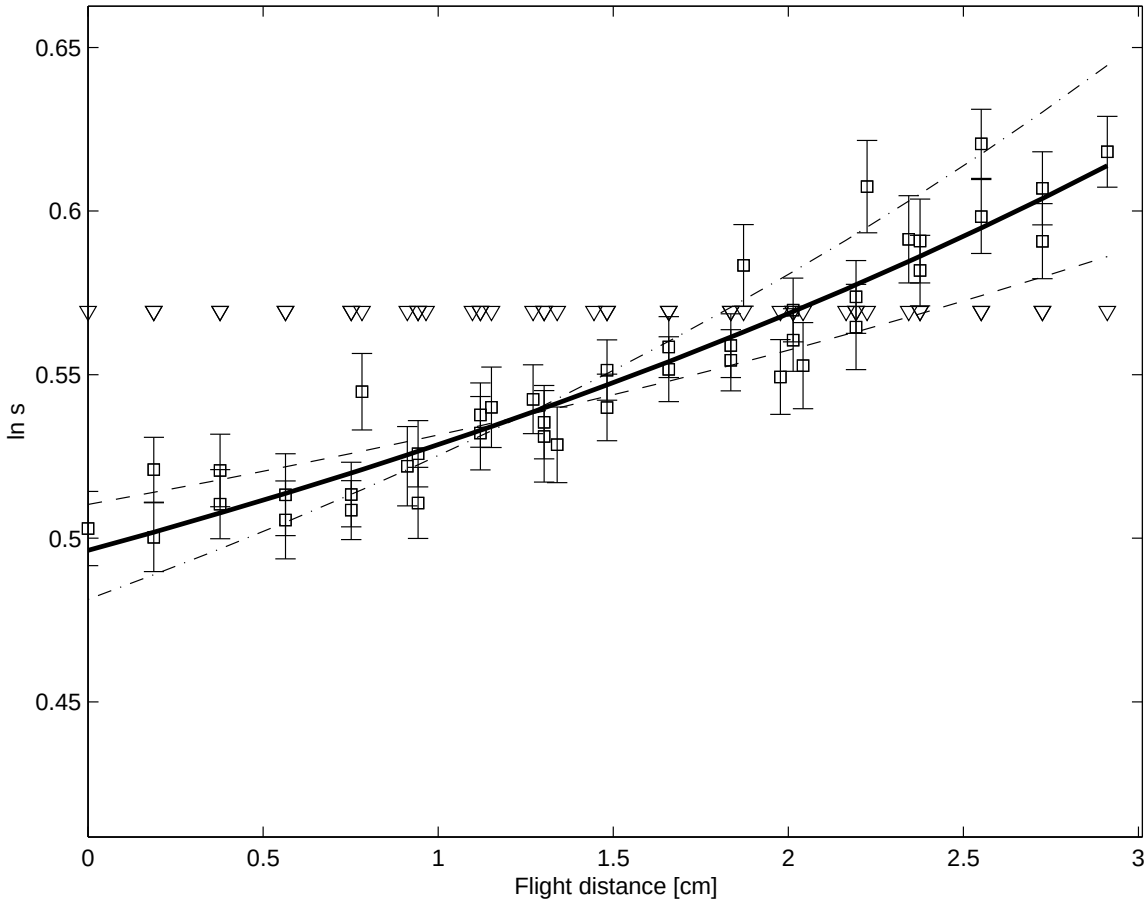

Figure 2.23: Combined data from a cosmic-ray track which was measured both before and after resurfacing. Triangles indicate the response of the calibration beam. The solid line represents the track of a particle with the best-fit charge and energy. The dashed line represents the track of a particle with an additional unit of charge, while the dot-dash line represents the track of a particle with charge reduced by one unit.

2.6 Etch Instabilities

During the course of the Extended-Trek analysis, a number of interesting etch instabilities were discovered (or possibly re-discovered). All of these instabilities appeared in HF etches. I list them here along with some of their apparent causes so that they may be avoided in the future.

2.6.1 Frosting

During the test etches in preparation for Extended-Trek, the biggest surprise was the discovery of frosting. A frosted piece of glass looks exactly like the name suggests. Under the microscope, the bulk surface away from any etch pits appears broken up into tiny bowls each a few microns in size. In addition, these tiny bowls appear within other etch pits and the normally smooth etch pit mouths are broken up and jagged. This pits-within-pits feature is probably the most telling characteristic of frosting and can often be detected under the microscope before frosting becomes apparent to the naked eye. Frosting is a bulk effect, in that if an etch is contaminated, all the glass in the tank will be frosted, although there may be regions on the glass in which the severity of the frosting appears correlated with the geometry of the frame or string holding the glass.

The primary, although almost certainly not the only, cause of frosting appears to be Teflon used for etch frames—specifically, Teflon freshly machined from new stock or purchased already machined (in the case of nuts and threaded rod). It is not known if this is due to the surface or the bulk of the Teflon. Older Teflon which has been used in etches for many years does not appear to cause frosting, although frosting has appeared in etches in which old Teflon was used. Not all new Teflon causes frosting. In particular, Teflon thread does not appear to cause frosting in any situation. Interestingly enough, Teflon thread is transparent with a slightly bluish tint, while the

Teflon used for etch frames is opaque white and has a slightly different consistency which is most readily apparent when it is cut with a sharp knife or razor. This leads me to speculate that some sort of dye or additive is at fault rather than the Teflon itself.

This particular cause of frosting was avoided by making all etch frames out of polyethylene. However, this is not an ideal solution since polyethylene is buoyant in HF. Furthermore, since frosting has appeared in etches with old Teflon or no Teflon at all, it seems likely that other contaminants may also cause frosting. It is even possible that certain types of latex gloves may have surface coatings which can contaminate an etch and cause frosting. Vinyl gloves show no sign of causing frosting. Thus a high degree of cleanliness and attention to detail may also be important in avoiding frosting.

2.6.2 Pseudo-Frosting

A small number of wafers from the first large Extended-Trek etch appeared to be frosted in patches. However, since frosting is a bulk effect which effects all glass in an etch, this was something different. For lack of a better term, this was dubbed “pseudo-frosting.” The pattern of the pseudo-frosted patches suggests a smear of some sort of contaminant, possibly organic, was present on the Trek sheet prior to coring. The second round of wafers were subjected to more thorough cleaning, including a soak in ethanol prior to a wash with soap. No pseudo-frosting was observed in this etch.

2.6.3 Comets

Comets are aptly named. Typically, an etch comet consists of a “head” of dimension $\sim 100\ \mu$m which appears very roughly etched, almost as though frosted, and additionally raised

above the surrounding surface. This is often accompanied by a “tail” which may be up to a few millimeters in length which appears similar but is less raised above the surface. Comets are very much more likely to appear on glass etched in unstirred tanks, suggesting that a small contaminant, such as a bit of organic material or dust, disrupted normal etching at a point and was not washed away by the flow of etchant.

2.7 Conclusion

It should now be clear that many of the advances needed for the analysis of next-generation track-etch detectors have already been achieved. The improvement in charge resolution has been demonstrated. Without significant changes in design, ECCO will probably be able to improve the resolution even further. Since the detector modules will be so large, the probability of walk-offs will be greatly reduced, although not entirely eliminated, since this category also includes events which fragment completely in the detector. This category could also be eliminated by only analyzing events which penetrate the detector completely. Detailed recommendations for ECCO are discussed in Chapter 6.

Chapter 3

Energy Loss of Heavy Ions in Matter

Is he a dot, or is he a speck?
When he's underwater, does he get wet?
Or does the water get him instead?
Nobody knows
Particle Man
— "Particle Man," *Flood* (1990)

3.1 Introduction

The simultaneous determination of charge and energy of a particle passing through a solid state detector, for example a track-etch detector, requires knowledge of the rate of energy loss, $\mathrm{d}E/\mathrm{d}x$, as a function of charge and energy. As a practical example, consider the measurement of the charge and energy of a cosmic ray from signal measurements in a stack of detectors. For a number of combinations of charge and initial energy, we calculate the values of $\mathrm{d}E/\mathrm{d}x$ along a track, and, by straightforward integration, use these values to predict the energies along the track. With the values charge and energy as a function of distance, we predict the detector response using an empirically determined response function. The character of this response function will be discussed

in Chapter 4. The predicted response is compared to the measured response, and the best value of charge and energy is found by maximum likelihood.

Provided beams of known charge and energy are available, it is usually straightforward to determine the response function $s(Z,\beta)$. The calculation of $\mathrm{d}E/\mathrm{d}x$, however, is a subject fraught with difficulty. Previously, we have relied on what amounts to a polynomial fit to empirical determinations of range as a function of energy. This method is described in Benton and Henke [24], which is itself an extension of the work of Barkas and Berger [27]. The code which results from this technique is extremely fast, since no integrals are involved. However, there is no evidence of comparison with ion ranges for species above ^{40}Ar. The extrapolation to higher charge is especially complicated by the increasing probability of ion shielding due to orbital electron capture. To address this deficiency I have investigated the theory of energy loss of charged particles in matter. Since there are many phenomena which must be included in a complete description of energy loss, and since these phenomena are described in many different publications over many decades, I have also collected here the mathematical expressions of these phenomena with modern and uniform notation. As I will show, good agreement with experimental results and with tables of extrapolated empirical ranges can be obtained with code constructed purely from theoretical considerations.

It is important to emphasize that a poor understanding of $\mathrm{d}E/\mathrm{d}x$ does not preclude the measurement of charge. It is always possible to simply apply empirical techniques: for example, a plot of detector signal versus total range (distance from stopping point) will resolve itself into bands of charge provided the intrinsic charge resolution of the detector is adequate. Alternatively, detector signal may be measured for beams of known charge and energy and compared directly to unknown signals in the same detector. However, if one wishes, for example, to use a target to reduce

the energy of an accelerator beam to a value which would otherwise be unavailable, precise $\mathrm{d}E/\mathrm{d}x$ calculations are necessary. More abstractly, it is probably not likely that in the foreseeable future there will be empirical measurements of the total range in all detector materials for all elements with energies of interest to cosmic-ray researchers. In this case, it is appropriate to seek theoretical guidance in improving $\mathrm{d}E/\mathrm{d}x$ calculations.

The review of Ahlen [28] on stopping powers must stand as the starting point for any modern calculation. It is particularly interesting to note that calculations of stopping power for uranium ions were confirmed in an experiment by Ahlen and Tarlé [29]; therefore, any modern calculation should reproduce this result.

3.2 Theory of Stopping Power

3.2.1 The Overall Form

The overall form of the stopping-power formula can be obtained from classical arguments [30]. In SI units, that formula is

$$-\frac{\mathrm{d}E}{\mathrm{d}x} = \frac{Z_1^2 e^4 n_\mathrm{e}}{4\pi\varepsilon_0^2 m_\mathrm{e} v^2} L. \tag{3.1}$$

Here, we have used Z_1 for the charge of the ion, and m_e and n_e are the electron mass and number density, respectively. The minus sign on the left hand side is simply a reminder that the stopping power is the energy *lost* by the particle and therefore a negative quantity. The factor L is the stopping logarithm, defined classically by

$$L = \ln \frac{b_\mathrm{max}}{b_\mathrm{min}}, \tag{3.2}$$

that is, the logarithm of the ratio of maximum to minimum impact parameters. More typically we wish to use units of A MeV g^{-1} cm^2, ("A MeV" is to be read "MeV per nucleon") in which case this becomes

$$-\frac{dE}{dx'} = 4\pi N_A m_e c^2 r_e^2 \frac{Z_1^2 Z_2}{A_1 A_2} \frac{1}{\beta^2} L, \tag{3.3}$$

where we have made the replacements $x \to x' = \rho x$ and $\beta = v/c$. Here, Z_2 and A_2 are the atomic number and atomic mass, respectively, of the target material, A_1 is the atomic mass of the projectile, N_A is Avogadro's number, and $r_e = e^2/4\pi\varepsilon_0 m_e c^2$ is the classical electron radius.

The devil, they say, is in the details. In this case, the detail is the stopping logarithm L. Following Lindhard and Sørensen [31], we set

$$L_0 = \ln\left(\frac{2m_e c^2 \beta^2 \gamma^2}{I}\right) - \beta^2 - \frac{\delta}{2}. \tag{3.4}$$

This is the form derived originally from quantum perturbation theory, and the first two terms are typically called the Bethe result. The third term is the density effect (see §3.2.3). The notation, $-\delta/2$, for the magnitude of the density effect, is historical. Here, I is the effective ionization potential of the target material. Although there are theoretical means to determine I, the experimentalist should regard it as an empirical parameter. Throughout what follows, I will refer to the form $L = L_0$ as the "Bethe" form of dE/dx.

For an accurate calculation, further corrections of the form $L = L_0 + \Delta L$ are required. It will be useful here to define the quantity

$$\eta \equiv \frac{\alpha Z_1}{\beta}, \tag{3.5}$$

where $\alpha = e^2/4\pi\varepsilon_0 \hbar c$ is the usual fine-structure constant. It is most desirable to find formulae for ΔL which will be valid for all values of η. In particular, for uranium, $\eta > 1$ when $\beta < 0.671$! Thus, any

formula which loses validity for $\eta > 1$ will be hopeless for describing the energy loss of uranium ions in matter.

3.2.2 Composite Materials

Often we must deal with target materials which are not pure elements. Glasses, plastics, and alloys are all common targets. For these, stopping power may be calculated by the so-called Bragg rule: *The total stopping power is the sum of the stopping powers due to each element in the target* [32]. Since it is the number of electrons which is important in stopping, it is most sensible to start with the expression (3.1) which contains the electron number density explicitly.

Consider a target containing a variety of elements, with the *i*th element present in mole fraction $f_i = N_i/N$, where N is the total number of atoms in the sample. In order to simplify the stopping power calculation for such a target, we define an effective electron number density n_{e} for the sample. Since $n_{\mathrm{e}_i} = Z_i n_i$, we can use the Bragg sum to define

$$n_{\mathrm{e}} \equiv Z_2 n = \sum_i Z_i n_i. \tag{3.6}$$

Obviously $n_i/n = f_i$, therefore the effective n_{e} is represented simply by

$$Z_2 = \sum_i f_i Z_i. \tag{3.7}$$

While this may seem like belaboring the obvious, it is intended to avoid careless application of the Bragg rule. Once we have performed the Bragg sum we may then wish to convert the energy loss per unit length measured in cm into energy loss per unit measured in g cm^{-2}. We do this by dividing by the total density ρ of the material. We then define

$$A_2 \equiv \rho N_{\mathrm{A}}/n. \tag{3.8}$$

From this definition it is possible to derive

$$A_2 = \sum_i f_i A_i. \tag{3.9}$$

It may happen that we know the mass fractions w_i of the constituents rather than the number fractions. The conversion between them is given by $f_i = A_2 w_i / A_i$, with the alternative self-consistent expression for A_2:

$$\frac{1}{A_2} = \sum_i \frac{w_i}{A_i}. \tag{3.10}$$

In addition, it is possible to show

$$\left\langle \frac{Z}{A} \right\rangle = \sum_i w_i \frac{Z_i}{A_i} = \frac{\sum_i f_i Z_i}{\sum_i f_i A_i} = \frac{Z_2}{A_2}, \tag{3.11}$$

while if the Bragg rule had been applied incorrectly, we might have been led to conclude

$$\left\langle \frac{Z}{A} \right\rangle = \sum_i f_i \frac{Z_i}{A_i} \text{ (INCORRECT!)} \tag{3.12}$$

The most important application of the Bragg sum rule is the derivation of the effective mean ionization potential for composite materials:

$$Z_2 \ln I = \sum_i f_i Z_i \ln I_i. \tag{3.13}$$

It has been recommended [33] that the value $I_i = 1.13 I_i^{\mathrm{E}}$ be used in (3.11), where I_i^{E} is the value of I used for the pure element.

3.2.3 The Density Effect

Although I have included the density effect as part of the "Bethe" form of the total stopping power, it is worthwhile to discuss it separately since it is important to the discussion of relativistic rise. Unlike many high-energy corrections, the density effect can actually be at least qualitatively

derived in classical electrodynamics. Such a derivation may be found in Jackson [30]. In dense media, the field which perturbs electrons far from the projectile track is modified by the dielectric polarization of the atoms between the distant electron and the projectile. The magnitude of the density effect was originally calculated by Fermi [34] and extended by Sternheimer and Peierls [35].

In this section we follow the historical notation of Sternheimer and Peierls [35] and define $X \equiv \log_{10}(\beta\gamma)$. At high energies, the density effect correction has the form

$$-\frac{\delta}{2} = -(\ln 10)\,X + \ln\frac{I}{\hbar\omega_p} + \frac{1}{2}, \tag{3.14}$$

where ω_p is the plasma frequency of the medium. The density effect reduces the relativistic rise from $\sim \ln\gamma^2$ to $\sim \ln\gamma$ and substitutes the plasma frequency for the mean ionization potential. At somewhat lower energies, the density effect is more complicated, but typically a parametric fit to the full density effect can be obtained. This parameterization was developed by Sternheimer and Peierls [35] and takes the form

$$-\frac{\delta}{2} = -\frac{1}{2}\delta_{\text{high}} - \frac{a}{2}\left[X_1 - X\right]^m \ (X_0 < X < X_1)\,, \tag{3.15}$$

where X_0, X_1, a, and m are parameters which depend on the medium, and δ_{high} can be obtained from (3.14). Typically, $X_0 \approx 0.1$, $X_1 \approx 3$, $a \approx 0.1$, and $m \approx 3$. In addition, there is a small low-energy density effect for conductors:

$$-\frac{\delta}{2} = -\frac{1}{2}\delta(X_0)\,10^{2(X-X_0)} \ (X \le X_0), \tag{3.16}$$

with the additional parameter $\delta(X_0) \approx 0.1$. For insulators, $\delta = 0$ for $X \le X_0$. The most recent available tabulations of these density effect parameters may be found in [36]. Recent advances in computing power have made this parameterization essentially obsolete except for historical pur-

poses. The density effect may now be computed by direct tabular interpolation for a single medium or by computing the complete density effect *a priori* [37].

3.2.4 The Bloch Correction

This correction was derived by Bloch [38] in an investigation of the similarities and differences between classical and quantum-mechanical range-energy calculations. The full story can be found in Ahlen [28]. This correction may be placed in the form

$$\Delta L_{\text{Bloch}} = \psi(1) - \text{Re}\psi(1+i\eta), \tag{3.17}$$

where

$$\psi(z) \equiv \frac{d}{dz}\ln\Gamma(z). \tag{3.18}$$

The numerical value of $\psi(1) = -0.5772157\ldots \equiv -\gamma_E$ is the negative of Euler's Constant.

Although there are robust and highly accurate algorithms for computing values of the Gamma function, it is somewhat simpler to implement the Bloch correction as a sum, which can take two forms:

$$\begin{aligned} \Delta L_{\text{Bloch}} &= \sum_{l=1}^{\infty}\left[\frac{l}{l^2+\eta^2} - \frac{1}{l}\right] \\ &= -\eta^2\sum_{l=1}^{\infty}\left[\frac{1}{l}\frac{1}{l^2+\eta^2}\right]. \end{aligned} \tag{3.19}$$

These are, of course, exactly equivalent. The second form of (3.19) suggests a common approximation to the Bloch correction. If η is small, the sum can be approximated by $\zeta(3) = 1.202057\ldots$, and thus we find a form frequently encountered:

$$\Delta L_{\text{Bloch}} \simeq -1.202\eta^2 \ (\eta \ll 1). \tag{3.20}$$

3.2.5 The Mott Correction

Corrections to the stopping power of order higher than Z^2 at high energies first became apparent a few decades ago [39, 40]. The origin of these higher-order corrections is simply the Dirac equation which is, after all, the correct theory of the electron and the Mott cross section is most appropriate for discussing the scattering of electrons off of highly charged nuclei. Ahlen [41] calculated a correction to stopping power using a parameterization of the Mott cross section derived by Doggett and Spencer [42] and Curr [43]. Here I give the form rederived by Ahlen [44]:

$$\begin{aligned} 2\Delta L_{\text{Mott}} &= \eta\beta^2\left[1.725+\left(0.52-2\sin^2\frac{\theta_0}{2}\right)\pi\cos\chi\right] \\ &\quad +\eta^2\beta^2\left(3.246-0.451\beta^2\right) \\ &\quad +\eta^3\beta^3\left(1.552\beta+0.987/\beta\right) \\ &\quad +\eta^4\beta^4\left(4.569-0.494\beta^2-2.696/\beta^2\right) \\ &\quad +\eta^5\beta^5\left(1.254\beta+0.222/\beta-1.170/\beta^3\right). \end{aligned} \tag{3.21}$$

Note the factor of two in front of the ΔL_{Mott}. The parameter θ_0 is the same as in the Ahlen correction described in §3.2.6. Also

$$\cos\chi = \text{Re}\left[\frac{\Gamma\left(\frac{1}{2}-i\eta\right)\Gamma(1+i\eta)}{\Gamma\left(\frac{1}{2}+i\eta\right)\Gamma(1-i\eta)}\right]. \tag{3.22}$$

This can be placed in a somewhat more tractable form. Recognizing that $\Gamma(z^*) = [\Gamma(z)]^*$, (3.22) reduces to

$$\chi = 2\left[\arg\Gamma\left(\frac{1}{2}-i\eta\right)+\arg\Gamma(1+i\eta)\right]. \tag{3.23}$$

Finally, let us note that by rearranging the factors of η and β the term may be put in a form more tractable to calculation:

$$2\Delta L_{\text{Mott}} = \eta\beta^2\left\{\left[1.725+\left(0.52-2\sin^2\frac{\theta_0}{2}\right)\pi\cos\chi\right]\right.$$

$$+\eta\left(3.246-0.451\beta^2\right)$$
$$+\eta^2\left(0.987+1.552\beta^2\right)$$
$$+\eta^3\left[-2.696+\beta^2\left(4.569-0.494\beta^2\right)\right]$$
$$+\eta^4\left[-1.170+\beta^2\left(0.222+1.254\beta^2\right)\right]\Big\}. \tag{3.24}$$

It is recommended [41] that the Mott correction not be used for $Z_1/\beta > 100$, since the Mott correction becomes very large and negative at low energies, resulting in not only an incorrect but also an unphysical form for the stopping power.

3.2.6 The Relativistic Bloch Correction

It has been experimentally demonstrated that the Bloch correction is inadequate in regimes of both high charge and high energy [29]. An additional relativistic correction to the Bloch correction is necessary. This was first calculated by Ahlen [44]. Unfortunately, the original paper is not very accessible to the programmer who may wish to implement his formulae. Furthermore, it contains two free parameters which are not present in more sophisticated theories. Nevertheless, for historical reasons and comparisons with previous calculations, it is necessary to understand the form of this correction.

The overall form of what I will call the Ahlen correction is

$$\Delta L_{\text{Ahlen}} = \frac{\pi}{2}\beta^2\eta\frac{\pi\eta\exp(\pi\eta)}{\sinh\pi\eta}\left[(4\eta\ln 2)\,\text{Re}L_1+(\pi\eta-1)\,\text{Im}L_1+2\eta\text{Re}L_2\right], \tag{3.25}$$

where

$$\begin{aligned} L_1 &= -\theta_0\frac{\mathrm{i}}{1+\mathrm{i}2\eta}\left(\frac{\theta_0}{2}\right)^{\mathrm{i}2\eta}+\mathrm{i}\left(\frac{\alpha}{\beta\gamma\lambda}\right)^{1+\mathrm{i}2\eta}\frac{\exp(\mathrm{i}2\sigma)}{1+\mathrm{i}2\eta} \\ &= -\frac{\mathrm{i}}{1+\mathrm{i}2\eta}\left[2\left(\frac{\theta_0}{2}\right)^{1+\mathrm{i}2\eta}-\left(\frac{\alpha}{\beta\gamma\lambda}\right)^{1+\mathrm{i}2\eta}\exp(\mathrm{i}2\sigma)\right], \end{aligned} \tag{3.26}$$

and

$$\begin{aligned} L_2 &= -\theta_0 \frac{\mathrm{i}}{1+\mathrm{i}2\eta}\left(\frac{\theta_0}{2}\right)^{\mathrm{i}2\eta}\left(\ln\frac{\theta_0}{2}-\frac{1}{1+\mathrm{i}2\eta}\right) \\ &\quad -\mathrm{i}\left(\frac{\alpha}{\beta\gamma\lambda}\right)^{1+\mathrm{i}2\eta}\frac{\exp(\mathrm{i}2\sigma)}{1+\mathrm{i}2\eta}\left(\ln\frac{4\beta\gamma\lambda}{\alpha}+\gamma_{\mathrm{E}}-1+\frac{1}{1+\mathrm{i}2\eta}\right) \\ &= -\frac{\mathrm{i}}{1+\mathrm{i}2\eta}\left[2\left(\frac{\theta_0}{2}\right)^{1+\mathrm{i}2\eta}\left(\ln\frac{\theta_0}{2}-\frac{1}{1+\mathrm{i}2\eta}\right)\right. \\ &\quad \left.+\left(\frac{\alpha}{\beta\gamma\lambda}\right)^{1+\mathrm{i}2\eta}\exp(\mathrm{i}2\sigma)\left(\ln\frac{4\beta\gamma\lambda}{\alpha}+\gamma_{\mathrm{E}}-1+\frac{1}{1+\mathrm{i}2\eta}\right)\right]. \end{aligned} \tag{3.27}$$

In both expressions

$$\sigma = \arg\Gamma(1+\mathrm{i}\eta). \tag{3.28}$$

The two free parameters are θ_0 and λ. The first arises from considerations of Mott scattering, and can be thought of as an angular cutoff above which transverse momentum components may be neglected in the electron momentum. The parameter $\lambda = b_1/a_0$ represents the choice of close versus distant collision regimes, normalized to the Bohr radius. These parameters are not completely independent since it is assumed that $1/(k_0 b_1) \ll \theta_0 \ll 1$, where k_0 is the electron wave number in the center-of-mass frame of the problem. Ahlen [44] recommends $\theta_0 = 0.1$ and $\lambda = 1.0$. An energy-dependent form for θ_0 is given in [45]:

$$\theta_0 = \sqrt{\frac{\alpha}{\beta\gamma\lambda}}, \tag{3.29}$$

that is, the geometric mean between $\alpha/\beta\gamma\lambda$ and 1.

Extracting the real and imaginary parts of these expressions is laborious. To evaluate these terms, first we define

$$\phi_1 = 2\eta\ln\frac{\theta_0}{2}, \tag{3.30}$$

and

$$\phi_2 = 2\sigma + 2\eta\ln\frac{\alpha}{\beta\gamma\lambda}. \tag{3.31}$$

Then the desired real and imaginary parts can be expressed as

$$\mathrm{Re}L_1 = \frac{-\theta_0\,(2\eta\cos\phi_1 - \sin\phi_1) + \frac{\alpha}{\beta\gamma\lambda}\,(2\eta\cos\phi_2 - \sin\phi_2)}{1+4\eta^2}, \tag{3.32}$$

and

$$\mathrm{Im}L_1 = \frac{-\theta_0\,(2\eta\sin\phi_1 + \cos\phi_1) + \frac{\alpha}{\beta\gamma\lambda}\,(2\eta\sin\phi_2 + \cos\phi_2)}{1+4\eta^2}. \tag{3.33}$$

The third term, $\mathrm{Re}L_2$, is

$$\begin{aligned}\mathrm{Re}L_2 \;=\; & \left\{-\theta_0\left[\left(\ln\frac{\theta_0}{2} - \frac{1}{1+4\eta^2}\right)(2\eta\cos\phi_1 - \sin\phi_1) - \frac{2\eta}{1+4\eta^2}\,(2\eta\sin\phi_1 + \cos\phi_1)\right]\right. \\ & -\frac{\alpha}{\beta\gamma\lambda}\left[\left(\ln\frac{4\beta\gamma\lambda}{\alpha} + \gamma_{\mathrm{E}} - 1 + \frac{1}{1+4\eta^2}\right)(2\eta\cos\phi_2 - \sin\phi_2)\right. \\ & \left.\left.+\frac{2\eta}{1+4\eta^2}\,(2\eta\sin\phi_2 + \cos\phi_2)\right]\right\}\frac{1}{1+4\eta^2}.\end{aligned} \tag{3.34}$$

As one might imagine, there are numerous avenues for algebraic errors to enter here, especially during the process of translating these formulae into computer code. In fact, the coder may find it more worthwhile to implement complex arithmetic so that the complex expressions (3.26) and (3.27) may be written directly into the code. While this does not reduce the complexity of the calculation, it dramatically increases the readability, resulting in fewer errors.

The Bloch, Mott, and Ahlen corrections form what I will call hereinafter the BMA group, both because of their common thread of development and the necessity for all three to be included together for precise calculations.

3.2.7 The Lindhard-Sørensen Correction

What we will term the Lindhard-Sørensen [31] (LS) correction, ΔL_{LS}, *replaces* the Bloch correction [28], the Mott correction [41], and the Ahlen correction [44] (the BMA group). In their paper Lindhard and Sørensen show that the low-energy limit of the LS correction is *exactly* the

Bloch correction. Furthermore, by using exact solutions to the Dirac equation, the LS correction automatically incorporates Mott scattering and is relativistically correct. (This definition of the LS correction differs from that of [46], where the Bloch and Mott corrections are still considered as separate.) The LS correction is given by

$$\begin{aligned}\Delta L_{\mathrm{LS}} &= \sum_{k=-\infty\,(k\neq 0)}^{\infty}\left[\frac{|k|}{\eta^2}\frac{k-1}{2k-1}\sin^2\left(\delta_k-\delta_{k-1}\right)-\frac{1}{2|k|}\right] \\ &\quad+\frac{1}{\eta^2}\sum_{k=1}^{\infty}\left[\frac{k}{4k^2-1}\sin^2\left(\delta_k-\delta_{-k}\right)\right]+\frac{\beta^2}{2},\end{aligned} \tag{3.35}$$

where

$$\delta_k=\xi_k-\arg\Gamma\left(s_k+1+\mathrm{i}\eta\right)+\frac{\pi}{2}\left(l-s_k\right), \tag{3.36}$$

and with

$$\begin{aligned}s_k &= \sqrt{k^2-\left(\alpha Z_1\right)^2}, \\ \exp(\mathrm{i}2\xi_k) &= \frac{k-\mathrm{i}\eta/\gamma}{s_k-\mathrm{i}\eta}, \\ l &= \begin{cases} k & (k>0) \\ -k-1 & (k<0) \end{cases}.\end{aligned} \tag{3.37}$$

The quantity δ_k is a relativistic Coulomb phase shift and the summation over k is simply a summation over a parameterization of the angular momentum quantum numbers (including spin). It is possible to show that

$$\tan\left(\delta_k-\delta_{-k}\right)=-\frac{\eta}{\gamma k}, \tag{3.38}$$

so that the second term of (3.35) becomes

$$\sum_{k=1}^{\infty}\frac{k}{4k^2-1}\frac{1}{\gamma^2k^2+\eta^2}. \tag{3.39}$$

When we take the difference in phase shifts we find

$$\begin{aligned}\delta_k - \delta_{k-1} &= \frac{1}{2}\arctan\frac{\eta\,(s_{k-1}-s_k)}{s_k s_{k-1}+\eta^2} + \frac{1}{2}\arctan\frac{\eta/\gamma}{k(k-1)+(\eta/\gamma)^2} \\ &- \arg\Gamma\,(s_k+1+i\eta) + \arg\Gamma\,(s_{k-1}+1+i\eta) \\ &- \frac{\pi}{2}\left(s_k - s_{k-1} - \frac{k}{|k|}\right). \end{aligned} \tag{3.40}$$

For ease of computation, it is simple to combine the summation terms in (3.35) into a single sum over positive k. Accordingly, we have

$$\begin{aligned}\Delta L_{\rm LS} &= \sum_{k=1}^{\infty}\left[\frac{k}{\eta^2}\frac{k-1}{2k-1}\sin^2(\delta_k-\delta_{k-1}) + \frac{k}{\eta^2}\frac{k+1}{2k+1}\sin^2(\delta_{-k}-\delta_{-k-1})\right. \\ &+ \left.\frac{k}{4k^2-1}\frac{1}{\gamma^2k^2+\eta^2} - \frac{1}{k}\right] + \frac{\beta^2}{2}. \end{aligned} \tag{3.41}$$

In this form, $\Delta L_{\rm LS}$ converges roughly as k^{-3}. Note, however, that some special care is required for the $k=1$ term only. The phase shift δ_0 enters in the first summed term of (3.41) and because of the definition of s_k, it will be a complex number. Fortunately, the factor in front of $\sin^2(\delta_1-\delta_0)$ is zero. Thus, it is recommended that for $k=1$ only, the first term should be set to zero identically, rather than trying to force the computation of δ_0. A smoother evaluation of $\Delta L_{\rm LS}$ will also be obtained if the correction is evaluated up to a particular value of k, rather than up to some fractional precision.

3.2.8 The Finite Nuclear Size Correction

In their paper Lindhard and Sørensen [31] also derive a correction due to the finite size of atomic nuclei. This is possible because exact solutions to the Dirac equation exist for any spherically symmetric potential [47, 48]. We take the nuclear radius to be $R = 1.18A^{1/3}$ fm, and the dimensionless nuclear radius to be the ordinary radius divided by the electron Compton wavelength, $R' = Rm_{\rm e}c/\hbar = 0.003056A^{1/3}$. The effect of finite nuclear size appears as a modification to the

Coulomb phase shifts (3.36). In this way, we can continue to use the summation (3.35), but with new phase shifts given by

$$\begin{aligned}\delta_k &= \arg\left[\exp \mathrm{i}\delta_k^{\mathrm{r}} + H_k \exp \mathrm{i}\delta_k^{\mathrm{s}}\right] \\ &= \arctan \frac{\sin\delta_k^{\mathrm{r}} + H_k \sin\delta_k^{\mathrm{s}}}{\cos\delta_k^{\mathrm{r}} + H_k \cos\delta_k^{\mathrm{s}}},\end{aligned} \tag{3.42}$$

where δ_k^{r} is given by (3.36) and δ_k^{s} can be obtained from (3.36) by the replacement $s_k \to -s_k$ throughout (including ξ_k). Note, however, that we must sum (3.35) and not (3.41), since the relationship (3.38) no longer applies. The phase shift δ_k^{s} is the phase shift arising from the solution to the Dirac equation in the Coulomb potential which is singular at the origin. The real number H_k, which provides the connection between the interior uniform sphere potential and the exterior Coulomb potential, is very complicated to evaluate in comparison to δ_k^{r}. First, the main expression for H_k is

$$H_k = \frac{F^{\mathrm{r}}/G^{\mathrm{r}} - F^{\mathrm{i}}/G^{\mathrm{i}}}{F^{\mathrm{i}}/G^{\mathrm{i}} - F^{\mathrm{s}}/G^{\mathrm{s}}} \frac{G^{\mathrm{r}}}{G^{\mathrm{s}}}. \tag{3.43}$$

The four ratios—$F^{\mathrm{r}}/G^{\mathrm{r}}$, $F^{\mathrm{i}}/G^{\mathrm{i}}$, $F^{\mathrm{s}}/G^{\mathrm{s}}$, and $G^{\mathrm{r}}/G^{\mathrm{s}}$—are themselves complicated expressions which we define below. First I consider the ratio

$$\frac{F^{\mathrm{r}}}{G^{\mathrm{r}}} = \sqrt{\frac{\gamma-1}{\gamma+1}} \frac{\mathrm{Re}\Lambda^{\mathrm{r}}}{\mathrm{Im}\Lambda^{\mathrm{r}}}. \tag{3.44}$$

I define the quantity

$$\Lambda^{\mathrm{r}} \equiv \exp\left[\mathrm{i}\left(\xi_k^{\mathrm{r}} - \beta\gamma R'\right)\right] M\left(s_k + 1 + \mathrm{i}\eta, 2s_k + 1, \mathrm{i}2\beta\gamma R'\right), \tag{3.45}$$

where M is the confluent hypergeometric function (§A.4). In addition, the ratio $F^{\mathrm{s}}/G^{\mathrm{s}}$ may be obtained from Λ^{s} by the substitution $s_k \to -s_k$ throughout (3.45). The ratio $G^{\mathrm{r}}/G^{\mathrm{s}}$ is given by

$$\frac{G^{\mathrm{r}}}{G^{\mathrm{s}}} = \frac{|\Gamma(s_k + 1 + \mathrm{i}\eta)|}{|\Gamma(-s_k + 1 + \mathrm{i}\eta)|} \frac{\Gamma(-2s_k + 1)}{\Gamma(2s_k + 1)} \frac{\mathrm{Im}\Lambda^{\mathrm{r}}}{\mathrm{Im}\Lambda^{\mathrm{s}}} \left(2\beta\gamma R'\right)^{2s_k}. \tag{3.46}$$

The ratio $F^{\mathrm{i}}/G^{\mathrm{i}}$ depends sensitively on the sign of k. We define $\mathrm{sgn}k \equiv k/|k| = \pm 1$, so that

$$\frac{F^{\mathrm{i}}}{G^{\mathrm{i}}} = \left[\frac{\sum_{n=0}^{\infty} b_n}{\sum_{n=0}^{\infty} a_n}\right]^{-\mathrm{sgn}k}, \tag{3.47}$$

where the summands are given by the recursion relations

$$\begin{aligned}
b_0 &= 1 \\
a_0 &= \frac{2|k|+1}{R'(\gamma \mathrm{sgn}k + 1) + \mathrm{sgn}k\,(3\beta\eta/2)} b_0 \\
a_1 &= \frac{1}{2}\left[R'(-\gamma \mathrm{sgn}k + 1) - \mathrm{sgn}k\,(3\beta\eta/2)\right] b_0 \\
b_n &= \frac{\left[R'(\gamma \mathrm{sgn}k + 1) + \mathrm{sgn}k\,(3\beta\eta/2)\right] a_n - \mathrm{sgn}k\,(\beta\eta/2)\, a_{n-1}}{2|k|+2n+1} \\
a_{n+1} &= \frac{\left[R'(-\gamma \mathrm{sgn}k + 1) - \mathrm{sgn}k\,(3\beta\eta/2)\right] b_n + \mathrm{sgn}k\,(\beta\eta/2)\, b_{n-1}}{2(n+1)}.
\end{aligned} \tag{3.48}$$

The convergence of (3.35) including nuclear size effects has been demonstrated out to $\gamma_{\max} \simeq 10/R'$ [49]. Above this value of the Lorentz factor, evaluation of the confluent hypergeometric function can be problematic. However, even for uranium $\gamma_{\max} \simeq 528$; this is well into the ultrarelativistic limit, which is the topic of the next section.

3.2.9 The Ultrarelativistic Limit

Sørensen [50] has shown that for ultrarelativistic ions, a (careful) perturbation treatment of the problem of energy loss is possible. In particular, because of finite nuclear size effects, the potential energy experienced by an electron has a maximum depth of order $4Z_1 A_1^{-1/3} m_{\mathrm{e}} c^2 \approx 10$ MeV, while the kinetic energies involved are very much greater than this. Thus, the stopping power calculation should be amenable to perturbation methods.

For a uniformly charged nucleus, the perturbation treatment leads to a correction

$$\Delta L_{\mathrm{ultra}} = \frac{1}{2}\int_{-1}^{1} \frac{1-(1-\mu)\beta^2/2}{1-\mu}\left[\frac{9}{2(\beta\gamma R')^2}\frac{j_1^2\left(\sqrt{2}\sqrt{1-\mu}\beta\gamma R'\right)}{1-\mu} - 1\right] \mathrm{d}\mu. \tag{3.49}$$

The limiting behavior of this expression is given by

$$\Delta L_{\text{ultra}} = -\ln\left(\beta\gamma R'\right) - 0.2 + \beta^2/2. \tag{3.50}$$

The LS correction with the finite nuclear size modification tends toward this same limit. This correction cancels the density effect correction in the ultrarelativistic limit, so that the entire stopping logarithm becomes

$$L = L_0 + \Delta L = \ln\frac{2c}{R\omega_{\text{p}}} - 0.2, \tag{3.51}$$

where ω_{p} is the plasma frequency of the target material. The physical interpretation is that the impact parameters range from a minimum of R out to a maximum of c/ω_{p}. The remarkable simplicity of (3.50) allows us to "sweep under the rug" the misbehavior of the confluent hypergeometric function at high Lorentz factor.

The prediction of an energy-independent stopping power in the ultrarelativistic regime has been confirmed with $>$ 100 A GeV Pb ions at the CERN SPS accelerator [51, 52].

3.2.10 Other Ultrarelativistic Effects

Although the finite nuclear size effect is the most important modification to stopping power at very high energies, there are a few additional effects which can make a small but significant contribution to slowing.

Ahlen [28] discusses two of these effects and gives approximate formulae. First is a quantum electrodynamical (QED) effect, or radiative correction. The primary physical manifestation of this correction is bremsstrahlung of scattered electrons during electron-projectile collisions. In the derivation of Jankus [53], he gives the correction as an entirely separate form of energy loss. In SI

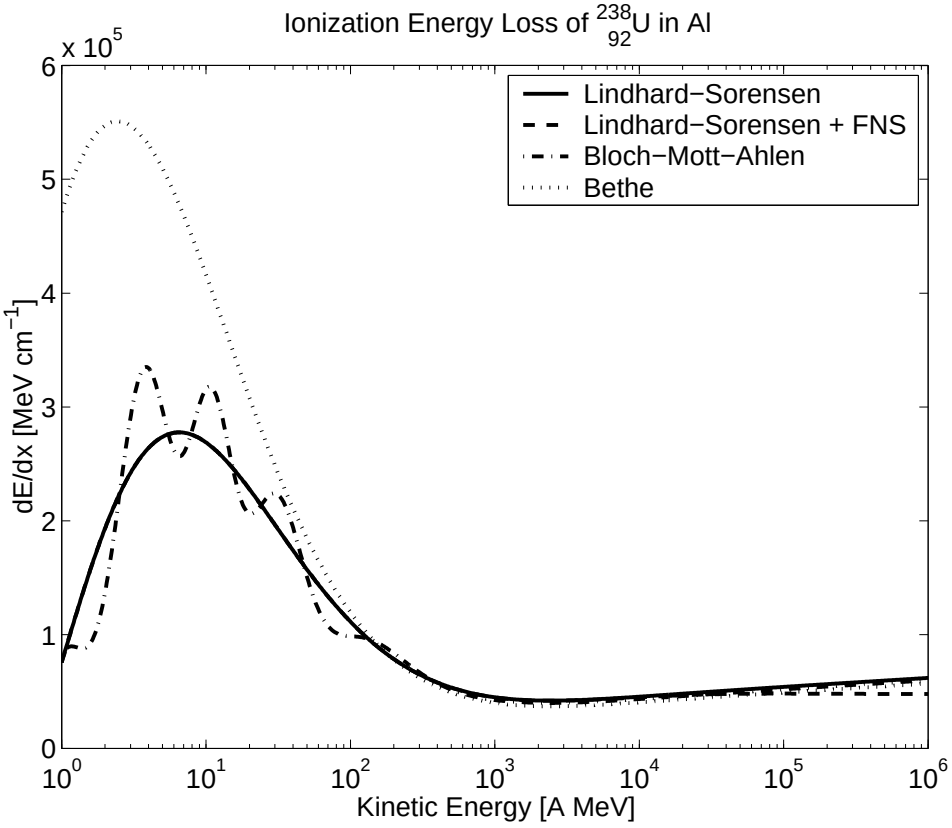

Figure 3.1: dE/dx as calculated with several important corrections for uranium slowing in aluminum. All computations included the Sternheimer, Berger, and Seltzer density effect and the Hubert, Bimbot, and Gauvin electron capture correction.

units, the energy loss is given by

$$-\frac{\mathrm{d}E_{\mathrm{QED}}}{\mathrm{d}x} = \frac{\alpha Z_1^2 e^4 n_{\mathrm{e}}}{4\pi^2 \varepsilon_0^2 m_{\mathrm{e}} c^2} L_{\mathrm{QED}}, \tag{3.52}$$

with the dimensionless factor L_{QED} given by

$$\begin{aligned} L_{\mathrm{QED}} &= \left\{ \frac{1}{3}[\ln(2\gamma)]^3 + \frac{29}{12}[\ln(2\gamma)]^2 - \left[\frac{217}{36} + \frac{\pi^2}{12}\right]\ln(2\gamma) \right. \\ &\quad \left. - \left[\frac{\pi^2}{3} - \frac{7}{4}\right]\ln q + \frac{899}{108} + \frac{\pi^2}{12} - \frac{39}{16}\zeta(3) - \frac{1}{4}\sum_{k=1}^{\infty}\frac{1}{2^k k^3} \right\}. \end{aligned} \tag{3.53}$$

The parameter q, which is a momentum integral cutoff in units of the electron mass, may take on the values $1 < q < 2\gamma$, but values of q in this range make rather small change in the value of (3.52). The sum in the last term has the value $\sum 1/2^k k^3 = 0.5372132\ldots$. Combining (3.52) with (3.1) we find

$$\Delta L_{\mathrm{QED}} = \frac{\alpha\beta^2}{\pi} L_{\mathrm{QED}}. \tag{3.54}$$

The other small ultrarelativistic effect is the kinematic correction. This accounts for the finite mass of the nucleus in electron-projectile collisions. We take the projectile mass to be $M_1 = A_1 m_{\mathrm{u}}$, where $m_{\mathrm{u}} = 931.4943\ \mathrm{MeV}/c^2$. This correction has the form

$$2\Delta L_{\mathrm{kin}} = -\ln\left(1 + 2\frac{\gamma m_{\mathrm{e}}}{A_1 m_{\mathrm{u}}}\right) - \frac{m_{\mathrm{e}}}{A_1 m_{\mathrm{u}}}\frac{\beta^2}{\gamma}. \tag{3.55}$$

Note the factor of 2 on the left-hand side. We can expect the finite-mass correction to become important when the energy of electrons in the rest frame of the projectile is comparable to the mass of the projectile. If we set $\gamma m_{\mathrm{e}} = A_1 m_{\mathrm{u}}$, then $\gamma = 1823 A_1$. This corresponds to approximately 400 A TeV for uranium! At so high an energy, other electromagnetic effects are much more important as we will see in §3.2.11. Furthermore, the kinematic effect may actually be damped by finite nuclear size effects. As pointed out by Lindhard and Sørensen [31], the momentum transfer in an electron-nucleus collision should have a maximum at roughly $\hbar/R$. Starting from the initial rest frame of the

nucleus, after the encounter, the recoil velocity of the nucleus will be of order $v_{\rm nuc}/c \simeq 0.18A^{-4/3}$. For uranium this is $v_{\rm nuc}/c \approx 10^{-4}$. Thus we can expect recoil effects to be entirely negligible for nuclei heavier than hydrogen.

3.2.11 Projectile Bremsstrahlung

There are a few ways in which a projectile can lose energy electromagnetically besides Coulomb collisions with electrons. The most important of these are projectile bremsstrahlung and pair production. Projectile bremsstrahlung is distinct from the QED electron bremsstrahlung correction. Here the bremsstrahlung is emitted directly from the projectile in the effective field of the target nuclei. Some of the details of the quantum theory of bremsstrahlung may be found in Heitler [54].

Following Heitler, then, the energy loss due to bremsstrahlung can be placed in the form (in units of A MeV g^{-1} cm^2)

$$\frac{{\rm d}E_{\rm rad}}{{\rm d}x} = \alpha N_{\rm A} m_{\rm u} c^2 r_{\rm e}^2 \left(\frac{m_{\rm e}}{m_{\rm u}}\right)^2 \frac{Z_1^4}{A_1^2}\frac{Z_2^2}{A_2}\gamma B, \tag{3.56}$$

where B is a dimensionless factor analogous to L. It is most interesting to note that unlike the Z_1^2/β^2 dependence in atomic collisions, bremsstrahlung scales as $Z_1^4\gamma$. Thus, although ion bremsstrahlung is depressed relative to electron bremsstrahlung by $(m_{\rm e}/m_{\rm u})^2$, bremsstrahlung can become important for very highly charged ions at energies which are not "too" ultrarelativistic (*i.e.*, energies accessible to present-generation heavy ion accelerators such as CERN-SPS and RHIC).

The explanation of the Z_1^4 dependence is very straightforward. Classically the power radiated by an accelerated particle with charge q is proportional to $q^2|\mathbf{a}|^2$. The acceleration is simply due to the Coulomb force, so $|\mathbf{a}|$ is proportional to q. Altogether then we have q^4. There is

an exact quantum mechanical correspondence. In terms of matrix elements, one must multiply the coupling of the ion to the electromagnetic radiation field ($\sim Z_1$) by the coupling of the ion to the Coulomb field of the target nucleus ($\sim Z_1 Z_2$). Then we square the matrix element to obtain rates and cross-sections, so altogether we have acquired $Z_1^4 Z_2^2$.

The dimensionless factor B is given by

$$B = \left[\frac{12\gamma^2+4}{3\beta\gamma^2} - \frac{6\beta+8}{3\beta^2\gamma^2}\ln(\gamma+\beta\gamma)\right]\ln(\gamma+\beta\gamma) - \frac{4}{3} + \frac{2}{\beta\gamma^2}F_{\rm b}\left(2\beta\gamma^2(1+\beta)\right), \tag{3.57}$$

where the "bremsstrahlung function," $F_{\rm b}$, is defined by

$$F_{\rm b}(x) = \int_0^x \frac{\ln(1+y)}{y}{\rm d}y. \tag{3.58}$$

This integral may be represented by the sum

$$F_{\rm b}(x) = -\sum_{n=1}^{\infty}\frac{(-x)^n}{n^2}, \tag{3.59}$$

for $x < 1$. For $x > 1$ the identity

$$F_{\rm b}(x) = \frac{\pi^2}{6} + \frac{1}{2}(\ln x)^2 - F_{\rm b}\left(\frac{1}{x}\right) \tag{3.60}$$

may be used.

There are a few corrections to this formula which Heitler discusses. The first is the correction due to bremsstrahlung off of atomic electrons. This may be included by making the replacement $Z_2^2 \to Z_2(Z_2+C)$ where $C \approx 0.75$. Another correction is due to the use of the first Born approximation in deriving (3.56). A correction of the form

$$\Delta B_{\rm Born} = -4.828(\alpha Z_2)^2 \tag{3.61}$$

accounts for the inadequacy of the first Born approximation for large Z_2. We may also expect further substantial corrections due to finite nuclear size effects, but this takes us beyond the scope of the present work.

Pair production, sometimes called "sparking the vacuum" is basically a small correction to projectile bremsstrahlung. Ahlen [28] gives the ratio of pair-production loss to bremsstrahlung loss:

$$\frac{\mathrm{d}E_{\mathrm{pair}}/\mathrm{d}x}{\mathrm{d}E_{\mathrm{rad}}/\mathrm{d}x} \simeq \frac{A_1}{1000Z_1^2}\frac{m_{\mathrm{u}}}{m_{\mathrm{e}}}, \tag{3.62}$$

for ultrarelativistic nuclei.

3.2.12 Electron Capture

With the possible exception of certain low-energy corrections, the influence of electron capture may be the least well understood correction to stopping power. It may not be possible to formulate the influence of electron capture as an additive correction. Intuitively, however, we can imagine that electron capture may be made manifest as a correction to the projectile charge. Indeed, this is typically how the correction is made. We take the bare charge of the projectile to be Z_0. Then, everywhere it appears, we take Z_1 to be the *effective* charge of the projectile. For energies significantly in excess of 1 A GeV, the effective charge will be very nearly equal to the bare charge. For lower energies, the empirical formula of Pierce and Blann [55] is available:

$$Z_1 = Z_0\left[1-\exp\left(-\frac{130\beta}{Z_0^{2/3}}\right)\right]. \tag{3.63}$$

The power $Z_0^{2/3}$ in the exponential is derived from Thomas-Fermi calculations on the target atoms [56, 57]; however, other parameters in the formula are shown experimentally to depend on the target material [58]. Using the parameterization of [58],

$$Z_1 = Z_0\left[1-A(Z_2)\exp\left(-\frac{B(Z_2)\beta}{\alpha Z_0^{2/3}}\right)\right], \tag{3.64}$$

with the empirically determined functions A and B given by

$$A \;=\; 1.16 - 1.91\times10^{-3}Z_2 + 1.26\times10^{-5}Z_2^2$$

Target	D	B	C	x_2	x_3	x_4
Be	2.045	2.000	0.04369	7.000	0.2643	0.4171
C	2.584	1.910	0.03958	6.933	0.2433	0.3969

Table 3.1: Effective charge parameters for the Hubert, Bimbot, and Gauvin formula for beryllium and carbon.

$$B = 1.18 - 7.5 \times 10^{-3} Z_2 + 4.53 \times 10^{-5} Z_2^2. \tag{3.65}$$

Even more recently, using a fit to a large dataset of stopping power and range data, Hubert, Bimbot, and Gauvin [59, 60] have produced the formula

$$Z_1 = Z_0 \left[1 - x_1 \exp\left(-x_2 E^{x_3} Z_0^{-x_4}\right)\right], \tag{3.66}$$

where E is the kinetic energy in A MeV, and the x parameters are given as follows:

$$\begin{aligned}
x_1 &= D + B\exp(-CZ_0) \\
D &= 1.164 + 0.2319\exp(-0.004302Z_2) \\
B &= 1.658 \\
C &= 0.05170 \\
x_2 &= 8.144 + 0.09876\ln Z_2 \\
x_3 &= 0.3140 + 0.01072\ln Z_2 \\
x_4 &= 0.5218 + 0.02521\ln Z_2,
\end{aligned}$$

where these parameters should be considered valid for all targets except beryllium and carbon which are given in Table 3.1. A comparison of the effective charge in all three models described here is given in Figure 3.2.

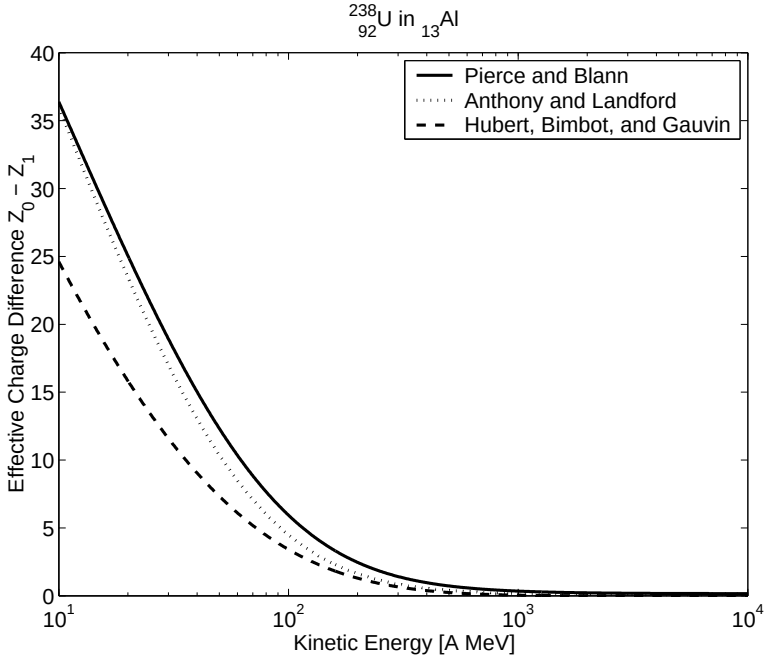

Figure 3.2: Effective charge difference of uranium in aluminum as a function of energy for the different electron capture models described in this work.

3.2.13 The Barkas Correction

As we have seen, the stopping logarithm becomes remarkably simple at very high energies. Our intuition might now suggest that it becomes remarkably more complicated as we approach lower energies. Indeed, this seems to be the case.

The Barkas effect was first noticed as a difference in stopping power between positive and negative pions [61, 62], indicating that the stopping power contained odd powers of Z_1. The independent analyses of Ashley, Ritchie, and Brandt [63, 64, 65] and Jackson and McCarthy [66] concluded that target polarization effects for low-energy distant collisions would produce a multiplicative correction to the stopping power, that is

$$\frac{\mathrm{d}E}{\mathrm{d}x} \rightarrow \frac{\mathrm{d}E_{\mathrm{Barkas}}}{\mathrm{d}x} = \frac{\mathrm{d}E}{\mathrm{d}x}\left(1 + \frac{Z_1}{\sqrt{Z_2}}F(V)\right). \tag{3.67}$$

V	$V^2F(V)$	$F(V)$
1.0	0.33	0.33
2.0	0.31	0.078
3.0	0.27	0.03
4.0	0.23	0.014
5.0	0.21	0.0084
6.0	0.19	0.0053
7.0	0.17	0.0035
8.0	0.16	0.0025
9.0	0.15	0.0019
10.0	0.14	0.0014

Table 3.2: Values of the Jackson-McCarthy "universal" function.

The variable V is a reduced momentum defined by

$$V = \frac{\beta\gamma}{\alpha\sqrt{Z_2}}. \tag{3.68}$$

The "universal" function $F(V)$ is a ratio of two integrals over a Thomas-Fermi model of the atom. A figure showing values of $V^2F(V)$ is given in [66]. Also, values of $V^2F(V)$ may be found in Table 3.2. Jackson and McCarthy do not consider their calculations to be reliable for $V < 0.8$. Interestingly, their calculation also found the close-collision correction to be nearly the same as the first term of the Mott correction (the term proportional to $\eta\beta^2$).

The Barkas effect was actually given its name several years after the Jackson and McCarthy article by Lindhard, who showed [67] that the correction factor should be multiplied by two (*i.e.* $F(V) \rightarrow 2F(V)$) to give better agreement with both theoretical results and experimental data. Basically, Jackson and McCarthy should have included close collisions even in the low-energy regime. This was confirmed with a more detailed calculation by Morgan and Sung [68].

Because of the way the Barkas correction is formulated, it has been questioned [69] whether the effect can be deconvolved from the effects of electron capture (*i.e.*, the effective charge

Z_1).

3.2.14 The Shell Corrections

Shell corrections arise when the velocity of the projectile is comparable to velocities of electrons in target atoms. Two regimes are possible: first, the velocity of the projectile may be low enough so that inner (K, L) shell electrons have velocities comparable to the projectile; second, the inner shell electrons may actually have relativistic velocities for sufficiently heavy target atoms.

For the first type of shell correction, Fano [70] proposed a correction of the form

$$\Delta L_{\text{shell}} = -C/Z_2, \tag{3.69}$$

where C is a complicated function of the various parameters. Fano also showed that ΔL_{shell} does not vanish at high energies, as was assumed when shell corrections were first discussed. This fact led to widespread use of the "adjusted" shell correction, which is defined by

$$\ln I + C/Z_2 \equiv \ln I_{\text{adj}} + C_{\text{adj}}/Z_2, \tag{3.70}$$

demanding $\lim_{\beta\to 1} C_{\text{adj}}/Z_2 = 0$. Theoretical calculations of C exist [70, 71, 72], as well as some experimental values [73]. However, as nearly as can be determined, these values only apply to protons and other singly charged particles. Since most other correction terms we have investigated scale as a positive power of Z_1, it is probably reasonable to assume that the shell correction is not as important as other low-energy corrections, especially the Barkas term. The version of Barkas and Berger [71] is fairly widely accepted:

$$\begin{aligned} C_{\text{adj}} &= \left(4.22377\times 10^{-7}\beta^{-2}\gamma^{-2} + 3.04043\times 10^{-9}\beta^{-4}\gamma^{-4} - 3.8106\times 10^{-10}\beta^{-6}\gamma^{-6}\right) I_{\text{adj}}^2 \\ &\quad + \left(3.858019\times 10^{-9}\beta^{-2}\gamma^{-2} - 1.667989\times 10^{-10}\beta^{-4}\gamma^{-4}\right. \end{aligned}$$

$$+ 1.57955 \times 10^{-12} \beta^{-6} \gamma^{-6} \big) I_{\mathrm{adj}}^3, \tag{3.71}$$

where the formula should be considered valid for $\beta\gamma > 0.13$.

The second situation mentioned above was addressed by Leung [74, 75] who found an additional relativistic shell correction:

$$\Delta L_{\mathrm{Leung}} = -\frac{5}{3} \ln \left(\frac{2 m_{\mathrm{e}} c^2 \beta^2}{I} \right) \frac{|B_{\mathrm{tot}}|}{Z_2 m_{\mathrm{e}} c^2} + \frac{I^2}{4 m_{\mathrm{e}}^2 c^4 \beta^2}, \tag{3.72}$$

where $B_{\mathrm{tot}} < 0$ is the total ground-state electronic binding energy. Again, it is not clear how this result scales with projectile charge. In addition I have omitted a term $-\beta^2$ which appears in the correction as defined in [75], since this is probably part of the Bethe form (the derivation is not highly relativistic in the projectile velocity).

3.3 Comparisons with Experiment

Uranium beam-time is very precious and so we have sought to compare the results of stopping power calculations to experiments already performed. Perhaps the most interesting is the experiment of Ahlen and Tarlé [29]. Regrettably, the LBNL Bevalac no longer operates, but in the Ahlen and Tarlé experiment, a beam of uranium from the Bevalac was brought to rest after passing through a series of targets (listed in Table 3.3). The beam energy was determined to be 955.7 ± 2.0 A MeV (by means other than range-energy). This is very close to the uranium beam energy currently offered by the GSI accelerator, so this is a repeatable experiment.

The primary interest of Ahlen and Tarlé was the importance of the BMA group of corrections to $\mathrm{d}E/\mathrm{d}x$, so several steps were taken to reduce the importance of additional low-energy corrections. The mean ionization potential I for each target was taken to have its adjusted value I_{adj}

Target	Thickness [g cm^{-2}]	I_{adj} [eV]
Al (beam window)	0.137 ± 0.020	166 ± 1
Air	0.0426 ± 0.0020	85.4 ± 1.0
Cu	8.3162 ± 0.0010	323 ± 2
Lexan	2.327 ± 0.002	67.0 ± 1.0

Table 3.3: Experimental setup in the Ahlen and Tarlé experiment.

(listed in Table 3.3) as the high-energy limit of the shell correction. The effective projectile charge due to electron capture was computed from the Pierce and Blann formula [55]. Finally, all (very uncertain) low-energy corrections were effectively circumvented by using a measured range [76] below 150 A MeV. That is, integrations of $\mathrm{d}E/\mathrm{d}x$ were carried out only between 150 A MeV and 1000 A MeV. Ignoring all corrections in the BMA group, they found a reconstructed beam energy of 903.5 A MeV. Including only the Mott correction the beam energy became 1003.9 A MeV. Clearly, Mott corrections alone are not sufficient for the stopping power of uranium. Finally, they calculated the beam energy including all components of the BMA group with a resulting theoretical energy of 952.8 A MeV, a fractional error of only 0.3%. Although the theoretical uncertainty was not quoted, the uncertainty due to electron capture alone encompasses the measured energy value as they show in their Figure 2.

As a first test of our own range-energy calculations we sought to reproduce the calculations of Ahlen and Tarlé so that we would have a solid basis against which we could compare other sorts of range-energy calculations. The primary complication is not in the theoretical construction of range-energy code, but in the empirical range used below 150 A MeV. For this we must look to the results of Ahlen, Tarlé, and Price [76]. This experiment was also performed at the Bevalac with a beam of 147.7 A MeV uranium. The experimental setup is summarized in Table 3.4. The

Target	Thickness [g cm^{-2}]
Al (beam window) + Air	0.2039 ± 0.014
CR-39	0.3771 ± 0.0005
Total Range	0.581 ± 0.014

Table 3.4: Experimental setup in the Ahlen, Tarlé, and Price experiment.

individual thicknesses of Al beam-pipe window and air were not quoted in the article. Note that the range was measured not in Lexan but in CR-39, a somewhat different plastic track-etch detector.

The details of how the conversion of CR-39 range to Lexan range was performed are hazy at best [77]. There are a variety of ways to perform the range conversion, ranging from overly simplistic to sophisticated. For each technique considered, we computed the beam energy using corrections due to the BMA group or its replacement, the LS correction. The resulting beam energies agreed with the original calculation typically to better than a few tens of A MeV. Furthermore, for each technique the BMA calculation and the LS calculation agreed to typically better than 1 A MeV. Thus, we feel it is quite valid to replace the BMA group with the LS correction.

Because of the uncertainty of the aforementioned range conversion, we also considered the direct integration of $\mathrm{d}E/\mathrm{d}x$. As there is no suggestion of how shell corrections scale with projectile charge, we ignored these entirely. More significant, however, is the Barkas correction which was included for some calculations. The integration was carried out using code based on the work of Salamon [78]. One interesting aspect of this code is the use of semi-empirical ranges based on the work of Barkas and Berger [27] for very low energies (< 8 A MeV). Results are summarized in Table 3.5. The "Bethe" method uses the bare Bethe formula plus the density effect correction. "BMA" is "Bethe" plus the BMA group. "LS" is "Bethe" plus the LS correction (finite nuclear size effects are negligible at this energy and were not included). Each method was performed with and

Method	Energy [A MeV]
(no Barkas)	
Bethe	899.4
BMA	931.9
LS	947.3
(with Barkas)	
Bethe	908.5
BMA	948.6
LS	957.0
Beam Energy	955.7 ± 2.0

Table 3.5: Beam energy reconstructions by the method of direct integration. (Data originally presented at 26th ICRC Salt Lake City.)

Target	Substance	Thickness [mg cm^{-2}]	I [eV]
Beam Window	Hostaphan ($C_{10}H_{10}O_4$)	22.8	72.3
	Kevlar ($C_{14}H_{14}N_2O_2$)	12.1	71.7
Air	Air	7.23	85.4
Wire Chamber	Kapton ($C_{22}H_{10}N_2O_5$)	3.55	75.9
	"Mesh"	5.16	223.0
	Ar (80%) CO_2 (20%)	19.0	174.7
	Kapton ($C_{22}H_{10}N_2O_5$)	3.55	75.9
Air	Air	32.5	85.4
Copper Absorber	Cu	8669.7 ± 4.5	323.0
Lexan Target	Lexan ($C_{16}H_{14}O_3$)	2725 ± 32	73.1

Table 3.6: Experimental setup in the 1999 GSI Exposure.

without the Barkas correction.

In 1999 we had the opportunity to repeat Ahlen and Tarlé's experiment. We made use of the 1.0 A GeV uranium beam at the GSI laboratory in Darmstadt, Germany. Table 3.6 shows the experimental setup in the 1999 GSI exposure. The details of the beam window and wire chamber are from Schardt [79]. In addition, the beam energy was 1000.0 ± 0.5 A MeV with a spread of 0.15% about this central value.

The Lexan target consisted of 103 sheets of Lexan plastic, each about 260 μm in thickness.

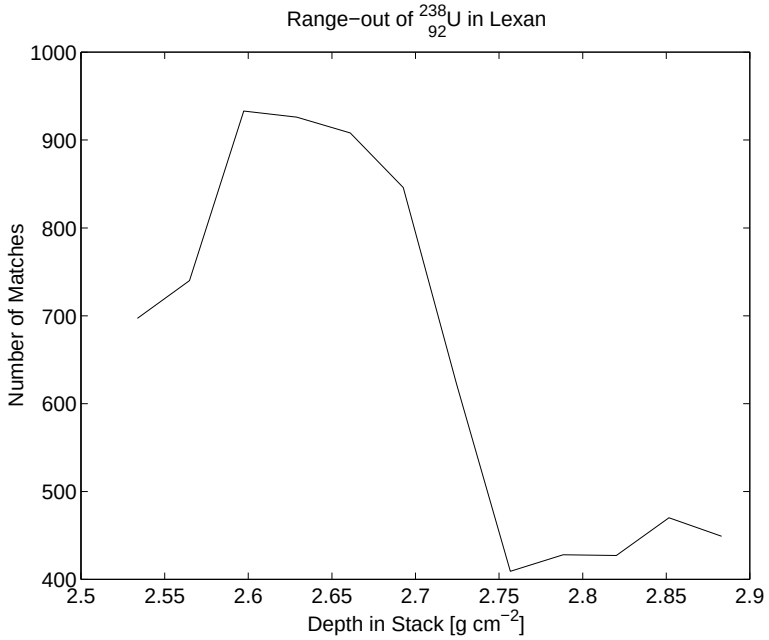

Figure 3.3: Number of matched events in adjacent sheets of Lexan as a function of depth in the Lexan stack.

The range in Lexan was determined by scanning the sheets near the stopping-point of the main beam, determined by visual comparison of track density on upstream and downstream sheets. The positions of events found in the scans were matched on adjacent sheets. The number of matches found as a function of depth in the Lexan stack is shown in Figure 3.3. Clearly, a steep decline in the number of matches begins at around 2.7 g cm^{-2} and continues to about 2.75 g cm^{-2}. The midpoint of this decline was taken to be the stopping point for the purpose of calculating energy, with the uncertainty determined by the thickness of one Lexan sheet to either side of the stopping point.

The results of the energy reconstruction are shown in Table 3.7. The various effects included in the reconstruction are also shown. In both cases, the range was integrated up from 8 A MeV, with the energy at 8 A MeV given by the Benton and Henke [24] range code.

Effects Included	Energy [A MeV]
Lindhard-Sørensen	
Electron Capture*	
Density Effect‡	1009.0 ± 2.7
Lindhard-Sørensen	
Electron Capture†	
Density Effect‡	
Shell Effect¶	
Leung Effect	1002.2 ± 2.7
Beam Energy	1000.0 ± 0.5

*Version of Hubert, Bimbot, and Gauvin [59, 60]
†Version of Anthony and Landford [58]
‡Version of Sternheimer, Berger, and Seltzer [36]
¶Version of Barkas and Berger [27]

Table 3.7: Results of energy reconstruction from range in the 1999 GSI exposure.

3.4 Comparisons with Theory

To test the general accuracy of the code developed as part of this study, I compared range and energy loss to the code developed by Benton and Henke [24] (hereinafter BH) and to the tables of Hubert, Bimbot, and Gauvin [60] (hereinafter HBG). The HBG tables cover the energy regime 2.5 to 500 A MeV, so the comparison was performed only in this region. Both the BH and HBG ranges are based on experimental measurements. In the case of BH, the code is based on parametric fits to the range tables of Barkas and Berger [27]. HBG extrapolated their tables from a large experimental data set. The comparison was performed using the Lindhard-Sørensen correction (without finite nuclear size which is negligible at these energies), the density effect of Sternheimer, Berger, and Seltzer [36], and HBG's own version of electron capture.

Figure 3.4 shows the comparison among all three sources. This log-log plot is only intended to show the overall shape of the curves in this energy region. Figure 3.5 shows the fractional

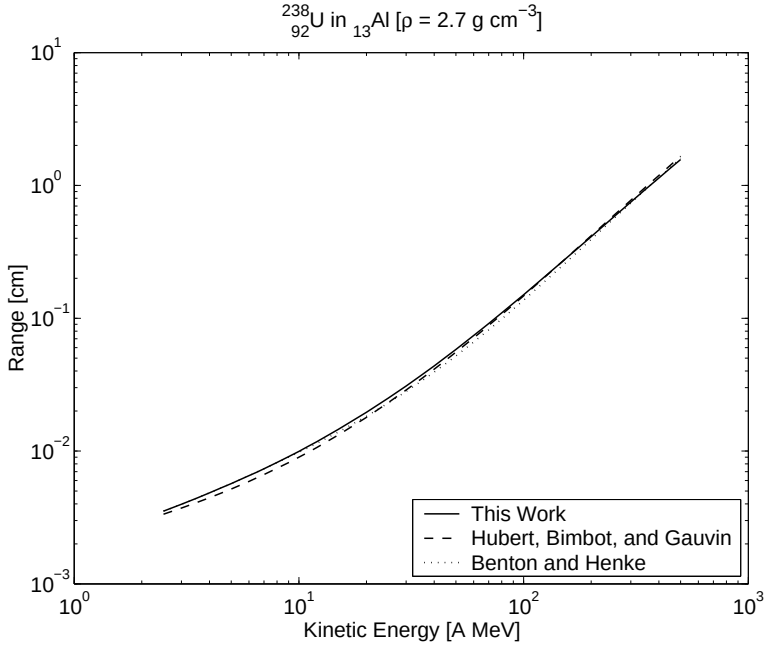

Figure 3.4: Comparison of ranges of uranium in aluminum from three different sources.

differences $(R-R_{\mathrm{BH}})/R_{\mathrm{BH}}$ and $(R-R_{\mathrm{HBG}})/R_{\mathrm{HBG}}$. Since the code developed in this work is based on the BH ranges below 8 A MeV, that fractional difference is extremely small at low energies. Figure 3.6 shows a comparison of $\mathrm{d}E/\mathrm{d}x$ computed from the three sources. The BH code contains three different parameterizations covering different energy regions. The dip in the BH value of $\mathrm{d}E/\mathrm{d}x$ at about 7 A MeV is due to a slight imperfection in the joining of two parameterization regions. The join between the different parameterization regions is optimized for continuity in range and $\mathrm{d}E/\mathrm{d}x$ only, so it is not surprising to see a discontinuity in the value of $\mathrm{d}^2E/\mathrm{d}x^2$.

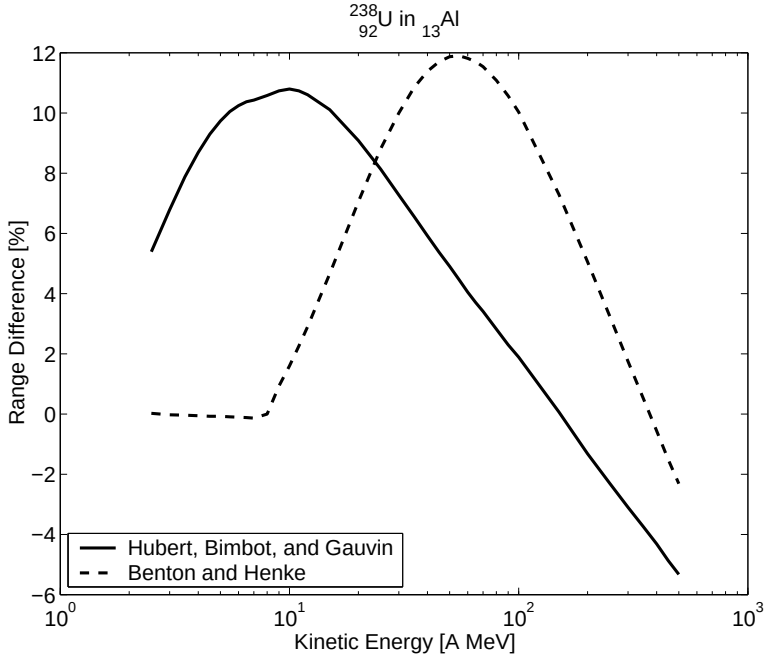

Figure 3.5: Fractional differences (in percent) for the range code developed in this work compared to two other sources.

3.5 Conclusion

The code developed as part of this study is certainly accurate enough for applications in cosmic-ray astrophysics and most other purposes. It is accurate to $\sim 0.2\%$ in the reconstruction of energy as a function of range in actual experiments and agrees to better than 10% with existing codes and tables in the theoretically troublesome low-energy region. Figure 3.6 is especially revealing when compared to Figure 3.1. Without the Lindhard-Sørensen correction (which reduces to the Bloch correction in the energy region of Figure 3.6) there would be a disagreement of roughly a factor of 2 between the code developed in this work and older codes and tabulations. With the exception of electron capture, the Lindhard-Sørensen correction completely dominates all low-energy effects. This is to be expected, since the Bloch correction scales as Z_1^2, the Barkas effect scales as Z_1,

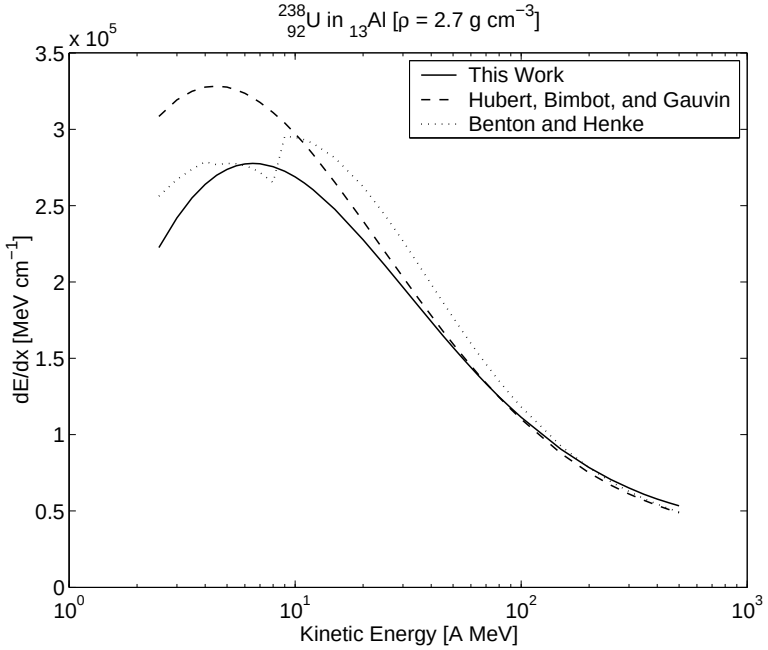

Figure 3.6: Comparison of energy loss of uranium in aluminum from three different sources.

and the shell and Leung corrections, which are primarily concerned with the velocity of inner-shell electrons of the target atoms, should not be expected to scale with Z_1 at all.

The code developed during this study can be found at

`http://ultraman.ssl.berkeley.edu/~weaver/dedx/`,

and will be maintained and updated for some time.

Chapter 4

The Response of BP-1 to Relativistic Heavy Ions

> See the constellation ride across the sky
> No cigar, no lady on his arm
> Just a guy made of dots and lines
> — "See the Constellation," *Apollo 18* (1992)

4.1 Introduction

In the study of track-etch detectors, the fundamental observables are the track geometry (the characteristics of the elliptical etch-pit mouth and, alternatively, the depth of the etch-pit), and the "general" or "bulk" etch rate v_G (determined by measuring G, the thickness of material removed from one surface during etching and dividing by the etch time). The particle track is etched at the track-etch rate v_T. The etch-pit characteristics depend on the ratio $s \equiv v_T/v_G$, which we will typically call the detector "signal" or "response." Since it is very difficult to measure a track-etch rate *in situ*, this ratio is necessarily determined purely from the geometry of the etch-pit. The

conversion from etch-pit geometry to response is fully described in Appendix B.

Since s can vary by orders of magnitude, depending on particle charge and energy, it is often more convenient to deal with the quantity $\ln s$. In addition the quantity

$$\xi \equiv \ln(s-1) \tag{4.1}$$

has been used in the past. Throughout this work I will refer to the empirically determined function $s = f(Z,\beta)$ (sometimes expressed in terms of $\ln s$ or $\ln(s-1)$) as the "response function."

For track-etch detectors to be useful as cosmic-ray detectors, we must have some knowledge of the detector response as a function of charge and energy. As we shall see, this function is not, in general, a simple function of a property such as total energy loss, or restricted energy loss. However, we have good evidence that response is a simple function of Z/β at low energies.

4.2 Response of BP-1 in HF

We exposed BP-1 detectors at the Alternating Gradient Synchrotron (AGS) to Au beams at three energies. All detectors were first exposed to 10.8 A GeV Au at two zenith angles. Later, one stack of detectors was exposed to 4 A GeV Au with additional slowing provided by a thick Pb target, while the other stack was exposed similarly to 2 A GeV Au. The exact beam energies at extraction were as follows [80]: 10.80 ± 0.03 A GeV (beam momentum, 11.69 ± 0.03 A GeV/c), 4.04 ± 0.01 A GeV, and 2.003 ± 0.002 A GeV. The lower energy exposures were performed at an azimuth angle of 90° relative to the 10.8 A GeV beam to allow for easy identification of the two exposures. The detectors were etched in HF to $G \approx 50\mu$m.

In order to determine the response as a function of both charge and energy, we needed accurate estimates of the energy of each beam. First of all, we used up-to-date range-energy calcu-

lations to determine the energy of the primary low-energy beams after passing through the Pb target as well as through the air between the beam-pipe and the target.

In general, the fragments of Au will have a different energy at the detector, due simply to the fact that their charges and masses are different. In particular the masses of nuclear fragments of Au can be estimated using the cross-section codes of Silberberg and Tsao [81, 82, 83, 84, 85, 86, 87] (version 10 Jan 2000, `http://spdsch.phys.lsu.edu`). In principle it is possible to find the average masses as a function of energy in the detector. However, this is computationally intensive, so for the purposes of estimation, we computed the average masses for a beam energy of 1000 A MeV and a propagation distance of 1 cm in BP-1. Further details are given in Appendix C. The average masses of fragments generally fall significantly on the proton-rich side of the valley of stability. While we can account for the change in mass and charge, we cannot know at what point along the path the nuclear fragmentation took place. Therefore we computed the energies for two extreme limits: one in which all fragmentation took place as the beam was emerging from the beam pipe, the other in which all fragmentation took place at the top of the detector sheet in consideration (*e.g.*, after passing through the Pb target and any upstream detector sheets). The final energy assigned to a group of fragments was the average of these two energies.

The response data were combined into a single dataset so that the charge and energy dependence could be fitted simultaneously, rather than separately as had been done in the past. Figure 4.1 and Figure 4.2 show the raw data considered for this fit. Due to the difficulty in fitting the relativistic rise (§4.3), the 160 A GeV data shown in these figures were not included in the fit.

Figure 4.3 shows signal versus $\mathrm{d}E/\mathrm{d}x$. It should be clear from this plot that detector signal is not a simple function of total energy loss. A quantity related to $\mathrm{d}E/\mathrm{d}x$ is the restricted energy loss

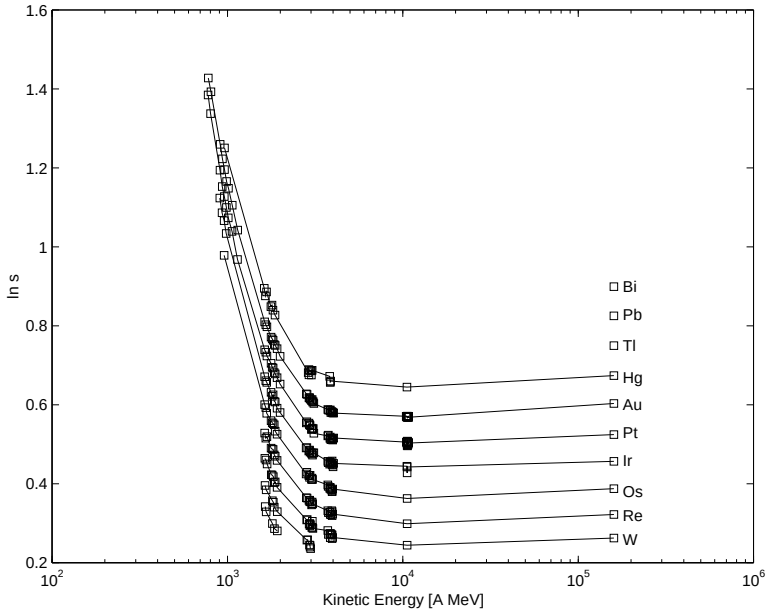

Figure 4.1: Detector response in terms of ln$s$ plotted versus projectile kinetic energy. Statistical error bars have been suppressed since they are smaller than the symbols for nearly every point. Labels are shown for a selected population of charges. Lines connect points with the same charge.

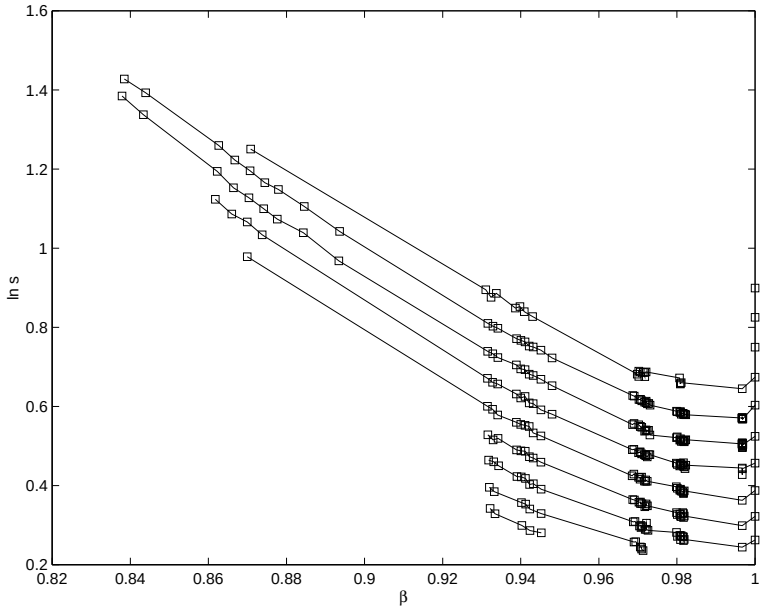

Figure 4.2: Detector response in terms of ln$s$ plotted versus velocity in units of the speed of light.

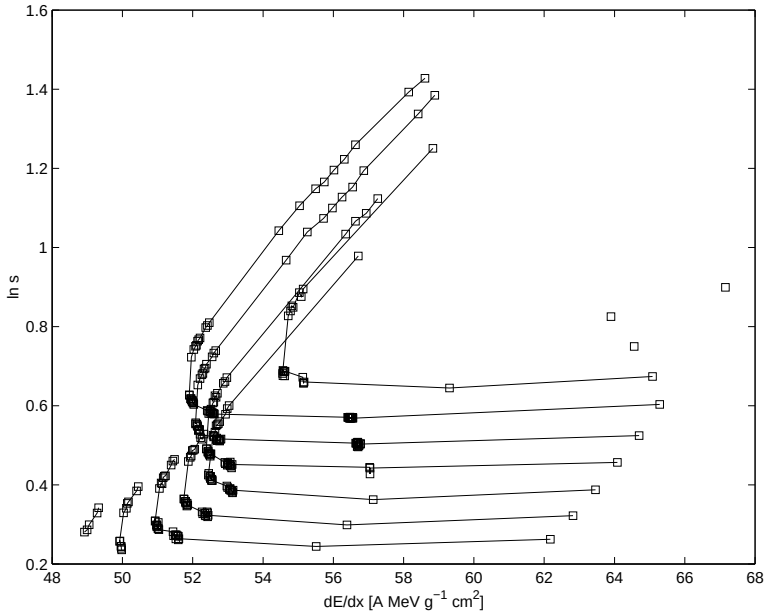

Figure 4.3: Detector response in terms of $\ln s$ plotted versus $\mathrm{d}E/\mathrm{d}x$.

(REL) [88], defined as the amount of energy lost per unit length which goes into free electrons with energy less than some given energy (350 eV in Figure 4.4). Presumably these low-energy electrons would deposit most of their energy close to the particle track. Figure 4.5 shows the signal versus Z/β, a traditional parameter in estimating detector response. It is quite interesting to compare this figure to Figure 19 of [28].

As Figure 4.5 shows, the response seems to approach a very simple function of Z/β at low energies. Also, as can be seen in Figure 4.1, there is essentially no relativistic rise between 4 and 10 A GeV. These two facts severely constrain the form of the response function. The form we considered is given by

$$\ln s = a_1 \frac{Z}{\beta^{a_2}} + a_3 \beta^{a_4} + a_5. \tag{4.2}$$

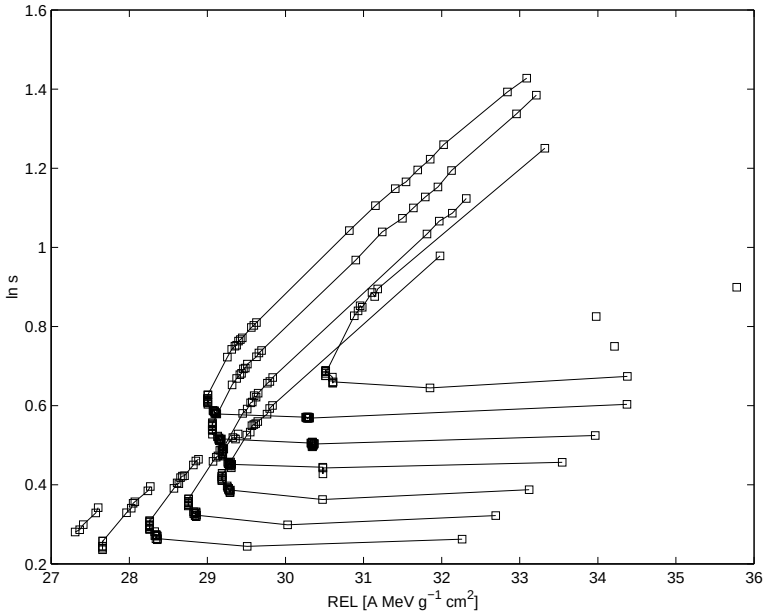

Figure 4.4: Detector response in terms of ln$s$ plotted versus restricted energy loss (REL).

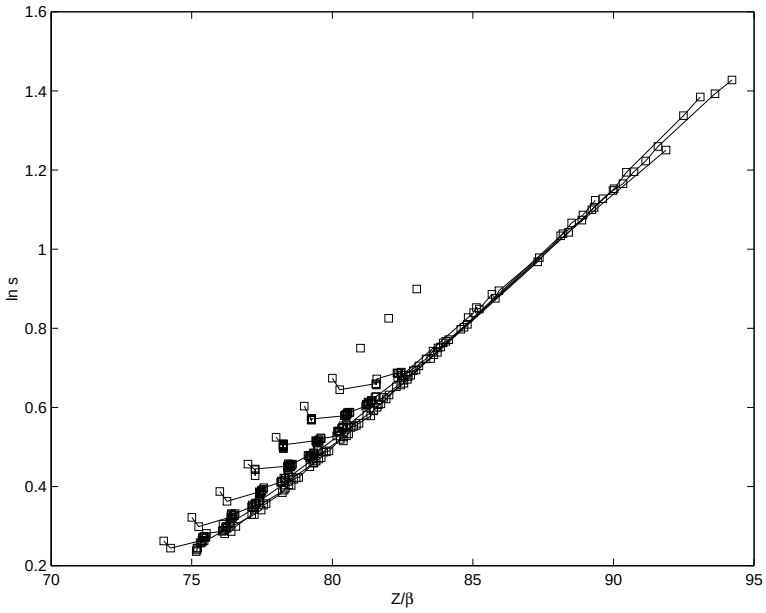

Figure 4.5: Detector response in terms of ln$s$ plotted versus Z/β.

The parameters are

$$\begin{aligned} a_1 &= 0.063887 \\ a_2 &= 1.023121 \\ a_3 &= 0.145173 \\ a_4 &= 51.862026 \\ a_5 &= -4.617155. \end{aligned} \tag{4.3}$$

There are several things worth noting here. First, $\ln s$ is strictly linear in Z in this model. Second, since $a_2 \approx 1$, $\ln s$ is very close to being strictly linear in Z/β, at least at low energies. Third, the threshold behavior is at least qualitatively reproduced by the form of this function—that is, arbitrarily small charges cannot produce arbitrarily small responses. Below $Z \approx 70.1$ at high energy, $\ln s < 0$, which indicates $s < 1$ and no track is formed. The strict linearity of $\ln s$ in Z may break down close to threshold, so the actual cut-off charge may be a few charges lower than this. Fourth, as mentioned above, the high power of β, that is a_4, is required by the absence of any significant change in the response between 4 A GeV and 10 A GeV.

The response function published in [23] is actually a rather poor fit to the data. For the sake of comparison, I reproduce it here:

$$\ln(s-1) = c_1 \ln Z + c_2 (\ln Z)^2 + c_3 \ln\beta + c_4 \beta^{1/c_5} + c_6, \tag{4.4}$$

with parameters

$$\begin{aligned} c_1 &= 240.8877 \\ c_2 &= -26.2148 \end{aligned}$$

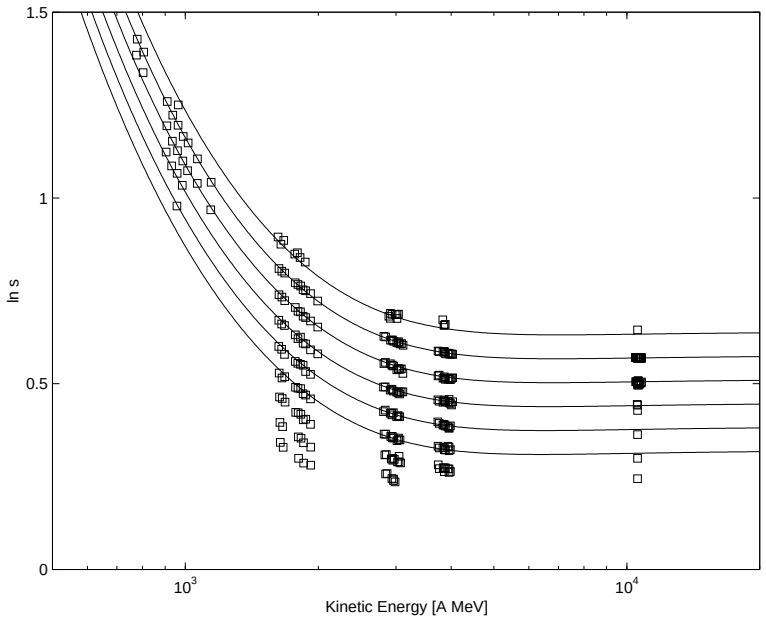

Figure 4.6: Detector response in terms of $\ln s$ plotted versus kinetic energy. Lines indicate the fitted response function for Hg, Au, Pt, Ir, Os, and Re.

$$\begin{aligned} c_3 &= -10.2718 \\ c_4 &= 0.30458 \\ c_5 &= 0.025 \\ c_6 &= -552.62218. \end{aligned} \tag{4.5}$$

Note that this function was a fit to $\ln(s-1)$ rather than $\ln s$. The coefficients published in [23] had fewer significant figures. There are some delicate cancellations between the terms of the old function which require the greater numerical precision. This function is plotted in Figure 4.7 together with the data used in the current fit. While at high energies the fit is not too bad, at 2 A GeV and below the fit becomes steadily worse. This function was the result of a fit to a different data set, but the fit is as bad there. This was the result of the assumption that the response as a function of charge could be fitted independently of energy and *vice versa*. Thus the portion of (4.5) which depends only on

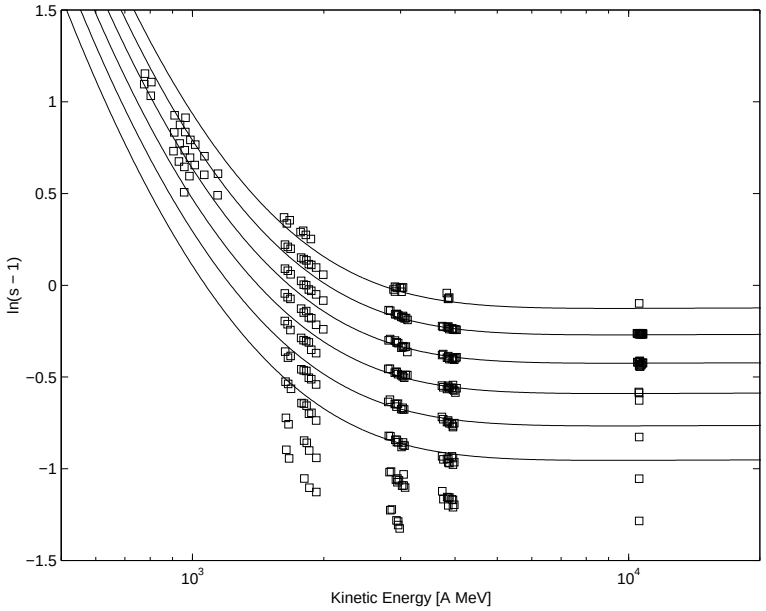

Figure 4.7: Detector response in terms of $\ln(s-1)$ plotted versus kinetic energy. Lines indicate the old fitted response function for Hg, Au, Pt, Ir, Os, and Re.

charge was fitted to only one energy (the 10.8 A GeV beam), while the portion which depends on β was fitted only to one charge (Au).

4.3 Relativistic Rise

In previous analyses of cosmic-ray data, we have assumed that the response function is flat at kinetic energies greater than about 10 A GeV. More precisely, we have, in the past, performed fits to signal data using only functions of velocity, $\beta = v/c$, which necessarily approach a value which depends only on charge at high energies. However, it is a well known fact that the rate of energy loss $\mathrm{d}E/\mathrm{d}x$ due to ionization of the medium traversed by a relativistic nucleus exhibits a relativistic rise ($\mathrm{d}E/\mathrm{d}x \sim \ln\gamma$, when the density effect is included) above a few A GeV, though this is ultimately limited by finite nuclear size effects.

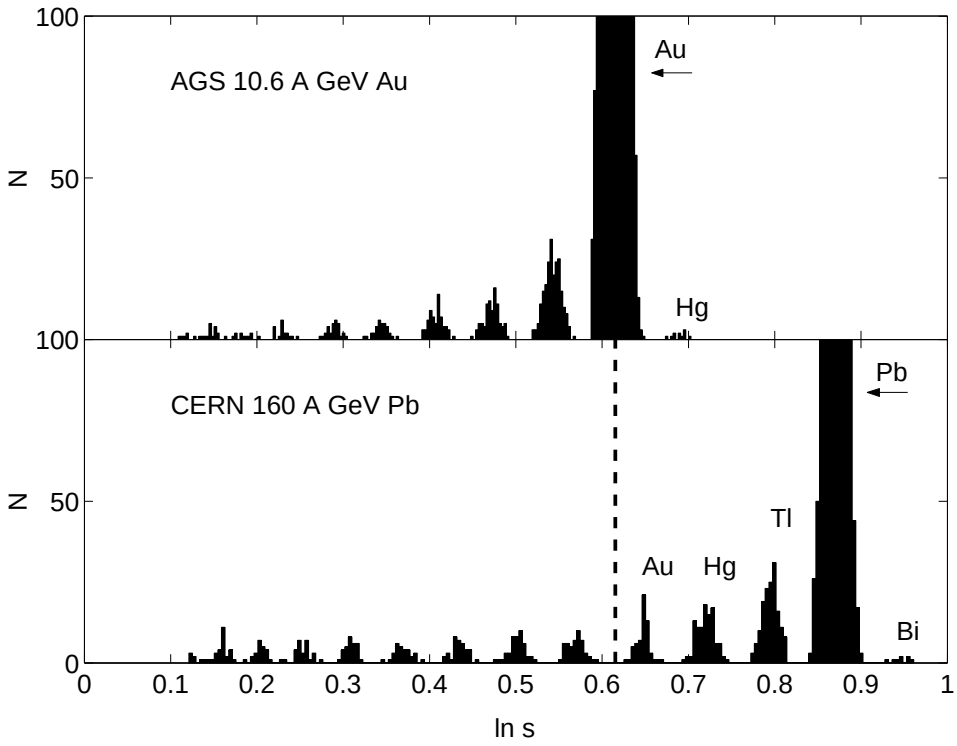

Figure 4.8: Comparison of track-etch signal (ln$s$) for 10.8 A GeV Au and 160 A GeV Pb in the same detector. The large peaks in both histograms are the main beam in each case. A small but significant number of charge pickup events (labelled "Hg" and "Bi" in the top and bottom histograms, respectively) can clearly be seen. Further discussion is in the main text.

A relativistic rise in track-etch signal could, in principle, allow a highly relativistic nucleus with a small charge to masquerade as a more highly charged nucleus at somewhat lower energy. While the fraction of events in our GCR sample with energies in excess of 10 A GeV is small ($< 5\%$), a significant relativistic rise could produce a tail in the point-spread functions used to reconstruct source abundances. To investigate the size of this effect, we etched BP-1 glass which had been exposed to two beams: first, a 10.8 A GeV Au beam at the AGS, and second, a 160 A GeV Pb beam at CERN. We were thus able to compare the track-etch signals of the two beams *in the same detector*.

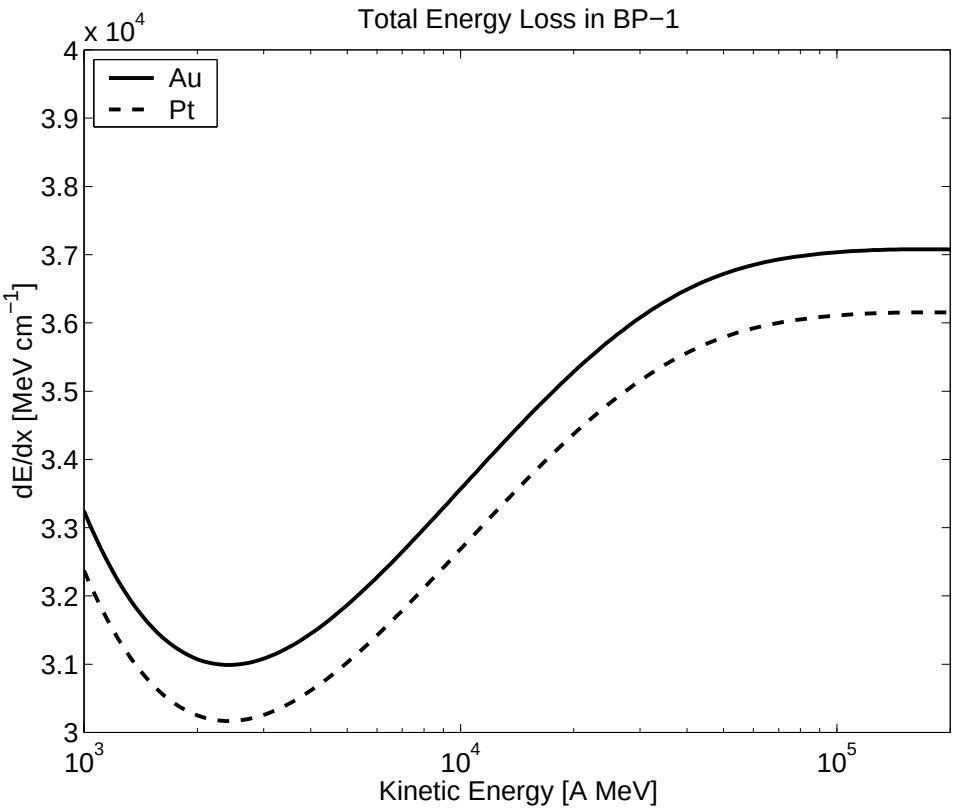

Figure 4.9: Stopping power of Au and Pt are plotted versus kinetic energy. The rise between 3 and 30 A GeV includes the density effect. At the highest energies, the rise is limited by finite nuclear size effects.

The results of this investigation are shown in Figure 4.8. The dashed line in the figure shows the expected signal of Au at 160 A GeV if there is no relativistic rise at all. Comparing the main Au peak at 10.8 A GeV to the Au fragments of Pb shows a very slight rise in signal, approximately 0.3 charge units. Figure 4.9 shows the total ionization energy loss of Au and Pt in BP-1. Note that the change in energy loss from 10 A GeV to 100 A GeV is much larger than the change from charge $Z = 78$ to $Z = 79$. Therefore if track-etch response were in some way proportional to or a function of total ionization energy loss, we would expect a relativistic rise in signal of several charge units, an order of magnitude larger than the change in signal we actually observe. Arguably, it is the restricted energy loss (REL) rather than total energy loss which we should consider. REL has been used to predict the response of plastics [88]. However, REL also exhibits a relativistic rise of exactly the same form as total energy loss. We have also found that the hypothesis $\ln s = f(Z,\beta) + a\ln(\ln\gamma)$, where a is an empirically determined constant, and $f(Z,\beta)$ is determined from the low-energy data, also predicts a relativistic rise larger than what is observed. Thus, while the very small relativistic rise we observe is a fascinating clue to nuclear track formation in glass, it is unlikely to impair the performance of Trek and ECCO.

Since these exposures were performed at different times, with the Au exposure taking place more than a year before the Pb exposure, I investigated the possibility that the apparent shift in response could be caused by differential thermal fading. I used the model of [23] in which the shift in response is given by

$$\Delta(\ln[s-1]) = At^{1-n}\exp\left(-\frac{E}{k_{\mathrm{B}}T}\right), \tag{4.6}$$

with $\ln A = 5.88$, $n = 0.837$, $E = 0.209$ eV, t is the time in hours since exposure, T is the absolute temperature, and k_{B} is Boltzmann's constant.

Event	Date
10.8 A GeV Au exposure	8 September 1993
160 A GeV Pb exposure	1 December 1994
Corrective anneal start	2 June 2000
Corrective anneal end	7 June 2000
Etch start	13 June 2000

Table 4.1: Dates relevant to the thermal history of the glass used in the relativistic rise analysis.

Table 4.1 summarizes the history of the glass used in this analysis. Since we do not know the detailed thermal history of the glass, especially between the two accelerator exposures, we consider a simple model in which the glass was held at a constant temperature T_1 between the two exposures. It was then placed in long-term storage at another temperature T_2 and held at that temperature until the corrective anneal. During the anneal period, the temperature was actually measured to be $T_3 = 51.1^\circ$ C.

The measured value of the shift in $\ln(s-1)$ for the Au peaks was 0.0756 ± 0.0022. This value is indicated by the solid horizontal line in Figure 4.10. For comparison, a shift of $\Delta\ln(s-1) = 0.15$ is equivalent to one charge unit at these energies. In this model, the observed shift is consistent with a storage between exposures at $T_1 = 25.1 \pm 0.3^\circ$ C for $T_2 = -20^\circ$ C, or $T_1 = 25.4 \pm 0.3^\circ$ C for $T_2 = 0^\circ$ C. For $T_2 > 10^\circ$ C, the storage temperature between exposures starts to become unrealistically high to explain the observed shift. Of course, this assumes that the glass was not deliberately heated at any time prior to the corrective anneal. If in fact $T_1 \approx 20^\circ$ C or less, as is almost certainly the case, since the glass was held in cold storage, then thermal fading cannot explain the observed shift.

With some confidence, then, we can say that the relativistic rise in BP-1 is *at most* $\sim 0.5e$ over the energy range 10 to 100 A GeV, since thermal effects would only tend to decrease the observed shift in this sample (unless the sample were stored at unrealistically high temperatures).

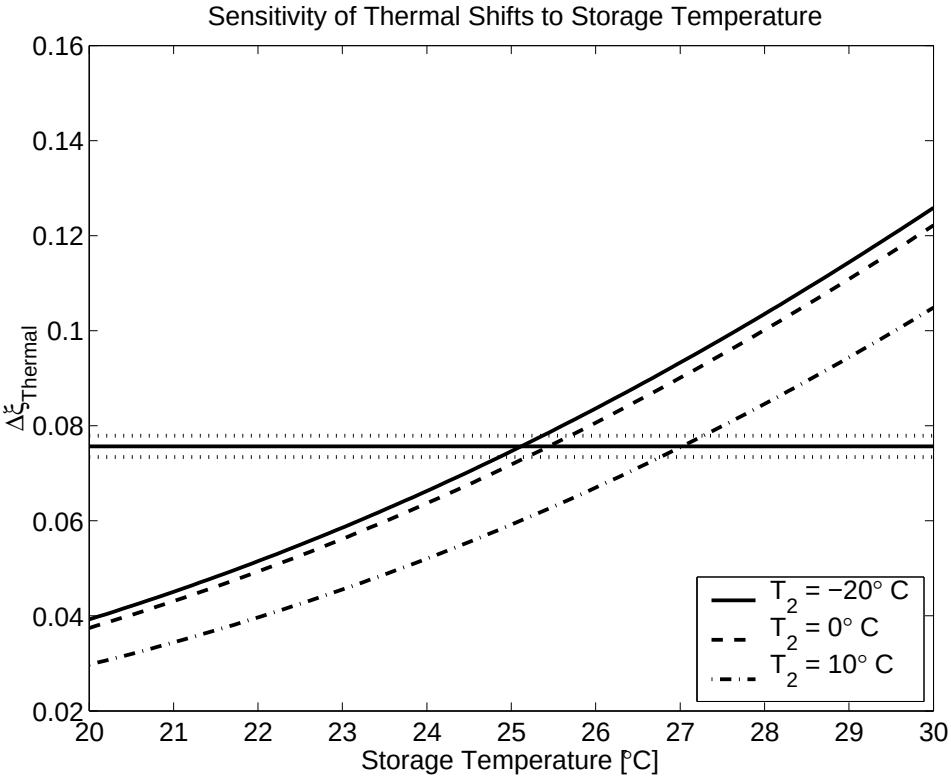

Figure 4.10: Shift in response in terms of $\ln(s-1)$ as a function of storage temperature between accelerator exposures for three different models of the long-term storage temperature. The measured value for Au is indicated by the horizontal line. The horizonal dotted lines indicate the 1σ statistical error bars on the measured value.

Obviously, if a shift of the same magnitude and direction were observed in a sample which was exposed to 10 A GeV Au *after* being exposed to 160 A GeV Pb, this would confirm the observation of relativistic rise in BP-1.

4.4 Conclusion

This study has shown the absolute necessity of considering charge and energy together in a single dataset when fitting an empirical response function. It is also clear that the energies of nuclear fragments are not the same as those of the parent beam. This effect is increasingly important at low energies. Furthermore, the relativistic rise of BP-1 is negligible for all practical purposes, so we do not have to be concerned about a 100 A EeV Pb nucleus masquerading as an actinide (to use a somewhat fanciful example). The extremely simple form of the low-energy response function and the lack of significant relativistic rise are important clues to the track-formation mechanism in BP-1.

At present it is not possible to determine the response of BP-1 to highly relativitic actinide nuclei ($\sim$ 10 A GeV) in a systematic way. However, beams of U at this scale will probably be available in the near future at RHIC. At that point it will be possible to make an empirical determination of the response function of BP-1 to actinides when etched in NaOH. We already have evidence based on the high-energy Trek actinide candidates and BP-1 exposed to low-energy U at GSI that the response of BP-1 etched in NaOH will be the same as the response in HF, but offset by an overall constant. The techniques established in this study will be of great practical use in the determination of this response function.

Chapter 5

Bound-State Beta-Decay

Istanbul was Constantinople
Now it's Istanbul, not Constantinople
Been a long time gone, Constantinople
Now it's Turkish delight on a moonlit night
— "Istanbul (Not Constantinople)," *Flood* (1990)

5.1 Introduction

Bound-state beta decay (hereinafter β_b decay) is an uncommon beta decay mode in which the electron is emitted into a bound atomic state rather than into the continuum. Because of the exclusion principle, the final atomic state must be initially empty, so isotopes which can only decay by β_b decay are stable as neutral atoms. However, when completely ionized as in the Galactic cosmic rays, these isotopes can decay. The isotope ^{193}Ir has been predicted to undergo β_b decay. ^{193}Ir is the most abundant isotope of iridium in the solar system. The results from the Trek detector suggest a depletion of iridium in the Galactic cosmic rays. Such a signal would be consistent with the β_b decay of this isotope. This would be only the third example of β_b decay ever observed and

the first observation in a natural system.

The possibility that ionized atoms could undergo β_b decay has been known for over fifty years [89, 90]. However, fully stripped nuclei which can be stored for a sufficiently long period to measure half-lives are available in the laboratory only at dedicated heavy-ion storage rings, such as the one at GSI. This type of beta decay has been observed for the first time only recently in ^{163}Dy [91] and ^{187}Re [92]. A naturally-occurring sample of fully ionized nuclei is the Galactic cosmic rays (GCRs). We expect the effects of β_b decay to be apparent in observations of elemental abundances in the GCRs.

Perhaps the most fascinating aspect of β_b decay is that it forces a reconsideration of nuclear stability. That is, "stable" atoms can become unstable to β_b decay when fully ionized (the rate of β_b decay declines steeply once the atomic K and L shells are filled). For purposes of discussion, we define a β_b-*isotope* as an isotope which is stable, or very nearly so, as a neutral atom, but which decays by β_b decay when fully ionized. Altogether there are four such isotopes in nature: ^{163}Dy, ^{187}Re, ^{193}Ir, and ^{205}Tl. We have included ^{187}Re as a β_b-isotope because of its extremely long continuum beta decay half-life (45.3 Gyr [93]). In general, a fully stripped nucleus is energetically favored to undergo β_b decay to the K shell when

$$Q_{\beta_b} = M_p - M_d - B_p + B_d - K_d > 0, \tag{5.1}$$

where M_p and M_d denote the masses (in appropriate energy units) of the *neutral* parent and daughter atoms, B_p and B_d denote the total electronic binding energies of the neutral atoms, and K_d is the K-shell binding energy of the hydrogen-like daughter ion. All binding energies are assumed to be negative in this definition.

Ratio	solar	Measured at Detector
Os	0.252 ± 0.019	$0.279^{+0.031}_{-0.033}(\text{stat.})^{+0.011}_{-0.011}(\text{syst.})$
^{191}Ir	0.092 ± 0.013	
^{193}Ir	0.155 ± 0.013	
Ir	0.247 ± 0.018	$0.190^{+0.036}_{-0.031}(\text{stat.})^{+0.007}_{-0.011}(\text{syst.})$
Pt	0.500 ± 0.043	$0.438^{+0.028}_{-0.041}(\text{stat.})^{+0.032}_{-0.032}(\text{syst.})$

Table 5.1: Solar system abundance ratios compared with abundance ratios observed in the Extended-Trek analysis. All ratios are (species/Pt-group).

5.2 Extended-Trek Measurement

The Trek detector, described in Chapter 2, was designed to measure the abundances of platinum-group elements, lead, and actinides in the GCRs. Though originally designed to answer questions about the source of GCRs, the range of elements analyzed encompasses three β_b-isotopes: ^{187}Re, ^{193}Ir, and ^{205}Tl. The natural abundances of ^{187}Re and ^{205}Tl are extremely low, so we would not expect any cosmic-ray experiment to say anything definite about these isotopes. However, Ir, at least in the solar system, is as abundant as its neighbor, Os, and ^{193}Ir is the most abundant of the two stable isotopes of Ir. Evidence for β_b decay of this isotope in the GCRs would constitute the first observation of β_b decay in a natural setting.

The predicted β_b half-life of ^{193}Ir is 140 yr [94], while the lifetime of nuclei in the GCRs is of order 10 Myr [95]. While this long half-life may put detection beyond the reach of laboratory storage rings, we expect ^{193}Ir to be effectively absent from the GCRs. In addition, the β_b daughter nucleus is ^{193}Pt, which is unstable to electron capture as a neutral atom, but which is stable in the GCRs.

The GCR abundances of the platinum-group elements measured by Extended-Trek are summarized in Table 5.1. We compare the observed GCR abundances to the solar abundances of Anders and Grevesse [96]. We have defined the "Pt-group" to include the total elemental abundance of atomic numbers $75 \leq Z \leq 79$. The Extended-Trek observed abundances are corrected for detector acceptance, but not for propagation through the interstellar medium. Iridium does appear depleted relative to solar values, but the statistics do not make this claim a particularly strong one.

5.3 Source Abundances

In this region of interest, nuclei are formed by the s-process or the r-process. The s-process refers to the *slow* capture of neutrons onto seed nuclei with enough time on average for ordinary continuum beta decay to take place between neutron captures. This process is thought to occur in asymptotic giant branch (AGB) stars. In contrast, the r-process involves the *rapid* capture of neutrons onto seed nuclei. This probably takes place in supernovae. Extremely neutron-rich nuclei are formed until it becomes energetically unfavorable for the nucleus to absorb another neutron (this is the so-called "neutron drip line"). Neutron magic numbers—such as the $N = 126$ magic number—constitute bottlenecks in the r-process, *i.e.*, nuclei build up at $N = 126$. A peak in abundances is formed after these nuclei beta decay back to the line of stability. The platinum-group nuclei are synthesized principally by the r-process and are the result of the $N = 126$ bottleneck. Only a very small fraction of platinum-group nuclei are synthesized by the s-process.

It is important to consider the source abundances for the GCRs. Our calculations show that the most favored models for the source of GCRs are, first, a fresh (young) source of pure r-process material [4], and, second, a source consisting of Galactic material (similar to solar material

but with additional material from more recent episodes of nucleosynthesis) with preferential acceleration by volatility [16, 17]. We have considered a number of nucleosynthetic models [4, 72, 97] for the s-process. We obtained r-process abundances by subtracting the s-process from solar abundances. All three sources agree on the abundances of Pt-group elements, with the exception of some uncertainty in the s-process abundance of Ir. However, because the ratio r/s for Pt-group elements is at least a factor of ten, uncertainty in the s-process abundance of Ir does not significantly alter the overall abundance of Ir. Furthermore, the Trek detector has strongly ruled out a GCR source dominated by s-process abundances. We also considered local Galactic abundances, which could, in principle, differ from solar values of abundances. We considered the nucleosynthetic and Galactic chemical evolution model of Thielemann, Metzinger, and Klapdor [98], but found that contemporary Galactic abundances of Pt-group elements do not differ significantly from solar values. Within the uncertainties, the abundances of Os and Ir are equal in every case. Finally, the atomic properties of the platinum group, including volatility, are all very nearly the same, so preferential acceleration by volatility would not lead to observed abundances significantly different from solar values. Thus, there is no reason to expect a depletion of Ir relative to Os in any cosmic-ray source/propagation model unless ^{193}Ir experiences β_b decay.

5.4 Conclusion

Once again the versatility of BP-1 as a detector has been demonstrated. The depletion of Ir in the cosmic rays appears to be only consistent with β_b decay of ^{193}Ir, a process which has not, to date, been detected in the laboratory. Trek was certainly not designed to detect β_b decay. Indeed, the importance of this process was not recognized by the Trek collaborators until after the detector

had been returned to Earth. That we have been able to, in some sense, beat the accelerator without even planning to, bodes well for the kinds of bonus science planned and unplanned for the ECCO detector.

Chapter 6

Conclusion

> Where was I? I forgot
> The point that I was making
> I said if I was smart that I would
> Save up for a piece of string
> And a rock to wind the string around.
> — "We Want a Rock," *Flood* (1990)

The future of track-etch detectors is quite secure. No other detector can be scaled to the sizes needed to meaningfully search for rare cosmic rays such as actinides or more exotic particles. The challenges of scaling up from Trek to ECCO are many, but as we have seen, many of those challenges have already been met and solved. The flexibility of track-etch detectors is so great that new experimental goals can be chosen even after the detector exposure is over. With Extended-Trek, we have experimentally demonstrated improvements in charge resolution and conducted a search for the effects of bound-state beta decay long after the actual Trek mission was complete. Unlike fleeting electronic pulses, nuclear tracks are *permanent* and will last as long as the detector is undamaged and stored at low temperature.

As promised, I would like to distill the lessons learned in this study into a series of recommendations for ECCO and other future track-etch detector missions:

- **Etching has its surprises.** The sudden appearance of frosting was both a shock and, admittedly, a temporary setback. There are really two lessons here: first, one cannot assume that the materials used to fabricate etch frames and etch tanks will behave in the same way as materials used in the past; second, it is important to keep everything which goes into an etch tank, including the tank itself, free of contaminants, especially organic materials. Fortunately, it will be relatively easy to satisfy both requirements, in the first case with preliminary test etching, and in the second, everyday organic solvents, such as ethanol and hexane appear to be sufficient to remove organic contaminants even from heavily handled glass. For resurfaced wafers I specifically recommend, in this order, a wash in hexane to remove wax or other adhesives used in the polishing process, a wash in ethanol to remove remaining residues, a wash in ordinary soap and water, and a final rinse in distilled water.

- **Intrinsic dispersion.** It now seems likely that the intrinsic dispersion in response of a track-etch detector is not independent of response, at least for large values of response. Further experiments to determine the extent of this effect should be possible with glass already in storage. It should prove possible to improve the charge resolution of lower-energy cosmic rays ($E < 1000$ A MeV) if the response and dispersion are better understood.

- **Automation is important.** Perhaps the most daunting aspect of scaling up from Trek to ECCO is not the size of the detector, but rather the sheer number of wafers to be analyzed, estimated to be in the range of 10,000 to 100,000, depending on the number of sub-actinide cosmic rays analyzed. Automation at every stage of the analysis will be necessary. As we

have seen, it will be possible to set up a final data analysis pipeline which requires minimal human intervention.

- **Wafers are great.** Glass wafers are amazingly easy to handle at all stages of the analysis. The uniform shape and size lends itself readily to automation at every stage of the analysis, from grinding and polishing all the way to final calibration scanning. Cosmic-ray etch-pits are always easy to find, since they are essentially always in the center of the wafer. Wafers dramatically reduce the costs associated with etchant, especially when one realizes that etchants cost as much, if not more, to dispose of as to purchase fresh. A 9 cm square sheet of glass is guaranteed to break if dropped on a hard floor, but experience seems to suggest that a wafer dropped on the same floor will break less than one-third of the time. It is not unreasonable to assert that the use of wafers reduced the time to complete the Extended-Trek analysis by more than a year.

- **Resurfacing is harmless.** The dicing and polishing of wafers after exposure is at the heart of the monolithic block technique. Resurfacing does not affect charge measurement or resolution both with calibration beams and with *actual cosmic-ray tracks*. Moreover, these results can be achieved with simple-to-operate equipment which anyone can learn to use in a relatively short time. While the sheer number of wafers expected from ECCO will probably require the services of a dedicated technician, we can be confident that anyone assigned this task will produce satisfactory results.

Bibliography

[1] P. Freier *et al.*, Phys. Rev. **79**, 213 (1948).

[2] P. Freier, E. J. Lofgren, and F. Oppenheimer, Phys. Rev. **79**, 1818 (1948).

[3] H. L. Bradt and B. Peters, Phys. Rev. **74**, 1828 (1948).

[4] W. R. Binns *et al.*, in *Cosmic Abundances of Matter*, edited by C. J. Waddington (AIP, New York, 1989), p. 147.

[5] J.-P. Meyer, Astrophys. J. Supp. **57**, 173 (1985).

[6] W. R. Webber, Space Sci. Rev. **81**, 107 (1997).

[7] D. V. Reames, Adv. Space Res. **15**, 41 (1995).

[8] T. K. Gaisser, *Cosmic Rays and Particle Physics* (Cambridge University Press, Cambridge, 1990).

[9] W. R. Binns *et al.*, Astrophys. J. **346**, 997 (1989).

[10] P. H. Fowler *et al.*, Astrophys. J. **314**, 739 (1987).

[11] B. S. Meyer, Ann. Rev. Astron. Astrophys. **32**, 153 (1994).

[12] R. Ramaty, B. Kozlovsky, and R. Lingenfelter, Phys. Today **51**, 30 (1998).

[13] N. Grevesse and J.-P. Meyer, in *Proceedings of the 19th International Cosmic Ray Conference* (NASA, La Jolla, 1985), Vol. 3, p. 5.

[14] R. I. Epstein, Mon. Not. R. Ast. Soc. **193**, 723 (1980).

[15] C. J. Cesarsky and J. P. Bibring, in *IAU Symposium 94, Origin of Cosmic Rays*, edited by G. Setti, G. Spada, and A. W. Wolfendale (Reidel, Dordrecht, 1980), p. 361.

[16] J.-P. Meyer, L. O. Drury, and D. C. Ellison, Astrophys. J. **487**, 182 (1997).

[17] D. C. Ellison, L. O. Drury, and J.-P. Meyer, Astrophys. J. **487**, 197 (1997).

[18] A. J. Westphal, P. B. Price, B. A. Weaver, and V. G. Afanasyev, Nature **396**, 50 (1998).

[19] J. Madsen, in *Hadrons in Dense Matter and Hadrosynthesis*, edited by J. Cleymans, H. B. Geyer, and F. G. Scholtz (Springer-Verlag, Berlin, 1999), p. 162.

[20] B. Pfeiffer, private communication, 1998.

[21] S. C. Wang *et al.*, Nucl. Inst. Meth. B **35**, 43 (1988).

[22] G. J. Agin, *Fitting Ellipses and General Second-Order Curves* (Carnegie-Mellon University, The Robotics Institute, Pittsburgh, 1981).

[23] B. A. Weaver *et al.*, Nucl. Inst. Meth. B **145**, 409 (1998).

[24] E. V. Benton and R. P. Henke, Nucl. Inst. Meth. **67**, 87 (1969).

[25] A. J. Westphal, Y. D. He, and P. S. Wojdowski, Nucl. Inst. Meth. B **86**, 317 (1994).

[26] K. Hikasa *et al.*, Phys. Rev. D **45**, 1 (1992).

[27] W. H. Barkas and M. J. Berger, in *Studies in Penetration of Charged Particles in Matter*, No. 39 in *Nuclear Science Series*, edited by U. Fano (National Academy of Sciences—National Research Council, Washington, D.C., 1964), Chap. 7, p. 103, publication 1133.

[28] S. P. Ahlen, Rev. Mod. Phys. **52**, 121 (1980).

[29] S. P. Ahlen and G. Tarlé, Phys. Rev. Lett. **50**, 1110 (1983).

[30] J. D. Jackson, *Classical Electrodynamics*, 2nd ed. (John Wiley & Sons, New York, 1975).

[31] J. Lindhard and A. H. Sørensen, Phys. Rev. A **53**, 2443 (1996).

[32] W. H. Bragg and R. Kleeman, Philos. Mag. **10**, 318 (1905).

[33] M. J. Berger *et al.*, *Stopping Powers for Electrons and Positrons*, No. 37 in *ICRU Reports* (International Commission on Radiation Units and Measurements, Bethesda, Maryland, 1984).

[34] E. Fermi, Phys. Rev. **57**, 485 (1940).

[35] R. M. Sternheimer and R. F. Peierls, Phys. Rev. B **3**, 3681 (1971).

[36] R. M. Sternheimer, M. J. Berger, and S. M. Seltzer, Atom. Dat. Nucl. Dat. Tab. **30**, 261 (1984).

[37] S. M. Seltzer, private communication, 2000.

[38] F. Bloch, Ann. Phys. (Leipzig) **16**, 285 (1933).

[39] G. Tarlé and M. Solarz, Phys. Rev. Lett. **41**, 483 (1978).

[40] M. H. Salamon, S. P. Ahlen, G. Tarlé, and K. C. Crebbin, Phys. Rev. A **23**, 73 (1981).

[41] S. P. Ahlen, Phys. Rev. A **17**, 1236 (1978).

[42] J. A. Doggett and L. V. Spencer, Phys. Rev. **103**, 1597 (1956).

[43] R. M. Curr, Proc. Phys. Soc. (London) **68**, 156 (1955).

[44] S. P. Ahlen, Phys. Rev. A **25**, 1856 (1982).

[45] C. J. Waddington, P. S. Freier, and D. J. Fixsen, Phys. Rev. A **28**, 464 (1983).

[46] P. Sigmund, Nucl. Inst. Meth. B **135**, 1 (1998).

[47] M. E. Rose, *Relativistic Electron Theory* (Wiley, New York, 1961).

[48] C. P. Bhalla and M. E. Rose, Phys. Rev. **128**, 774 (1962).

[49] A. H. Sørensen, private communication, 1999.

[50] A. H. Sørensen, in *Photonic, Electronic and Atomic Collisions; Twentieth International Conference on the Physics of Electronic and Atomic Collisions*, edited by F. Aumayr and H. Winter (World Scientific, Singapore, 1998), p. 475.

[51] C. Scheidenberger, Ph.D. thesis, Universität Gießen, 1994.

[52] S. Datz *et al.*, Phys. Rev. Lett. **77**, 2925 (1996).

[53] V. Z. Jankus, Phys. Rev. **90**, 4 (1953).

[54] W. Heitler, *The Quantum Theory of Radiation*, 3rd ed. (Oxford University Press, London, 1954).

[55] T. E. Pierce and M. Blann, Phys. Rev. **173**, 390 (1968).

[56] N. Bohr, Kgl. Danske Videnskab. Selskab., Mat.-Fys. Medd. **18**, 1 (1948).

[57] N. Bohr and J. Lindhard, Kgl. Danske Videnskab. Selskab., Mat.-Fys. Medd. **28**, 1 (1954).

[58] J. M. Anthony and W. A. Landford, Phys. Rev. A **25**, 1868 (1982).

[59] F. Hubert, R. Bimbot, and H. Gauvin, Nucl. Inst. Meth. B **36**, 357 (1989).

[60] F. Hubert, R. Bimbot, and H. Gauvin, Atom. Dat. Nucl. Dat. Tab. **46**, 1 (1990).

[61] W. H. Barkas, N. J. Dyer, and H. H. Heckmann, Phys. Rev. Lett. **11**, 26 (1963).

[62] H. H. Heckman and P. J. Lindstrom, Phys. Rev. Lett. **22**, 871 (1969).

[63] J. C. Ashley, R. H. Ritchie, and W. Brandt, Phys. Rev. B **5**, 2393 (1972).

[64] J. C. Ashley, R. H. Ritchie, and W. Brandt, Phys. Rev. A **8**, 2402 (1973).

[65] J. C. Ashley, R. H. Ritchie, and W. Brandt, Phys. Rev. A **10**, 737 (1974).

[66] J. D. Jackson and R. L. McCarthy, Phys. Rev. B **6**, 4131 (1972).

[67] J. Lindhard, Nucl. Inst. Meth. **132**, 1 (1976).

[68] S. H. Morgan, Jr. and C. C. Sung, Phys. Rev. A **20**, 818 (1979).

[69] C. J. Waddington *et al.*, Phys. Rev. A **34**, 3700 (1986).

[70] U. Fano, Ann. Rev. Nucl. Sci. **13**, 1 (1963).

[71] H. Bichsel, in *A.I.P. Handbook*, 3rd ed., edited by D. E. Gray (McGraw-Hill, New York, 1972), Chap. 8, p. 142.

[72] H. Bichsel, Phys. Rev. A **46**, 5761 (1992).

[73] H. H. Andersen, J. F. Bak, H. Knudsen, and B. R. Nielsen, Phys. Rev. A **16**, 1929 (1977).

[74] P. T. Leung, Phys. Rev. A **40**, 5417 (1989).

[75] P. T. Leung, Phys. Rev. A **60**, 2562 (1999).

[76] S. P. Ahlen, G. Tarlé, and P. B. Price, Science **217**, 1139 (1982).

[77] G. Tarlé, private communication, 1999.

[78] M. H. Salamon, Ph.D. thesis, University of California, Berkeley, 1981.

[79] D. Schardt, private communication, 1999.

[80] P. H. Pile, private communication, 2000.

[81] R. Silberberg and C. H. Tsao, Astrophys. J. Supp. **25**, 315 (1973).

[82] R. Silberberg and C. H. Tsao, Astrophys. J. Supp. **25**, 335 (1973).

[83] J. R. Letaw, R. Silberberg, and C. H. Tsao, Astrophys. J. Supp. **56**, 396 (1984).

[84] R. Silberberg, C. H. Tsao, and J. R. Letaw, Astrophys. J. Supp. **58**, 873 (1985).

[85] R. Silberberg and C. H. Tsao, Phys. Rep. **191**, 351 (1990).

[86] C. H. Tsao *et al.*, Phys. Rev. C **47**, 1257 (1993).

[87] R. Silberberg, C. H. Tsao, and A. F. Barghouty, Astrophys. J. **501**, 911 (1998).

[88] E. V. Benton and W. D. Nix, Nucl. Inst. Meth. **67**, 343 (1969).

[89] R. Daudel *et al.*, C. R. Acad. Sci. (Paris) **224**, 1427 (1947).

[90] R. Daudel, M. Jean, and M. J. Lecoin, Phys. Radium **8**, 238 (1947).

[91] M. Jung *et al.*, Phys. Rev. Lett. **69**, 2164 (1992).

[92] F. Bosch *et al.*, Phys. Rev. Lett. **77**, 5190 (1996).

[93] J.-M. Luck and C. J. Allègre, Nature **302**, 130 (1983).

[94] K. Takahashi, R. N. Boyd, G. J. Mathews, and K. Yokoi, Phys. Rev. C **36**, 1552 (1987).

[95] A. Lukasiak, P. Ferrando, F. B. McDonald, and W. R. Webber, Astrophys. J. **423**, 426 (1994).

[96] E. Anders and N. Grevesse, Geochim. Cosmochim. Acta **53**, 197 (1989).

[97] F. Käppeler, H. Beer, and K. Wisshak, Rep. Prog. Phys. **52**, 945 (1989).

[98] F.-K. Thielemann, J. Metzinger, and H. V. Klapdor, Z. Phys. A **309**, 301 (1983).

[99] W. H. Press, S. A. Teukolsky, W. T. Vetterling, and B. P. Flannery, *Numerical Recipes in C*, 2nd ed. (Cambridge University Press, Cambridge, 1992).

[100] R. L. Fleischer, P. B. Price, and R. M. Walker, *Nuclear Tracks in Solids* (University of California Press, Berkeley, 1975).

Appendix A

Definitions

A.1 $Q(\chi^2|\nu)$

Throughout this work, the function $Q(\chi^2|\nu)$ will be interpreted as the probability that the value of χ^2 obtained by maximum likelihood methods should exceed a particular value of χ^2 by chance for ν degrees of freedom. The definition of $Q(\chi^2|\nu)$ is simply

$$Q(\chi^2|\nu) = \int_{\chi^2}^{\infty} F(\chi'^2,\nu)\mathrm{d}\chi'^2, \tag{A.1}$$

where F is the probability distribution of χ^2 for ν degrees of freedom given by

$$F(\chi^2,\nu)\mathrm{d}\chi^2 = \frac{\left(\chi^2\right)^{\nu/2-1}\exp\left(-\chi^2/2\right)}{2^{\nu/2}\Gamma(\nu/2)}\mathrm{d}\chi^2. \tag{A.2}$$

It is possible to show that $Q(\chi^2|\nu) = 1 - P(\nu/2,\chi^2/2)$, where

$$P(a,x) = \frac{1}{\Gamma(a)}\int_0^x \exp(-t)t^{a-1}\mathrm{d}t \tag{A.3}$$

is the incomplete gamma function.

The application of this function is best illustrated by a simple example. Suppose we make some measurements and fit the measurements to a model with adjustable parameters by minimizing χ^2. If the model is correct, and the errors associated with the individual measurements are of the correct magnitude, then we should expect $Q(\chi^2|\nu) \approx 0.5$, indicating that if we made another set of measurements from scratch and again minimized χ^2, about 50% of the time we should find a new χ^2 larger than the original value. It is possible to show by Monte Carlo techniques that if a set of values of χ^2 are drawn from the distribution (A.2), then the distribution of $Q(\chi^2|\nu)$ is *uniform* on the interval $[0,1]$. The distribution remains uniform even if we have several sets of χ^2 drawn from distributions with different degrees of freedom. This gives a mechanism to measure the overall goodness-of-fit for a whole set of measurements, each with different degrees of freedom but fitted to the same overall model (with only the parameters differing).

A.2 Kolmogorov-Smirnov Test

The Kolmogorov-Smirnov (KS) test is a statistical technique to answer the question: Are two distributions different? In contrast to χ^2 fitting, the KS test does not require the data to be binned. Consider a one-dimensional dataset $\{x_k\}$ with the index $k = 1,\ldots,N$ which has been sorted so that $x_1 < x_2, x_2 < x_3, \ldots, x_{N-1} < x_N$. The cumulative distribution of x is denoted $S(x)$ and $S(x_k)$ gives the fraction of data points less than or equal to x_k. In general, $S(x_k) = k/N$, so that $S(x_N) = 1$. In modeling the data we assume that the data comes from an underlying probability distribution function $F(x)$ (*i.e.*, "the model"). The cumulative model probability we denote by $I(x)$ and is given by

$$I(x) = \int_{x_1}^{x} F(x')\mathrm{d}x'. \tag{A.4}$$

If the model is properly normalized then $I(x_1) = 0$ and $I(x_N) = 1$. In general $I(x_k)$ gives the probability of finding $x \leq x_k$.

Now we wish to compare the cumulative distribution of the data to that of the model. We define the KS statistic $D_{\rm KS}$ as

$$D_{\rm KS} = \max |S(x) - I(x)| \tag{A.5}$$

over the full range of x. While there are certainly other ways to compare $S(x)$ and $I(x)$, as it happens the significance level $Q_{\rm KS}$ can be calculated fairly simply. In analogy to $Q(\chi^2|\nu)$ for the χ^2 distribution, $Q_{\rm KS}$ gives the probability that $D_{\rm KS}$ should exceed the observed value by chance even for a correct model. It is given by the formula

$$Q_{\rm KS}(\lambda) = 2\sum_{j=1}^{\infty}(-1)^{j-1}\exp\left(-2j^2\lambda^2\right), \tag{A.6}$$

with λ given by

$$\lambda = D_{\rm KS}\left[\sqrt{N} + 0.12 + 0.11/\sqrt{N}\right]. \tag{A.7}$$

A.3 Gamma Function

The complex Gamma function, both its magnitude and argument, appears frequently in dE/dx calculations. To very high precision the Gamma function is given by [99]

$$\Gamma(z+1) = \left(z+\gamma+\frac{1}{2}\right)^{z+\frac{1}{2}}\exp\left[-\left(z+\gamma+\frac{1}{2}\right)\right]\sqrt{2\pi}\left[c_0 + \sum_{k=1}^{N}\frac{c_k}{z+k} + \varepsilon\right]. \tag{A.8}$$

For special choices of γ, N, and the parameters c_k, the error term $|\varepsilon| < 2\times 10^{-10}$ everywhere in the right complex plane, Re$z > 0$. The special choices are $\gamma = 5$, $N = 6$, and

$$c_0 \quad = \quad 1.000000000190015$$

$$
\begin{aligned}
c_1 &= 76.18009172947146 \\
c_2 &= -86.50532032941677 \\
c_3 &= 24.01409824083091 \\
c_4 &= -1.231739572450155 \\
c_5 &= 0.1208650973866179 \times 10^{-2} \\
c_6 &= -0.5395239384953 \times 10^{-5}.
\end{aligned} \tag{A.9}
$$

With some effort, the real and imaginary parts can be extracted from this formula and from these, the absolute value and the argument. If we let $z = x + \mathrm{i}y$, then we must define two parameters

$$T = -y \sum_{k=1}^{6} \frac{c_k}{(x+k)^2 + y^2}, \tag{A.10}$$

and

$$B = c_0 + \sum_{k=1}^{6} \frac{c_k (x+k)}{(x+k)^2 + y^2}. \tag{A.11}$$

Now we have

$$
\begin{aligned}
\ln|\Gamma(z+1)| &= \frac{1}{2}\left(x+\frac{1}{2}\right)\ln\left[(x+5.5)^2+y^2\right] - y\arctan\frac{y}{x+5.5} \\
&\quad -(x+5.5) + \ln\sqrt{2\pi\,(T^2+B^2)},
\end{aligned} \tag{A.12}
$$

and

$$
\begin{aligned}
\arg\Gamma(z+1) &= \frac{y}{2}\ln\left[(x+5.5)^2+y^2\right] + \left(x+\frac{1}{2}\right)\arctan\frac{y}{x+5.5} \\
&\quad -y + \arctan\frac{T}{B}.
\end{aligned} \tag{A.13}
$$

For operations taking place in the left complex plane $\mathrm{Re}\, z < 0$, it is handy to know the reflection formula

$$\Gamma(1-z)\Gamma(1+z) = \frac{\pi z}{\sin \pi z}. \tag{A.14}$$

The Gamma function has poles at zero and all negative integers, and that behavior is reproduced faithfully in this formula.

A.4 Confluent Hypergeometric Function

The confluent hypergeometric function, $M(a,b,z)$ [alternatively ${}_1F_1(a,b;z)$] appears in the finite nuclear size correction to the Lindhard-Sørensen correction. The simplest representation is

$$M(a,b,z) = 1 + \frac{\Gamma(b)}{\Gamma(a)} \sum_{n=1}^{\infty} \frac{\Gamma(a+n)}{\Gamma(b+n)} \frac{z^n}{n!}, \tag{A.15}$$

with a,b,z being complex numbers. The implementation of this formula would seem to require an excessive number of calls to the Gamma function, but we recognize here the so-called Pochhammer Symbol

$$\begin{aligned} \frac{\Gamma(z+n)}{\Gamma(z)} &= z(z+1)(z+2)\cdots(z+n-1) \\ &\equiv (z)_n, \end{aligned} \tag{A.16}$$

so that (A.15) becomes

$$M(a,b,z) = 1 + \sum_{n=1}^{\infty} \frac{(a)_n}{(b)_n} \frac{z^n}{n!}. \tag{A.17}$$

Each term in the series can be obtained from the previous one by multiplying by $(a+n-1)z/(b+n-1)n$ and thus requires only complex multiplication.

Appendix B

Etch-Pit Geometry

While the response of a track-etch detector is formally defined as the ratio of the track etch rate to the general etch rate,

$$s \equiv \frac{v_T}{v_G}, \tag{B.1}$$

it is extremely difficult to measure either etch rate while etching is underway. Here we discuss the derivation of response from geometric observables measured after the conclusion of an etch. Fleischer, Price, and Walker [100], Chapter 2, is the basis for these formulae, but two of the most important formulae in their discussion of etch-pit geometry are in error.

We begin with the assumption that neither the track etch rate nor the general etch rate vary on length scales comparable to the size of the etch-pit. In this limit the etch-pit can be treated as a perfect cone. From basic considerations of etching in analogy to the formation of supersonic shock-waves or of Cherenkov radiation, it is possible to derive the fundamental relationship between response and geometry:

$$\frac{1}{s} = \sin\alpha, \tag{B.2}$$

where α is the half-opening angle of the cone. We define the zenith angle, θ, as the angle of the track with respect to the normal. We let t be the amount of time the sample is etched, and the amount of material removed from the bulk surface during etching is defined by

$$G = v_G t. \tag{B.3}$$

The etch-pit cone intersects the etched surface in an ellipse. As usual, we take the semi-major and semi-minor axes to be a and b, respectively. These are given in terms of s, G, and θ by

$$a = G\frac{\sqrt{s^2-1}}{s\cos\theta+1}, \tag{B.4}$$

and

$$b = G\sqrt{\frac{s\cos\theta-1}{s\cos\theta+1}}. \tag{B.5}$$

The formula (B.5) is simple to invert to find the most commonly-used formula in determining response:

$$s = \sec\theta\frac{1+(b/G)^2}{1-(b/G)^2}. \tag{B.6}$$

In order for a track to form at all in a flat surface, the component of the track etch rate normal to the surface must be greater than the bulk etch rate; otherwise, the track will be erased faster than it can form. The requirement $v_T\cos\theta > v_G$ gives

$$s\cos\theta > 1, \tag{B.7}$$

as the criterion for visible etch-pit formation. This criterion also defines the angular acceptance of a rectangular detector. The *threshold* for a given etchant is the smallest charge at relativistic energies which produces a detectable etch-pit (at normal incidence). Different etchants have different thresholds. Thus, HBF_4 is said to be more *sensitive* than HF because it has a lower threshold. NaOH is less sensitive than HF.

In the opposite extreme, $s \to \infty$, we can see from (B.6) that b approaches G as its limiting value. Equivalently, $\mathrm{d}b/\mathrm{d}s \to 0$ in the limit of large s. We refer to this phenomenon as *saturation*. It represents the limit to the ellipse method of measuring s, and in practice, values $s > 7$ are very difficult to measure with the ellipse method. There is a trade-off between sensitivity and saturation. A relativistic Au track will have $s \approx 1.8$ when etched in HF, but will be saturated in HBF_4, and will be below threshold in NaOH. As an alternative to the ellipse method, the depth of the cone also can be converted into a value of s. If we let D be the depth of the tip of the cone below the *etched* surface, measured along the normal to the etched surface, then

$$s\cos\theta = \frac{D}{G} + 1. \tag{B.8}$$

Despite the simplicity of this formula, it has been the experience of others in this field that this method is less sensitive in terms of charge resolution. In addition, it does not lend itself to automated scanning techniques. Furthermore, this formula itself has its limits. If the initial thickness of a track-etch detector sheet is T, then the etch cones on the two sides of the sheet will actually meet when $2(D+G) = T$ or

$$s\cos\theta = \frac{T}{2G}. \tag{B.9}$$

Since some techniques for the preliminary identification of tracks rely on the formation of through-holes, (B.9) gives the minimum s which will form a hole for given G and θ.

Given a, b, and G, it is possible to determine θ. First we define

$$s' = \frac{1+(b/G)^2}{1-(b/G)^2}, \tag{B.10}$$

then θ is given by

$$\cos\theta = \frac{s'}{\sqrt{1+(a/G)^2(s'+1)^2}}. \tag{B.11}$$

If *a* and *b* are both known for two populations of calibration events with the same charge and energy but different zenith angles, it is possible to determine *G* and the two zenith angles simultaneously by assuming the responses of the two beams are equal.

Finally, we consider the measurement of zenith angle by projection. On a microscope stage, the coordinates of the center of the etch-pit ellipse are measured on the top surface and on the bottom surface. However, the center of the ellipse does not coincide with the axis of the cone (and thus not with the particle track). The distance from the point of intersection of the axis of the ellipse with the detector surface to the nearest edge of the ellipse, measured along the major axis, is given by

$$X_1 = G\frac{1-\frac{1}{s\cos\theta}}{\cos(\theta+\alpha)}. \tag{B.12}$$

Since X_1 depends on θ it must be applied iteratively if it is to be used to measure θ. If *G* is also unknown, it is still possible to iteratively determine *G* and θ simultaneously, provided at least *b* is known for two calibration populations.

Appendix C

Fragment Masses From Cross-Sections

The calculation of the abundances of fragments of Au and other ions in BP-1 glass is complicated by two factors: the detector is made entirely of elements heavier than hydrogen and the detector is a compound, not a single element. Fortunately there are easy ways to deal with both problems. First, semi-empirical calculations of the fragmentation cross-sections for a species going to a lighter species on an arbitrary target nucleus are now available. Second, for compounds we can easily implement the equivalent of Bragg's rule for stopping powers.

Let f_k be the fraction by number of element k in a sample. Then the effective cross-section for the fragmentation of ion i into (lighter) ion j is simply

$$\sigma_{ij} = \sum_k f_k \sigma_{ij}(Z_k, A_k). \tag{C.1}$$

We define J_i to be the abundance of species i. The normalization is arbitrary, but it is convenient to set $\sum J_i = 1$. The change in J_j is

$$\mathrm{d}J_j = n\mathrm{d}x \left[\sum_{i>j} \sigma_{ij} J_i - J_j \sum_{k<j} \sigma_{jk} \right], \tag{C.2}$$

where the labels on the sum signs are taken to mean "all species i heavier than j" and "all species k lighter than j" respectively. The second term is simply the definition of the total fragmentation cross-section for species j, σ_j. Now if we maintain the convention that species i is heavier than species j, we are free to define $\sigma_{ji} = 0$ and $\sigma_{jj} = -\sigma_j$. Thus we are left with

$$dJ_j = n dx \sum_k \sigma_{kj} J_k, \tag{C.3}$$

with the index k now running over all species in consideration. Obviously this is a matrix equation and $J_j(x)$ can be solved with routine matrix methods.

We now consider the average mass of a group of fragments with the same charge. Species j has charge Z_j and mass A_j. The total fraction of fragments with charge Z present is then

$$f_Z = \sum_{Z_j=Z} J_j. \tag{C.4}$$

The average is

$$\langle A \rangle_Z = \frac{1}{f_Z} \sum_{Z_j=Z} A_j J_j. \tag{C.5}$$

In the space ship,
The silver space ship,
The lion waves good-bye
— “The Guitar,” *Apollo 18* (1992)